©Copyright 2019
Shi Jin

Fission Dynamics in a Microscopic Theory

Shi Jin

A dissertation
submitted in partial fulfillment of the
requirements for the degree of

Doctor of Philosophy

University of Washington

2019

Reading Committee:

Aurel Bulgac, Chair

Sanjay Reddy

Alejandro Garcia

Program Authorized to Offer Degree:
Physics

University of Washington

Abstract

Fission Dynamics in a Microscopic Theory

Shi Jin

Chair of the Supervisory Committee:
Professor Aurel Bulgac
Department of Physics

This thesis is concerned with the application of the time-dependent density functional theory (TDDFT) to investigate the fission dynamics of atomic nuclei, which is still one of the most complicated problems in nuclear physics and a full microscopic interpretation is still missing. The establishment of the time-dependent superfluid local density approximation (TDSLDA) and the increasing power of computing resources have made the three-dimensional symmetry unrestricted simulations of fission dynamics possible in recent years. In this work, a qualitative new nuclear energy density functional (NEDF) is developed, which contains only seven uncorrelated fitting parameters, and yields excellent performance in describing various nuclear properties, e.g. nuclear mass, charge radii, neutron separation energy, shell structure, and deformation properties like the height of fission barriers and the excitation energy of the fission isomer. Using this new NEDF and another popular NEDF among fission practitioners, SkM*, a comprehensive study of fission dynamics with the TDSLDA formalism is presented. The role of pairing correlations in fission dynamics is demonstrated quantitatively. It is also shown that independent TDSLDA trajectories with different initial conditions on the potential energy surface generate almost the same fission fragment (FF) configurations, e.g. the mass split, total kinetic energy, total excitation energies, etc. An important aspect of this study is to provide a quantitative validation that the fission dynamics from saddle to scission is a non-adiabatic, over-damped one. To overcome the limitation of TDDFT that

fails to produce the variances in the FF properties, a novel method in the spirit of the classical Langevin approach is promoted to include fluctuations and dissipation into the TDDFT framework. Promising results are obtained in a simpler nuclear hydrodynamics simulation, while its implementation in a full TDSLDA calculation is still challenging.

TABLE OF CONTENTS

Page

Glossary . . . iii

Chapter 1: Introduction . . . 1
1.1 Nuclear fission: a brief history . . . 1
1.2 About this thesis . . . 10

Chapter 2: Theoretical Framework . . . 11
2.1 Density Functional Theory (DFT) . . . 11
2.2 Nuclear DFT and superfluid local density approximation (SLDA) . . . 14
2.3 Time-dependent superfluid local density approximatuon (TDSLDA) . . . 18

Chapter 3: Nuclear Energy Density Functional: SeaLL1 . . . 24
3.1 Bethe-Weizsäcker (BW) formula . . . 25
3.2 Form of SeaLL1 EDF . . . 27
3.3 Optimization . . . 34
3.4 Orbital-free functional . . . 37
3.5 Physical Properties . . . 38

Chapter 4: Fission Dynamics . . . 48
4.1 Simulation set-up . . . 49
4.2 Role of pairing correlations . . . 49
4.3 Results . . . 51
4.4 Summary . . . 62

Chapter 5: Fluctuations and Dissipations . . . 66
5.1 Introduction . . . 66
5.2 Theoretical formalism . . . 68

5.3 Results 72
5.4 Summary 79

Chapter 6: Conclusion and outlook 80

Appendix A: Numerical implementations 82
A.1 Discretization 82
A.2 The Coulomb potential 84
A.3 Static SLDA 87
A.4 TDSLDA 90

Appendix B: Parallelization and GPU acceleration 93
B.1 Static Code 93
B.2 Time-dependent Code 95

Appendix C: Performances of the codes 97

Bibliography 101

GLOSSARY

BW Bethe-Weizsäcker. 20

DFT *density functional theory*. 41, 42

DVR discrete variable representation. 74

EDF energy density functional. 14, 20, 39

EoS equation of state. 24, 30, 39

FFT fast Fourier transform. 47, 76

HFB *Hartree-Fock-Bogoliubov*. 16, 40

HK Hohenberg-Kohn. 11, 14

HO harmonic oscillator. 41

KS Kohn-Sham. 13

NEDF nuclear energy density functional. 14, 15, 20, 34, 40, 42, 43

NMP nuclear matter properties. 20

QMC quantum Monte Carlo. 39

SLDA *superfluid local density approximation*. 17

TDDFT *time-dependent density functional theory*. 17

TDSLDA *time-dependent superfluid local density approximation.* 19, 43, 44

ABM Adams-Bashforth-Milner. 46, 47

c.m. center of mass. 15, 35

DoF degrees of freedom. 55

N^{2}LO next-to-next-to leading order. 25

N^{3}LO next-to-next-to-next-to leading order. 25

rms root-mean-square. 34

SeaLL1 Seattle Lawrence-Livermore Functional. 30, 32–34, 38–40, 42

TDGCM time-dependent generator-coordinate method. 55, 60

TDRPA time-dependent random phase approximation. 60

TKE total kinetic energy. 52

TXE total excitation energy. 52, 53

ACKNOWLEDGMENTS

I would like to thank my supervisor Prof. Aurel Bulgac for his guidance, motivation and patience over the years. I am also grateful for the help from my collaborators Michael Forbes, Ionel Stetcu, Gabriel Wlazlowski, and Nicolas Schunck. I need to thank Kenneth Roche in particular for his guidance and support on my HPC knowledge and coding skills.

DEDICATION

to my dear wife, Jiayi

Chapter 1

INTRODUCTION

1.1 Nuclear fission: a brief history

Experiments on the bombardment of Uranium atoms (charge number Z=92) with neutrons performed by Hahn and Strassmann in 1938 [1] showed that lighter elements akin to Barium (Z=56) are formed in the reaction. This new type of nuclear reaction was given the name "fission" by Meitner and Frisch [2], who interpreted this phenomenon based on the liquid drop model (LDM), even before the publication of Hahn and Strassmann's paper in 1939. In Meitner and Frisch's paper [2], they made an analogy of the nuclear fission to a Coulomb-driven division of the classically charged incompressible liquid drop in competition with the surface tension of the liquid drop, and they obtained a good estimation of the total kinetic energy (TKE) of the fission fragments (FF) around 200 MeV. A few months later, Bohr and Wheeler quantified Meitner's arguments in their seminal paper [3] that introduced the compound model of nuclei in the mechanism of nuclear fission. According to this work, a low energy of incident neutron is captured by the Uranium nucleus and leads to the formation of a compound nucleus. After some time, the compound nucleus evolves from the initial state to the *saddle point*, which is the configuration where the Coulomb force is exactly balanced by the surface tension. The time scale of this process can be estimated by the uncertainty principle. The compound nucleus is hot when it is formed, thus the energy levels are very dense in its spectrum. The average spacing of energy levels is $\Delta E \approx 10$ eV in the n+Th reaction [4], then the time from the formation of the compound nucleus to the saddle point is $\tau_{GS} \approx \hbar/\Delta E \sim 10^7$ fm/c. From the saddle point to scission, the Coulomb force overwhelms the surface tension and the nucleus is driven to be separated. This process is much faster, with a typical time scale $\tau_{SS} \approx 10^3 \cdots 10^4$ fm/c. Figure 1.1 shows the total energy as a

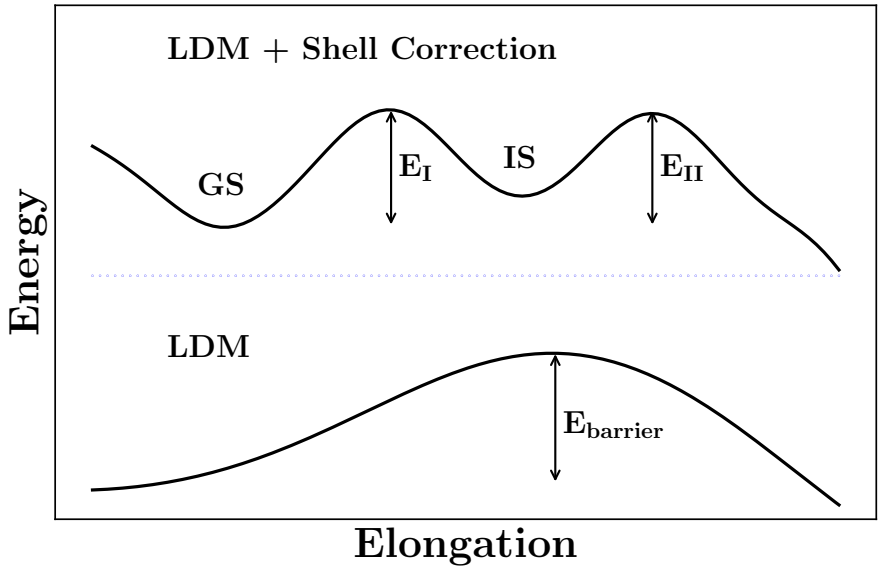

Figure 1.1: Potential energy surface (PES) of the nucleus in the fission process. Bottom: the PES obtained from the liquid drop model (LDM). Top: the PES obtained by LDM plus the shell correction. The ground state (GS), inner and outer fission barrier (E_{I} and E_{II}) and the fission isomer (IS) are denoted.

function of elongation of the nucleus in the fission process, which has a single-humped shape in the liquid drop model (bottom). The saddle point names the maximum of the curve.

Although the liquid drop model provides a phenomenological interpretation of fission, it can only predict a symmetric fission where two fragments have the same mass [3]. The distribution of FFs of Uranium demonstrates an asymmetric pattern in experiments. The liquid drop model is also a semi-classical theory and it ignores quantum effects, i.e. the individual behaviors of nucleons inside the nucleus. Evidence from the scattering experiments shows that the mean free path of the nucleon is at least the order of the size of the nucleus [4]. This fact indicates that to a good approximation, the nucleons in the nucleus can be treated as independent particles, which validates the establishment of the nuclear *shell model* [6, 7, 8]. In the shell model, nucleons are placed in quantized orbits and the strong spin-orbit interaction in the nucleus gives the energy spectrum its shell structure. Strutinsky proposed

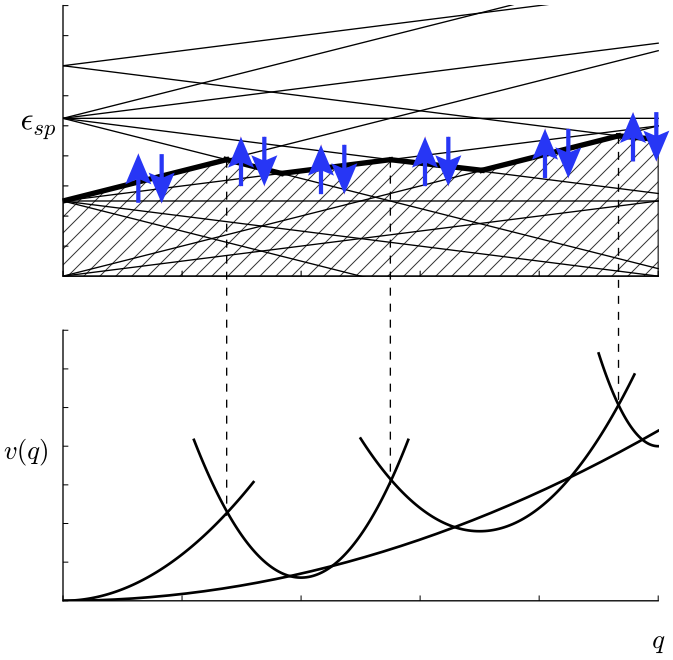

Figure 1.2: Schematic presentations of the single particle (s.p.) levels (upper) and of the total nuclear energy (lower) as a function of nuclear deformation[5]. The Fermi level is shown with a thick line and the up and down arrows represent the Kramer's degeneracy in each s.p. level.

a method to calculate the shell correction energy of the LDM by identifying the fluctuations of the single particle energies [9, 10]. The addition of this correction to the deformation energy obtained by the liquid drop model results in an oscillation on the potential energy surface. As shown in the top panel of Fig. 1.1, the PES has a double-humped shape, with a second minimum named the fission isomer (IS) [11, 12]. The shell effect also leads to a ground-state (GS) deformation for the Uranium nucleus.

In Hill and Wheeler's work [14], the emergence of the deformation energy in the fission process is discussed in a picture of individual particles. As shown in the bottom of Fig. 1.2, the potential energy as a function of deformation parameter $v(q)$, to a first approximation,

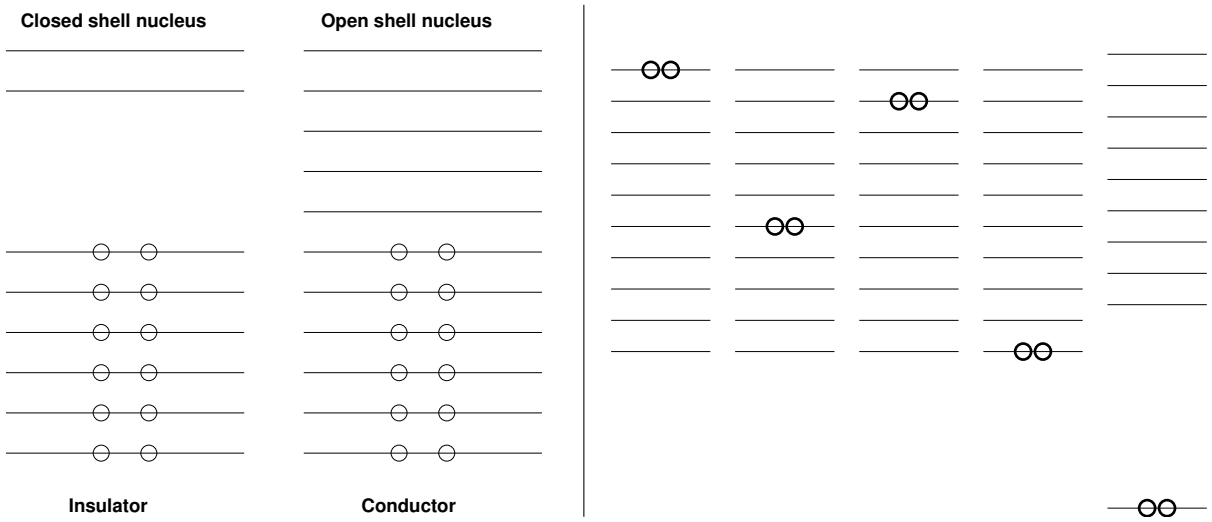

Figure 1.3: Left: Generic single-particle spectra of closed (insulators) and open shell (conductors) nuclei. Right: Cooper's picture of how a Cooper pair is formed [13].

can be viewed as the superposition of a series of parabolas. The bottom of each parabola represents a *Hartree-Fock* (HF) state with a constraint on the deformation q, which is the minimum energy of the nucleus for a certain deformation. The other points on the same parabola describe how the energy changes as the state deforms in the same single particle configuration. One finds that it is very energetic unfavorable if the nucleus stays at the same state as it deforms. The intersections of different states (parabolas) can be displayed as the crossing of single particle energy levels shown in the top of Fig. 1.2. Starting from the ground state ($q = 0$), each s.p. level increases or decreases according to the relative direction of its angular momentum and the deformation axis. In order to keep the total energy minimum, the nucleons on the top level (thick lines) need to jump from upsloping to downsloping levels at each level crossing. Due to the Kramers degeneracy [15], each single particle level is typically doubly degenerate, thus the nucleons will jump in pairs, i.e. transit from states $(m_1, -m_1)$ to $(m_2, -m_2)$. In the nucleus, the most effective mechanism to realize such a transition is the pairing interaction.

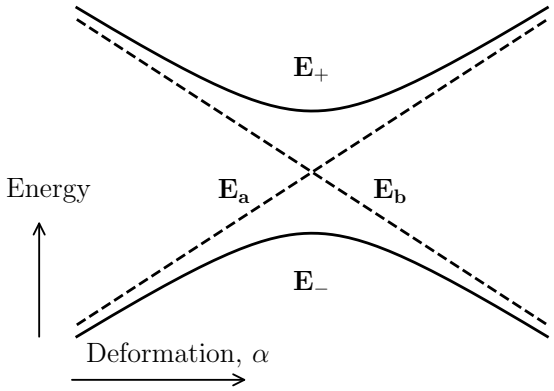

Figure 1.4: Behavior of two levels at a point of near cross-over, $\alpha = \alpha_0$ [14].

In open-shell nuclei, nucleons with opposite spins and (spatial) angular momenta can be paired due to the short-range residual interactions between them, like the Cooper pairs [16] of electrons in the theory of superconductivity [17]. The large number of degeneracy of the energy levels causes a considerable shift in the energy level of the paired nucleons and forms a bound state lower than the Fermi surface, as shown in Fig. 1.3. The presence of the pairing gap Δ between the bound state and the next excitation level makes the nucleus become a superfluid system. The influence of the pairing interaction on the level crossing can be studied in a schematic two-level system [14] shown in Fig. 1.4. Assuming two single particle levels: $E_a = E_0 + a(\alpha - \alpha_0), a > 0$ and $E_b = E_0 + b(\alpha - \alpha_0), b < 0$ cross at certain deformation parameter $\alpha = \alpha_0$ (dashed lines). The presence of a pairing gap will avoid the crossing of the two levels by adding the off-diagonal terms in the hamiltonian of the system:

$$H\psi = \begin{pmatrix} E_a & \Delta \\ \Delta^* & E_b \end{pmatrix} \psi = E\psi \tag{1.1}$$

with the eigenvalues $E_\pm = \frac{1}{2}(E_a + E_b) \pm \left[(\frac{1}{4}(E_a - E_b)^2 + |\Delta|^2\right]^{1/2}$ (solid lines). Therefore, the

nucleons residing on the lower level E_- will transit from the upsloping E_a adiabatically to the downsloping E_b with the probability $1 - P_D$, where P_D is the probability of the diabatic transition ($E_- \to E_+$), which can be calculated by the *Landau-Zener* formula [18]:

$$\begin{aligned} P_D &= e^{-2\pi\Gamma}, \\ \Gamma &= \frac{\Delta^2}{|\frac{\partial}{\partial t}(E_a - E_b)|} = \frac{\Delta^2}{|\frac{\partial \alpha}{\partial t}\frac{\partial}{\partial \alpha}(E_a - E_b)|}. \end{aligned} \tag{1.2}$$

For non-zero Δ, when the evolution of deformation is slow enough ($\frac{\partial \alpha}{\partial t} \ll 1$), $P_D \sim 0$ and the diabatic transition will be suppressed. When pairing is missing $\Delta = 0$, the nucleons will have the diabatic transition at the energy level crossing ($P_D = 1$) and the Fermi surface will become deformed [19, 20], which will cause a volume excitation energy for the system. This is in contrast to the fact that the nucleus is a saturation system and the deformation energy sources from the surface and Coulomb energies. Therefore, without the redistribution of nucleons on the single particle levels, the fission will be hindered. Negele [21] gives a model example as the fission of sulfur ^{32}S into two oxygens ^{16}O + ^{16}O in a mean-field method. The angular momentum distribution in the initial nucleus ^{32}S is $\pm 1/2^5, \pm 3/2^2, \pm 5/2^1$ (for each neutron or proton), including 20 positive and 12 negative parity s.p orbitals. However, in the final nuclei the angular momentum distribution becomes $\pm 1/2^6, \pm 3/2^2$ (for each neutron or proton), including 16 positive and 16 negative parity s.p. orbitals. Thus the pair of neutrons or protons $(5/2, -5/2)$ in ^{32}S transits into $(1/2, -1/2)$ in ^{16}O. In Negele's paper [21], this redistribution of nucleons is realized by breaking the axial symmetry of the mean field artificially, while introducing pairing can also enable such transitions without breaking the symmetry.

Overall, fission dynamics is one of the most challenging quantum many-body problems, and still lacks a full microscopic theory even 80 years after its discovery [22]. The *macroscopic-microscopic* (MM) method has been developed since 1970s [23, 24, 25, 26, 27, 28, 29, 30], and has remained a popular approach to statistical studies of fission fragments properties. In the MM method, a potential energy surface (PES) is calculated by the liquid drop model combined with shell correction, depending on a few number of variables that

describe various collective characters of the nucleus during the fission process, like the mass quadruple moment q_{20}, the octuple moment q_{30}, the thickness of the neck, etc. Then the classical Langevin equations for the collective variables are solved on the PES and the FF properties are derived by the configurations in the exit channel. The MM method can successfully reproduce the mass and charge distribution of FF in the experimental data when the number of collective variables is large enough, typically 5 in the recent studies [31, 32], which corresponds to around five million configurations on the PES. But the phenomenological nature and the limited number of collective degree of freedoms (DOF) make the prediction of the MM method restricted to only a few quantities. And the results are influenced considerably by the *ad hoc* modelings of inertia and friction used in the Langevin equations, which leaves uncertainties on its predictive power.

The full microscopic approach to the nuclear dynamics is to solve the many-body Schrödinger equation, which is still not applicable to heavy nuclei at present due to the huge number of DOFs involved. Self-consistent mean-field (SCMF) approaches like Hartree-Fock (HF) and Hartree-Fock-Bogoliubov (HFB) based on the nuclear energy density functionals (NEDF) have been developed and applied to study nuclei across the nuclear landscape. Their extensions to time-dependent problems [33] are straightforward and have been applied to various nuclear dynamics like nuclear vibrations and reactions [34, 35]. The study of fission dynamics using TDHF method goes back to the work by Negele *et al.* [36]. Due to computational limitations, the mean field was restricted with axial and reflection symmetry and the spin-orbit interaction was ignored. Pairing dynamics was solved in time-dependent BCS approximation with a constant pairing gap. Due to the reflection symmetry, only symmetric fission was obtained and the resulting total kinetic energy (TKE) had a strong dependence on the pairing gap. With the increase of computational power, the three-dimensional (3D) symmetry-unrestricted TDHF codes with full Skyrme EDFs [37, 38] have been utilized to fission dynamics in recent years [39, 40, 41, 42, 43]. In all of these simulations, the nucleus cannot fission unless the initial state is far beyond the saddle point where two fragments are already formed [39, 40, 41, 42], or given an initial boost with large energy [43], as shown in

Fig. 1.5. This phenomenon, named the "threshold anomaly", is due to the fact that in the TDHF formalism the pairing interaction is neglected and the occupation numbers of the single particle levels are frozen. Then the redistribution of nucleons is forbidden, which creates an insurmountable potential barrier and hinders the fission, as discussed earlier. Introducing the pairing dynamics in the TD-BCS formalism [40, 41] could vary the occupation numbers in the evolution, but the pairing field has a constant magnitude and its time-dependent phase can be removed by a trivial gauge transformation, with a modification of the chemical potential. TD-BCS also violates the continuity equation unless the occupation number is frozen [44], which returns to the case of TDHF. Therefore neither TDHF nor TDHF+BCS treats appropriately the pairing dynamics, which plays a critical role in the shape evolution of the saddle-to-scission process. This bottleneck was solved in the milestone work by Bulgac *et al.* [45], which realized for the first time the simulation of the induced fission of ^{240}Pu within a full microscopic framework, formally equivalent to the TDHFB method in 3D coordinate space without any symmetry restrictions. Starting from an initial state slightly beyond the outer fission barrier of ^{240}Pu, the nucleus goes to scission without any initial boosts and two excited fragments emerge. The heavy fragment has a spherical shape because its neutron/proton number is close to the double magic ^{132}Sn, while the lighter fragment is highly deformed. The evaluated FF properties like masses, charge numbers, and TKE are in good agreement with observations.

The breakthrough of the theoretical fission study in Ref. [45] relies on the simultaneous developments of both theoretical formalisms and computational techniques. In theory, the density functional theory (DFT) provides an equivalent alternative to the solution of the many-body Schrödinger equation. As the Hohenberg-Kohn (HK) theorem [46] proves, there is a one-to-one map between the ground state wavefunction, the number density, and the external field. Though initially established in the many-electron system, this theorem also applies to any non-relativistic many-fermion system. The Kohn-Sham scheme [47] provides a practical way to calculate the number density in a self-consistent way with quantum shell effects taken into account. With the local density approximation (LDA) treatment for the

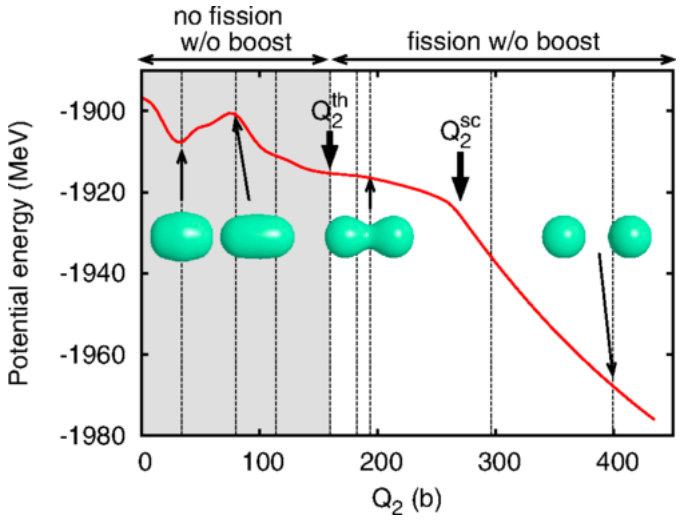

Figure 1.5: Initial conditions of fission dynamics with TDHF method on the PES. For the states with deformation (denoted as the quadruple moment Q_2) in shadowed region, the fission is forbidden without a boost for the wavefunctions [41].

exchange energy [47], one obtains a series of non-interacting Schrödinger equations, which has a similar form with the HF equations in the SCMF method. But different from SCMF, which depends on the independent particle approximation, DFT is an exact theory in nature. Due to the tremendous savings in computational work, DFT is widely used in quantum chemistry, solid state physics and many other many-electron systems. The main difficulty of applying DFT in nuclear system is that the *universal* EDF is unknown. Both the HK and KS theorems do not provide an algorithm to derive the EDF from the many-body Scrhödinger equation. Another complexity is the fact that nucleus is a superfluid system. The extension of DFT to superfluid system goes back to the work by Oliveira *et al.* [48]. However, that work used a non-local form for the pairing field, which hinders practical implementations. The work by Bulgac and Yu [49] provides a renormalization of the pairing field, which is named the superfluid local density approximation (SLDA) as an analogy to the LDA treatment in the KS scheme. The SLDA and its time-dependent extension, TDSLDA have been applied to various static and dynamical problems in cold atom and nuclear systems [50, 51, 52, 53, 54,

55, 56, 57, 58, 59, 60]. In computing, powerful supercomputers with petaflop performance makes large-scale TDSLDA calculations possible. In our typical implementations, nearly a million complex coupled time-dependent partial differential equations (PDE) are solved on large 3D lattices for up to 400,000 time steps. Over the years we have developed highly efficient MPI [61] + CUDA [62] codes, taking full advantage of the speed-up by the multi-core + GPU architectures on the top supercomputers [63] in the world, like Titan [64], Piz-Daint [65], and Summit [66].

1.2 About this thesis

This thesis is organized as follows. In chapter 2 we introduce DFT and TDDFT and their application to nuclear systems. In chapter 3 we introduce the nuclear energy density functional we developed for fission dynamics. In chapter 4, we report the results of simulations of fission dynamics with the TDSLDA method. In chapter 5 we introduce a novel formalism to include fluctuations and dissipation in the TDDFT framework. The conclusions and outlooks are summarized in chapter 6.

Chapter 2

THEORETICAL FRAMEWORK

2.1 Density Functional Theory (DFT)

A full microscopic theory of the nucleus should be given by the solution of the many-body Schrödinger equation

$$H\Psi(1,\cdots,A) = E\Psi(1,\cdots,A),$$
$$H = \overbrace{\sum_{i}^{A} -\frac{\hbar^2}{2m}\Delta_i}^{\hat{T}} + \overbrace{\sum_{i<j}^{A}\hat{V}_{ij} + \sum_{i<j<k}^{A}\hat{V}_{ijk}}^{\hat{W}} + \overbrace{\sum_{i}^{A}\hat{V}_{\mathrm{ext},i}}^{\hat{V}_{\mathrm{ext}}} \tag{2.1}$$

The hamiltonian $\hat{H}$ consists of the kinetic energy term $\hat{T}$, the interacting term $\hat{W}$ including the two-body ($\hat{V}_{ij}$) and three-body ($\hat{V}_{ijk}$) nuclear forces, and the external potential $\hat{V}_{\mathrm{ext}}$. The index i represents all coordinates of the ith nucleon, for instance,

$$(i) = (\vec{r}_i, s_i, t_i), \tag{2.2}$$

where $\vec{r}_i$ represents the spatial coordinates (x, y, z), s_i the spin freedom (up and down), and t_i the isospin freedom (proton and neutron). Solving Eq. (2.1) is a formidable task for a heavy nucleus considering its extremely large number of coordinates and degrees of freedom (DOF). For example, for ^{240}Pu, $\Psi(1,\cdots,A)$ has 720 spatial coordinates and $2^{240} \approx 1.77 \times 10 \times 10^{72}$ spin components. The theoretical tool we used in this thesis is the density functional theory (DFT), which provides a formalism equivalent to Eq. (2.1) and brings huge savings in the computational cost.

The formalism of DFT is based on the Hohenberg-Kohn (HK) theorem [46], which was established for the many-electron system, but it can be applied to any interacting fermion

systems, including the nucleus. Here we still use the terms in Eq. (2.1) for illustration. The HK theorem [67] establishes that there is a one-to-one map between three quantities:

(1) the ground-state wavefunction $\Psi(1, \cdots, A)$;

(2) the one-body (number) density

$$n(\vec{r}) = \langle\Psi|\hat{n}(\vec{r})|\Psi\rangle = \langle\Psi|\sum_s \hat{\psi}_s^\dagger(\vec{r})\hat{\psi}_s(\vec{r})|\Psi\rangle \tag{2.3}$$

where $\hat{\psi}_s(\vec{r})$ and $\hat{\psi}_s^\dagger(\vec{r})$ are the annihilation and creation operator for spin s ($\uparrow\downarrow$) at spatial coordinate $\vec{r}$.

(3) the external potential $\hat{V}_{\rm ext}$.

The map $n(\vec{r}) \Leftrightarrow \Psi[n] \Leftrightarrow \hat{V}_{\rm ext}$ suggests that the total energy of the system $E = \langle\Psi[n]|\hat{H}|\Psi[n]\rangle$ is a functional of $n(\vec{r})$:

$$E[n(\vec{r})] = \int d^3r \left[\mathcal{E}[n(\vec{r})] + n(\vec{r})V_{\rm ext}(\vec{r})\right], \tag{2.4}$$

where

$$\int d^3r\mathcal{E}[n(\vec{r})] = \langle\Psi[n]|\hat{T} + \hat{W}|\Psi[n]\rangle. \tag{2.5}$$

Since the map $n(\vec{r}) \Leftrightarrow \Psi[n]$ does not depend on $\hat{V}_{\rm ext}$, the form of $\mathcal{E}[n(\vec{r})]$ is *universal*, independent of the external potential. The ground state density $n_0(\vec{r})$ can be determined by the minimization of the energy $E[n(\vec{r})]$ with a constraint on the particle number N,

$$E_0 = \min_{n\in\mathcal{N}} E[n], \quad \mathcal{N} : N = \int d^3r n(\vec{r}), \tag{2.6}$$

or practically , via the variational principle

$$\frac{\delta}{\delta n(\vec{r})}\int d^3r \left\{\mathcal{E}[n(\vec{r})] + n(\vec{r})V_{\rm ext}(\vec{r}) - \mu n(\vec{r})\right\} = 0. \tag{2.7}$$

One main difficulty of applying Eq. (2.7) directly is that the kinetic energy $T[n] = \langle\Psi[n]|\hat{T}|\Psi[n]\rangle$ cannot be described explicitly in the terms of $n(\vec{r})$ in a finite interacting system. Efforts to derive $T[n]$ in terms of $n(\vec{r})$ have been made in many semi-classical approximations [68, 69]. The Thomas-Fermi (TF) approximation

$$T_0 = \int d^3r \frac{\hbar^2}{2m}\tau_0(\vec{r}), \quad \tau_0 = \frac{3}{5}(3\pi^2)^{2/3}n^{5/3}(\vec{r}) \tag{2.8}$$

is valid in infinite systems, but it cannot describe the surface of a finite system. The extended Thomas-Fermi (ETF) approximation

$$\tau_{\mathrm{ETF}} = \tau_0 + \left[\frac{1}{36}\frac{(\nabla n)^2}{n} + \frac{1}{3}\nabla^2 n\right] + \mathcal{O}\left[(\nabla n)^4\right] \tag{2.9}$$

can describe the surface, but it fails to account for the quantum oscillations brought about by the shell structure. Another difficulty is the exchange-correlation energy $\mathcal{E}_{\mathrm{xc}}[n]$ in the universal functional, due to the two-body correlations in fermion systems, is unknown and its non-locality will increase computational cost for any implementation. For sufficiently slowly varying density, the exchange-correlation energy can be treated in the *local density approximation* (LDA)

$$\mathcal{E}_{\mathrm{xc}}[n] = n(\vec{r})\epsilon_{\mathrm{xc}}[n(\vec{r})]. \tag{2.10}$$

The Kohn-Sham (KS) scheme [47] provides a practical approach to obtaining $n(\vec{r})$ that takes into account the shell effects. As the Kohn-Sham theorem proves, for any interacting system, there exists a non-interacting system that has the same ground state density, which can be obtained by solving the *Kohn-Sham equation* (the spin-freedom is neglected)

$$\left[\frac{\hbar^2}{2m}\nabla^2 + U(\vec{r}) + V_{\mathrm{ext}}(\vec{r})\right]\phi_i(\vec{r}) = \epsilon_i\phi_i(\vec{r}) \tag{2.11}$$

with

$$n(\vec{r}) = \sum_i |\phi_i(\vec{r})|^2. \tag{2.12}$$

where $\phi_i(\vec{r})$ is the s.p. wavefunction for the energy level ϵ_i. The kinetic energy is calculated as

$$T[n] = \int d^3r \frac{\hbar^2}{2m}\tau(\vec{r}), \quad \tau(\vec{r}) = \sum_i |\nabla\phi_i(\vec{r})|^2 \tag{2.13}$$

The local potential $U(\vec{r})$ is a functional of $n(\vec{r})$

$$U(\vec{r}) = \frac{\delta\mathcal{E}[n(\vec{r})]}{\delta n(\vec{r})} = \frac{\delta\left(n(\vec{r})\epsilon_{\mathrm{xc}}[n(\vec{r})]\right)}{\delta n(\vec{r})} + \text{other Hartree terms.} \tag{2.14}$$

Thus the KS equation needs to be solved self-consistently.

2.2 Nuclear DFT and superfluid local density approximation (SLDA)

Although the HK theorem proves that there exists a universal energy density functional (EDF) for any many-fermion system, it fails to provide a recipe for the construction of the EDF. The nucleus is a complex finite system and the nuclear energy density functional (NEDF) should contain the number density $n(\vec{r})$, the kinetic density $\tau(\vec{r})$ and the spin-orbit density that describes the spin-orbit interaction in the nucleus

$$\vec{J}(\vec{r}) = (-i) \sum_{k,s,s'} \phi_k^*(\vec{r}, s, \sigma) \left[\vec{\nabla} \phi_k(\vec{r}, s, \sigma) \times \vec{\sigma}_{ss'} \right], \tag{2.15}$$

where $\vec{\sigma}_{ss'}$ is the vector of *Pauli* matrices [15]. The gradient of the density $\nabla n(\vec{r})$ is also needed to describe the nuclear surface. As discussed in the introduction, the nucleons in the open shell with opposite angular momenta and spins form Cooper pairs due to short-range residual interactions, which makes the nucleus a superfluid system. Then the single particle wavefunctions in the KS equation Eq. (2.11) are reformulated into the quasi-particle wavefunctions (qpwfs) $\psi_{k,s}(\vec{r}) \Rightarrow [u_{k,s}(\vec{r}), v_{k,s}(\vec{r})]^T, s = \uparrow\downarrow$ via the *Bogoliubov* transformation [70]. The *anomalous density* works as an order parameter to signal the presence of Cooper pairs

$$\nu(\vec{r}) = \sum_k v_{k\uparrow}^*(\vec{r}) u_{k\downarrow}(\vec{r}) \sim \langle \Psi | \hat{\psi}_\uparrow(\vec{r}) \hat{\psi}_\downarrow(\vec{r}) | \Psi \rangle \tag{2.16}$$

And all the local densities in the normal system are rewritten as

$$n(\vec{r}) = \sum_{k,s} v_{k,s}^*(\vec{r}) v_{k,s}(\vec{r}), \tag{2.17a}$$

$$\tau(\vec{r}) = \sum_{k,s} \vec{\nabla} v_{k,s}^*(\vec{r}) \cdot \vec{\nabla} v_{k,s}(\vec{r}), \tag{2.17b}$$

$$\vec{J}(\vec{r}) = -i \sum_{k,s,s'} v_{k,s}^*(\vec{r}) \left[\vec{\nabla} v_{k,s}(\vec{r}) \times \vec{\sigma}_{s,s'} \right] \tag{2.17c}$$

Depending on the local densities defined above, a generic NEDF is represented as a sum of the kinetic $\mathcal{E}_{\text{kin}}$, the interaction $\mathcal{E}_{\text{nuclear}}$, the Coulomb $\mathcal{E}_{\text{Coul}}$, and the pairing $\mathcal{E}_{\text{pair}}$ contributions

$$\mathcal{E} = \mathcal{E}_{\text{kin}} + \mathcal{E}_{\text{nuclear}} + \mathcal{E}_{\text{Coul}} + \mathcal{E}_{\text{pair}}. \tag{2.18}$$

The kinetic energy density depends on the kinetic densities and the effective nucleon masses

$$\mathcal{E}_{\rm kin}(\vec{r}) = \sum_{q=n,p} \frac{\hbar^2 \tau_q(\vec{r})}{2m_q(\vec{r})}. \tag{2.19}$$

In some EDFs, the center of mass (c.m.) correction is included by replacing the bare nucleon mass m with $m/(1-1/A)$. The total particle number is $A = N + Z$ where N and Z are respectively the neutron (n) and proton (p) numbers. The Coulomb contribution is composed of the direct and the exchange energy densities

$$\begin{aligned} \mathcal{E}_{\rm Coul}(\vec{r}) &= \mathcal{E}^d_{\rm Coul}(\vec{r}) + \mathcal{E}^e_{\rm Coul}(\vec{r}) \\ &= \frac{e^2}{2} \int \frac{n_p(\vec{r}) n_p(\vec{r}')}{|\vec{r} - \vec{r}'|} d^3\vec{r}' - \frac{3e^2}{4} \left(\frac{3}{\pi}\right)^{1/3} n_p^{4/3}(\vec{r}). \end{aligned} \tag{2.20}$$

The pairing energy depends on the local anomalous density:

$$\mathcal{E}_{\rm pair}(\vec{r}) = \sum_{q=n,p} g_{\rm eff}(\vec{r}) |\nu_q(\vec{r})|^2 \tag{2.21}$$

and the effective pairing coupling strength $g_{\rm eff}(\vec{r})$ is obtained via a renormalization [49, 50, 71] of the bare pairing strength, typically parameterized as

$$g_0(\vec{r}) = g_0 \left(1 - \alpha \frac{n(\vec{r})}{n_0}\right), \tag{2.22}$$

where $n_0 = 0.16$ fm^{-3} is the nuclear saturation density. The parameter $\alpha = 0, 1, 1/2$ corresponds to volume, surface, and mixed pairing respectively [72, 73].

The interaction energy density is the most complicated. Over the years, many forms of the nuclear functional have been proposed; see Refs. [74, 75] for review. Among them the *Skyrme* family EDFs [74, 76] are rather popular and they have the generic form

$$\begin{aligned} \mathcal{E}_{\rm Skyrme} &= \mathcal{E}_{n^2} + \mathcal{E}_{n^\gamma} + \mathcal{E}_{n\Delta n} + \mathcal{E}_{n\tau} + \mathcal{E}_{n\nabla J} \\ &= \sum_{t=0,1} \left(C^n_t n_t^2 + C^\gamma_t n_t^2 n_0^\gamma + C^{n\Delta n}_t n_t \Delta n_t + C^\tau_t n_t \tau_t + C^{\nabla J}_t n_t \vec{\nabla} \cdot \vec{J}_t \right), \end{aligned} \tag{2.23}$$

where $n_0 = n_n + n_p$ and $n_1 = n_n - n_p$ (and similar for $\tau_{0,1}$ and $\vec{J}_{0,1}$) are the isoscalar and isovector densities respectively, and the C's are coupling constants.

Starting from the NEDF defined above, the components of the qpwfs $u_{k,s}(\vec{r})$ and $v_{k,s}(\vec{r})$ are obtained from the self-consistent solution to the formal *Hartree-Fock-Bogoliubov* (HFB) equation (for each neutron and proton)

$$\begin{pmatrix} h_{\uparrow\uparrow}(\vec{r})-\mu & h_{\uparrow\downarrow}(\vec{r}) & 0 & \Delta(\vec{r}) \\ h_{\downarrow\uparrow}(\vec{r}) & h_{\downarrow\downarrow}(\vec{r})-\mu & -\Delta(\vec{r}) & 0 \\ 0 & -\Delta^*(\vec{r}) & -h^*_{\uparrow\uparrow}(\vec{r})+\mu & -h^*_{\uparrow\downarrow}(\vec{r}) \\ \Delta^*(\vec{r}) & 0 & -h^*_{\downarrow\uparrow}(\vec{r}) & -h^*_{\downarrow\downarrow}(\vec{r})+\mu \end{pmatrix} \begin{pmatrix} u_{k\uparrow}(\vec{r}) \\ u_{k\downarrow}(\vec{r}) \\ v_{k\uparrow}(\vec{r}) \\ v_{k\downarrow}(\vec{r}) \end{pmatrix} = E_k \begin{pmatrix} u_{k\uparrow}(\vec{r}) \\ u_{k\downarrow}(\vec{r}) \\ v_{k\uparrow}(\vec{r}) \\ v_{k\downarrow}(\vec{r}) \end{pmatrix}. \quad (2.24)$$

The local particle-hole Hamiltonian $h_{\sigma,\sigma'}(\vec{r})$ is obtained by taking the appropriate functional derivatives of the energy density functional. For the Skyrme functional it takes the form [70]:

$$h_{\sigma,\sigma'}(\vec{r}) = \left(-\vec{\nabla}\cdot\frac{\hbar^2}{2m^*(\vec{r})}\vec{\nabla}+U(\vec{r})\right)\delta_{\sigma,\sigma'} - i\vec{W}(\vec{r})\cdot(\vec{\nabla}\times\vec{\sigma})_{\sigma,\sigma'}, \quad (2.25)$$

where $m^*(\vec{r})$ is the effective mass,

$$\frac{\hbar^2}{2m^*_q(\vec{r})} = \frac{\delta\mathcal{E}}{\delta\tau_q(\vec{r})} = \frac{\hbar^2}{2m} + C^\tau_0 n_0(\vec{r}) + \xi_q C^\tau_1 n_1(\vec{r}) \quad (2.26)$$

and ξ_q is the sign for isospin $q = n, p$: $\xi_n = 1, \xi_p = -1$. $U(\vec{r})$ is the central part of the mean-field potential,

$$\begin{aligned} U_q(\vec{r}) = \frac{\delta\mathcal{E}}{\delta n_q(\vec{r})} &= 2C^n_0 n_0 + 2\xi_q C^n_1 n_1 + C^\tau_0\tau_0 + \xi_q C^\tau_1\tau_1 \\ &+ 2C^{\Delta n}_0\nabla^2 n_0 + 2\xi_q C^{\Delta n}_1\nabla^2 n_1 \\ &+ C^{\nabla J}_0\vec{\nabla}\cdot\vec{J}_0 + \xi_q C^{\nabla J}_1\vec{\nabla}\cdot\vec{J}_1 \\ &+ C^\gamma_0(\gamma+2)n_0^{\gamma+1} + 2\xi_q C^\gamma_1 n_1 n_0^\gamma \end{aligned} \quad (2.27)$$

and $\vec{W}(\vec{r})$ is the spin-orbit potential:

$$\vec{W}_q(\vec{r}) = \frac{\delta\mathcal{E}}{\delta\vec{J}_q(\vec{r})} = C^{\nabla J}_0\vec{\nabla}n_0 + \xi_q C^{\nabla J}_1\vec{\nabla}n_1. \quad (2.28)$$

The local pairing field $\Delta(\vec{r})$ is defined as a function of the anomalous density

$$\Delta(\vec{r}) = -g_{\text{eff}}(\vec{r})\nu(\vec{r}). \quad (2.29)$$

Here we use a local form for both $\nu(\vec{r})$ and $\Delta(\vec{r})$, in contrast to the first attempt to applying DFT to superconducting system [48], where a non-local pairing potential $\Delta(\vec{r},\vec{r}')$ was used. One can show that the anomalous density $\nu(\vec{r},\vec{r}') = \sum_k v^*_{k\uparrow}(\vec{r})u_{k\downarrow}(\vec{r}') \sim \frac{1}{|\vec{r}-\vec{r}'|}$ diverges for $|\vec{r}-\vec{r}'| \to 0$. The pairing potential $\Delta(\vec{r})$ also diverges when $\nu(\vec{r})$ is a multiplicative factor of it $\Delta(\vec{r}) \sim g\nu(\vec{r})$ where g is the pairing coupling constant. The work by Bulgac and Yu [49] suggested a renormalization scheme of the pairing coupling strength to remove the divergence part in $\nu(\vec{r})$ and therefore in $\Delta(\vec{r})$. For a lattice system with energy cutoff E_c, the effective pairing strength $g_{\text{eff}}(\vec{r})$ in Eq. (3.25) is defined as

$$\frac{1}{g_{\text{eff}}(\vec{r})} = \begin{cases} \frac{1}{g_0(\vec{r})} - \frac{m^*(\vec{r})k_c(\vec{r})}{2\pi^2\hbar^2}\left(1 - \frac{k_F(\vec{r})}{2k_c(\vec{r})}\ln\frac{k_c(\vec{r})+k_F(\vec{r})}{k_c(\vec{r})-k_F(\vec{r})}\right), & k_F^2(\vec{r}) \geq 0 \\ \frac{1}{g_0(\vec{r})} - \frac{m^*(\vec{r})k_c(\vec{r})}{2\pi^2\hbar^2}\left(1 + \frac{|k_F(\vec{r})|}{k_c(\vec{r})}\arctan\frac{|k_F(\vec{r})|}{k_c(\vec{r})}\right), & k_F^2(\vec{r}) < 0 \end{cases} \tag{2.30a}$$

$$E_c = \frac{\hbar^2 k_c^2(\vec{r})}{2m} + U(\vec{r}) - \mu, \tag{2.30b}$$

$$\mu = \frac{\hbar^2 k_F^2(\vec{r})}{2m} + U(\vec{r}). \tag{2.30c}$$

Note that Eq. (2.30) is derived in 1D spherical momentum space and when discretized the energy cutoff E_c should be smaller than the natural energy cutoff of the lattice $\frac{\hbar^2\pi^2}{2ma^2}$ where a is the lattice constant. In 3D Cartesian coordinates with $dx = dy = dz$ the natural energy cutoff becomes $\frac{\hbar^2\pi^2}{2mdx^2} + \frac{\hbar^2\pi^2}{2mdy^2} + \frac{\hbar^2\pi^2}{2mdz^2} = 3\frac{\hbar^2\pi^2}{2mdx^2}$ and for $E_c > \frac{\hbar^2\pi^2}{2mdx^2}$ Eq. (2.30) becomes inapplicable. An expression of $g_{\text{eff}}(\vec{r})$ on a 3D lattice with the natural energy cutoff $3\frac{\hbar^2\pi^2}{2mdx^2}$ is suggested in Ref. [77] and Chapter 5 of Ref. [78]

$$\frac{1}{g_{\text{eff}}(\vec{r})} = \frac{1}{g_0(\vec{r})} - \frac{m^*(\vec{r})}{4\pi^2\hbar^2}\frac{\pi}{dx}K \tag{2.31}$$

where K is a numerical constant given by

$$K = \frac{12}{\pi}\int_0^{\pi/4} d\theta \ln(1 + 1/\cos^2\theta) = 2.442\ 749\ 607\ 806\ 335\cdots.$$

This formalism of localizing the pairing field is named the *superfluid local density approximation* (SLDA) in analogy to the LDA treatment in the KS scheme. Similarly, Eq. (2.24) is also named the SLDA equation.

2.3 Time-dependent superfluid local density approximatuon (TDSLDA)

The extension of DFT to time-dependent problems, *time-dependent density functional theory* (TDDFT) was promoted by Runge and Gross [33], who proved that for the time-dependent Schrödinger equation

$$i\hbar\frac{\partial}{\partial t}\Psi(1,\cdots,A,t)=\left\{\sum_{i=1}^{A}-\frac{\hbar^2}{2m}\Delta_i+V(1,\cdots,A,t)\right\}\Psi(1,\cdots,A,t), \tag{2.32}$$

the time-dependent wavefunction $\Psi(1,\cdots,A,t)$ is still a functional of the time-dependent density $n(\vec{r},t)$, which can be solved by the time-dependent KS equation

$$i\hbar\frac{\partial}{\partial t}\phi_k(\vec{r},t)=\left[-\frac{\hbar^2}{2m}\nabla^2+V_{\rm KS}(\vec{r},t)\right]\phi_k(\vec{r},t) \tag{2.33}$$

with

$$n(\vec{r},t)=\sum_k|\phi_k(\vec{r},t)|^2 \tag{2.34}$$

and the corresponding current density

$$\vec{j}(\vec{r},t)=\sum_k\frac{1}{2i}\left[\phi_k^*(\vec{r},t)\nabla\phi_k(\vec{r},t)-\phi_k(\vec{r},t)\nabla\phi_k^*(\vec{r},t)\right]. \tag{2.35}$$

In nuclear systems, the interaction part of the (Skyrme) NEDF needs to include time-odd terms to satisfy Galilean invariance

$$\begin{aligned}\mathcal{E}_{\rm Skyrme}&=\mathcal{E}_{n^2}+\mathcal{E}_{n^\gamma}+\mathcal{E}_{n\Delta n}+\mathcal{E}_{n\tau}+\mathcal{E}_{n\nabla J}\\&=\sum_{t=0,1}C_t^n n_t^2+C_t^\gamma n_t^2 n_0^\gamma+C_t^{n\Delta n}n_t\Delta n_t\\&+C_t^\tau(n_t\tau_t-\vec{j}_t\cdot\vec{j}_t)+C_t^{\nabla J}(n_t\vec{\nabla}\cdot\vec{J}_t+\vec{s}_t\cdot(\vec{\nabla}\times\vec{j}_t))\end{aligned} \tag{2.36}$$

while the form of other parts of NEDF is not changed. The total energy density is a functional

of the time-dependent local densities introduced earlier (for each neutron and proton)

$$n(\vec{r},t) = \sum_{k,s} v^*_{k,s}(\vec{r},t)v_{k,s}(\vec{r},t), \tag{2.37a}$$

$$\nu(\vec{r},t) = \sum_{k} v^*_{k\uparrow}(\vec{r},t)u_{k\downarrow}(\vec{r},t), \tag{2.37b}$$

$$\tau(\vec{r},t) = \sum_{k,s} \vec{\nabla} v^*_{k,s}(\vec{r},t)\cdot\vec{\nabla} v_{k,s}(\vec{r},t), \tag{2.37c}$$

$$\vec{s}(\vec{r},t) = \sum_{k,s,s'} \vec{\sigma}_{ss'} v^*_{k,s}(\boldsymbol{r},t)v_{k,s'}(\boldsymbol{r},t), \tag{2.37d}$$

$$\vec{J}(\vec{r},t) = \frac{1}{2i}(\vec{\nabla}-\vec{\nabla}')\times\vec{s}(\vec{r},\vec{r}',t)\Big|_{\vec{r}=\vec{r}'}, \tag{2.37e}$$

and the current density

$$\vec{j}(\vec{r},t) = \frac{1}{2i}\sum_{k,s}\left[v_{k,s}(\vec{r},t)\vec{\nabla}v^*_{k,s}(\vec{r},t) - v^*_{k,s}(\vec{r},t)\vec{\nabla}v_{k,s}(\vec{r},t)\right] \tag{2.38}$$

where the components $u_{k,s}(\vec{r},t), v_{k,s}(\vec{r},t)$ are obtained by solving the *time-dependent superfluid local density approximation* (TDSLDA) equation

$$i\hbar\frac{\partial}{\partial t}\begin{pmatrix} u_{k\uparrow}(\boldsymbol{r},t)\\ u_{k\downarrow}(\boldsymbol{r},t)\\ v_{k\uparrow}(\boldsymbol{r},t)\\ v_{k\downarrow}(\boldsymbol{r},t)\end{pmatrix} = \begin{pmatrix} h_{\uparrow\uparrow}(\boldsymbol{r},t)-\mu & h_{\uparrow\downarrow}(\boldsymbol{r},t) & 0 & \Delta(\boldsymbol{r},t)\\ h_{\downarrow\uparrow}(\boldsymbol{r},t) & h_{\downarrow\downarrow}(\boldsymbol{r},t)-\mu & -\Delta(\boldsymbol{r},t) & 0\\ 0 & -\Delta^*(\boldsymbol{r},t) & -h^*_{\uparrow\uparrow}(\boldsymbol{r},t)+\mu & -h^*_{\uparrow\downarrow}(\boldsymbol{r},t)\\ \Delta^*(\boldsymbol{r},t) & 0 & -h^*_{\downarrow\uparrow}(\boldsymbol{r},t) & -h^*_{\downarrow\downarrow}(\boldsymbol{r},t)+\mu\end{pmatrix}\begin{pmatrix} u_{k\uparrow}(\boldsymbol{r},t)\\ u_{k\downarrow}(\boldsymbol{r},t)\\ v_{k\uparrow}(\boldsymbol{r},t)\\ v_{k\downarrow}(\boldsymbol{r},t)\end{pmatrix}. \tag{2.39}$$

The s.p. hamiltonian has the generic form

$$\begin{aligned} h_{\sigma,\sigma'}(\vec{r}) = &\left(-\vec{\nabla}\cdot\frac{\hbar^2}{2m^*(\vec{r})}\vec{\nabla}+U(\vec{r})\right)\delta_{\sigma,\sigma'} - i\vec{W}(\vec{r})\cdot(\vec{\nabla}\times\vec{\sigma})_{\sigma,\sigma'}\\ &+\vec{U}_\sigma(\vec{r})\cdot\vec{\sigma}+\frac{1}{i}\left(\vec{\nabla}\cdot\vec{U}_\Delta(\vec{r})+\vec{U}_\Delta(\vec{r})\cdot\vec{\nabla}\right), \end{aligned} \tag{2.40}$$

where

$$\vec{U}_\sigma(\vec{r}) = C^{\nabla J}\vec{\nabla}\times\vec{j}, \tag{2.41}$$

$$\vec{U}_\Delta(\vec{r}) = C^{\tau}\vec{j}+\frac{1}{2}C^{\nabla J}\vec{\nabla}\times\vec{s}, \tag{2.42}$$

and $m^*(\vec{r})$, $U(\vec{r})$, $\vec{W}(\vec{r})$ and $\Delta(\vec{r})$ have the same form as in Eq. (2.26), Eq. (2.27), Eq. (2.28) and Eq. (2.29).

2.3.1 External boosts and external potentials

In studies of nuclear reactions and giant resonances, the nucleus is "boosted" at the beginning of the evolution to gain certain initial velocities or other collective flows. Such boost is realized by performing a $U(1)$ gauge transformation on each qpwf as

$$\begin{pmatrix} u_k(\vec{r},t) \\ v_k(\vec{r},t) \end{pmatrix} \rightarrow \begin{pmatrix} e^{i\chi} & 0 \\ 0 & e^{-i\chi} \end{pmatrix} \begin{pmatrix} u_k(\vec{r},t) \\ v_k(\vec{r},t) \end{pmatrix} \tag{2.43}$$

The spatial profile $\chi(\vec{r})$ should be chosen appropriately for different situations. For example. when $\chi(\vec{r}) = \vec{p}\cdot\vec{r}/\hbar$, the nucleus will gain an initial velocity $\hbar\vec{\nabla}\chi/M = \vec{p}/M$ where M is the total mass of the nucleus.

In addition, during the evolution, the system can also be coupled to external excitation fields in both scalar and vector channels

$$\hat{h}_q \rightarrow \hat{h}_q + U^0_{q,\mathrm{ext}}(\vec{r},t) - \frac{1}{2}(\vec{U}_{q,\mathrm{ext}}\cdot\hat{\vec{p}} + \hat{\vec{p}}\cdot\vec{U}_{q,\mathrm{ext}}). \tag{2.44}$$

Different choices for the external potentials allow one to study the response of the nuclear system to different probes.

2.3.2 Center of mass motion and rotation

The presence of external potentials or boosts sometimes leads to center of mass motions and rotations of the system. In order to follow the internal motion of nucleus in the moving and rotating frame, we need to introduce extra terms in the hamiltonian to balance these collective motions [79]. For the center of mass motion, we perform a transformation for each qpwf as

$$\phi_n(\vec{r},t) = \exp\left[\frac{i\vec{R}(t)\cdot\hat{\vec{p}}}{\hbar}\right]\psi_n(\vec{r},t) \tag{2.45}$$

where $\vec{R}(t)$ describes the center of mass motion and $\hat{\vec{p}}$ is the momentum operator. The equation of motion for ϕ_n becomes

$$i\hbar\dot{\phi}_n(\vec{r},t) = [\hat{H} - \vec{v}\cdot\hat{\vec{p}}]\phi_n(\vec{r},t) \tag{2.46}$$

where $\vec{v} = \dot{\vec{R}}(t)$ is the velocity of the c.m. motion. In practice it can also be calculated as

$$\vec{v} = \frac{\hbar}{M}\int d^3r\vec{j}(\vec{r},t) \tag{2.47}$$

where $\vec{j}(\vec{r},t) = \vec{j}_n(\vec{r},t) + \vec{j}_p(\vec{r},t)$ is the total current density and M is the total mass of the nucleus.

Similar to the center of mass motion, the rotation of the system can also be balanced by making a transformation on the qpwfs such that

$$\phi_n(\vec{r},t) = \exp\left[\frac{i\vec{\theta}(t)\cdot\hat{\vec{j}}}{\hbar}\right]\psi_n(\vec{r},t) \tag{2.48}$$

where $\vec{\theta}(t) = \theta_0\hat{\theta}$ is the vector of rotation angles for the system with respect to the z-axis and $\hat{\vec{j}}$ is the total angular momentum operator

$$\hat{\vec{j}} = \hat{\vec{l}} + \hat{\vec{s}}, \quad \hat{\vec{l}} = \hat{\vec{r}}\times\hat{\vec{p}}. \tag{2.49}$$

The determination of $\vec{\theta}$ is as follows. We calculate the mass quadrupole matrix of the system as

$$Q_{ij} = \int d^3r\vec{r}_i\vec{r}_j n(\vec{r}), \quad i,j = x,y,z \tag{2.50}$$

Diagonalizing Q we obtain the rotation matrix R

$$Q = RDR^T, \tag{2.51}$$

which has a structure

$$R_{ik} = \cos\theta_0\delta_{ik} + (1-\cos\theta_0)n_in_k - \sin\theta_0\varepsilon_{ikl}n_l \tag{2.52}$$

where (n_x, n_y, n_z) is the unit vector of rotation axis $\hat{\theta}$. They can be determined by the following relations

$$\text{tr } R = 1 + 2\cos\theta_0, \quad R - R^T = 2\sin\theta_0 \begin{pmatrix} 0 & -n_z & n_y \\ n_z & 0 & -n_x \\ -n_y & n_x & 0 \end{pmatrix} \tag{2.53}$$

In practice, we usually ignore the rotation along the z axis,then the rotation angle can be determined simply as

$$\vec{\theta} = \vec{R}_3 \times \hat{z} \tag{2.54}$$

where $\vec{R}_3$ is the third column of the R matrix and $\hat{z} = (0, 0, 1)^T$ is the unit vector in the z-direction. The equation of motion for ϕ_n reads

$$i\hbar\dot{\phi}_n(\vec{r}, t) = [\hat{H} - \vec{\omega} \cdot \hat{\vec{j}}]\phi_n(\vec{r}, t) \tag{2.55}$$

where $\vec{\omega}(t) = \dot{\vec{\theta}}(t)$ is the angular velocity.

2.3.3 Miscellaneous quantities

Some other quantities are also calculated in the TDSLDA calculations.

- The center of mass

$$\vec{r}_{\text{cm}} = \frac{\int d^3r\vec{r}n(\vec{r})}{\int d^3rn(\vec{r})}. \tag{2.56}$$

- Deformation parameters

$$Q_{lm} = \int d^3r\hat{Q}_{lm}n(\vec{r}), \quad \hat{Q}_{lm} \propto r^l Y_{lm} \tag{2.57a}$$

where Y_{lm} is the spherical harmonics function, and

$$\hat{Q}_{20} = (2z'^2 - x'^2 - y'^2), \tag{2.57b}$$

$$\hat{Q}_{30} = z'(2z'^2 - 3x'^2 - 3y'^2), \tag{2.57c}$$

$$\hat{Q}_{40} = 35z'^4 - 30z'^2r'^2 + 3r'^4, \tag{2.57d}$$

with $x' = x - x_{\rm cm}, y' = y - y_{\rm cm}, z' = z - z_{\rm cm}$ and $r'^2 = x'^2 + y'^2 + z'^2$.

- The average pairing gap

$$\langle \Delta_q \rangle = \frac{\int d^3r |\Delta_q(\vec{r})| n_q(\vec{r})}{\int d^3r n_q(\vec{r})}, \tag{2.58}$$

- The collective flow energy

$$E_{\rm coll} = \sum_q \int d^3r \frac{\hbar^2}{2m} \vec{j}_q^2(\vec{r}), \tag{2.59}$$

- The center of mass kinetic energy

$$E_{\rm cm} = \frac{1}{2} m \vec{v}_{\rm cm}^2. \tag{2.60}$$

Chapter 3

NUCLEAR ENERGY DENSITY FUNCTIONAL: SEALL1

DFT proves that there exists a *universal* EDF for any fermion systems. However, it does not provide a recipe for the construction of EDF. Early NEDFs are derived in the mean-field picture, as the expectation value of effective nuclear Hamiltonians on the Slater determinant of single particle wavefunctions, such as the Skyrme and Gogny EDFs [76]. There exists more than 300 NEDFs at present, which depend on a large number of phenomenological fitting parameters (typically 14 and sometimes even more). However, among these parameters, only some parameters or their combinations are uncorrelated, which makes it difficult to study the relations between parameters and various nuclear properties.

A good NEDF should be able to describe the following nuclear properties correctly: the infinite nuclear matter properties (NMP); the surface and radius of the nucleus; the shell structure, due to the spin-orbit interaction in the nuclear force; the deformation properties. We have developed a qualitatively new NEDF, which contains only 7 uncorrelated parameters [80]. Our strategy of constructing the NEDF is based on the Bethe-Weizsäcker (BW) formula in the liquid drop model (LDM) [70], which gives an excellent description of the bulk properties of nuclei. Following the spirit of Hohenberg-Kohn [46], an orbital-free functional of neutron and proton density is established based on four dominant parameters and it obtains a global mass fit better than the four-parameter BW formula. Based on this parameterization, the shell effects are then introduced in the Kohn-Sham scheme [47], taking into account the spin-orbit and pairing interaction in the SLDA formalism. This resulting orbital-based functional, named *SeaLL1*, has excellent performances on all the nuclear properties mentioned above. In this chapter [1], we have a brief review of the LDM first, and

[1]This chapter is based on the work by A. Bulgac, Michael McNeil Forbes, Shi Jin, Rodrigo Navarro Perez,

introduce the form of SeaLL1 EDF then. Finally, the physical properties of SeaLL1 EDF are also discussed.

3.1 Bethe-Weizsäcker (BW) formula

In the liquid drop model, the mass of an atomic nucleus consisting N neutrons and Z protons is given by ($c = 1$)

$$m = Zm_p + Nm_n - E_B \tag{3.1}$$

where m_p and m_n are the rest mass of a proton and neutron. The term E_B is the binding energy of the nucleus, which can be evaluated by the *Bethe-Wezsäscker formula*

$$\begin{aligned} E_B(N,Z) &= a_V A - a_S A^{2/3} - a_C \frac{Z^2}{A^{1/3}} - a_A \frac{(N-Z)^2}{A} + \delta(A) \\ a_V &= 15.68, a_S = 18.56, a_C = 0.717, a_A = 28.1 \quad [\text{MeV}] \\ \delta(A) &= \begin{cases} 12A^{-1/2} & \text{even-even nuclei,} \\ 0 & \text{odd nuclei,} \\ -12A^{-1/2} & \text{odd-odd nuclei.} \end{cases} \end{aligned} \tag{3.2}$$

The physical meaning of the formula Eq. (3.2) is as follows. The first term is usually called the *volume term* because it's proportional to A ($\propto R^3$) thus the volume of the nucleus. The second term is called the *surface term*, which is proportional to $A^{2/3}$ ($\propto R^2$) thus the surface area of the nucleus. The nucleons on the surface feel the attractive net force towards inside. One can relate this term to the surface energy of a liquid drop via

$$a_S A^{2/3} = \sigma S, \quad \sigma = \frac{a_S}{4\pi r_0^2}, \tag{3.3}$$

which yields a value of the surface tension $\sigma \approx 1$ MeV. The third term is the *Coulomb term*, which accounts the Coulomb repulsion of the protons. Assuming a uniformly distributed

---

and Nicolas Schunck, *Minimal nuclear energy density functional*, Phys. Rev. C. 97, 04413 (2018) [80] with minor modifications.

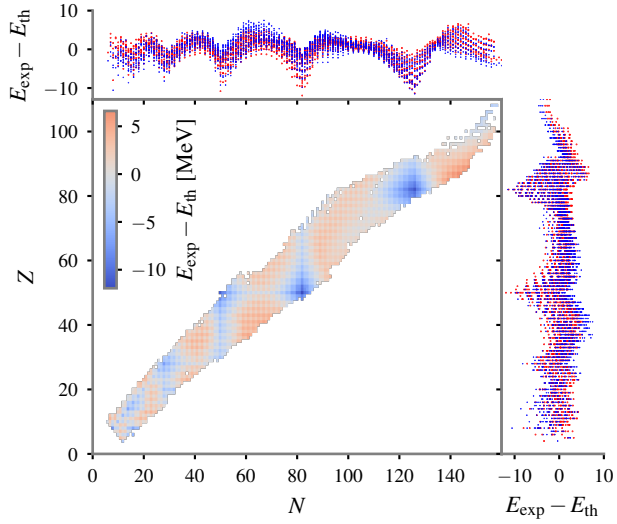

Figure 3.1: The differences $E_{\rm exp} - E_{\rm th}$ in MeVs between the evaluated ground state energies $E_{\rm exp}(N, Z)$ [81, 82] of 2375 nuclei with $A \geq 16$ and fitted with the Liquid Drop Model. One can easily identify the location of closed shells (the blue regions) for protons and neutrons.

charge sphere, this energy is proportional to Z^2 and inversely proportional to the radius $R \propto A^{1/3}$. The fourth term, which is called the *symmetry term*, results from the isospin dependent term in nuclear force and the Pauli principle (in the kinetic energy). The last term is the *pairing term*, which sources from the pairing interactions in the nucleus and causes an odd-even staggering pattern in the nuclear masses [4].

The Liquid Drop Model provides a good estimation of nuclear masses throughout the nuclear chart. Fig. 3.1 shows the differences in MeVs between the evaluated ground state energies $E_{\rm exp}(N, Z)$ in AME 2012 atmoc mass evaluations [81, 82], and the fitted with the LDM $E_{\rm th}$. Here both $E_{\rm exp}$ and $E_{\rm th}$ should be interpreted as $-E_B$. Compared to 2375 measured nuclei ($A \geq 16$), the LDM gives an rms mass error $\chi_E \approx 3$ MeV per nucleus. This is a remarkable result: the nuclear binding energy of heavy nuclei can reach 2000 MeV; hence the errors are at the sub-percent level. The maximum error occurs in the neighborhood of magic or semi-magic nuclei, due to the missing of shell effects in the LDM. In the next

section, we will describe a NEDF that depends on the smallest number of phenomenological parameters needed to account for all the contributions in the BW formula.

3.2 Form of SeaLL1 EDF

The SeaLL1 EDF consists of three parts, the kinetic energy density $\mathcal{E}_{\text{kin}}$, the Coulomb energy density $\mathcal{E}_{\text{Coulomb}}$ and the interaction energy density $\mathcal{E}_{\text{int}}$

$$\mathcal{E}[n(\vec{r}), \tau(\vec{r}), \vec{J}(\vec{r}), \vec{\nabla} n(\vec{r}), \nu(\vec{r})] = \mathcal{E}_{\text{kin}} + \mathcal{E}_{\text{Coulomb}} + \mathcal{E}_{\text{int}} \tag{3.4}$$

where the local densities $n(\vec{r}), \tau(\vec{r}), \vec{J}(\vec{r}), \nu(\vec{r})$ are defined in Eq. (2.16) Eq. (2.17) for each neutron and proton. The kinetic energy density and Coulomb energy density are well defined and there is no free parameter in them. All the phenomenological parameters are in the interacting term $\mathcal{E}_{\text{int}}$, which consists of the homogeneous term $\mathcal{E}_{\text{homo}}$, the gradient term $\mathcal{E}_{\text{grad}}$, the spin-orbit term $\mathcal{E}_{\text{so}}$ and the pairing term $\mathcal{E}_{\text{pair}}$

$$\mathcal{E}_{\text{int}} = \mathcal{E}_{\text{homo}} + \mathcal{E}_{\text{grad}} + \mathcal{E}_{\text{so}} + \mathcal{E}_{\text{pair}} \tag{3.5}$$

3.2.1 Kinetic term

The kinetic energy density is the same with the one for a noninteracting system.

$$\mathcal{E}_{\text{kin}} = \frac{\hbar^2}{2m}(\tau_n + \tau_p), \quad m = \frac{m_n + m_p}{2} \tag{3.6}$$

Due to the mass difference between neutron and proton $\delta m = m_n - m_p$, there is a difference between Eq. (3.6) and the exact form

$$\mathcal{E}_{\text{kin}} = \frac{\hbar^2}{2m_n}\tau_n + \frac{\hbar^2}{2m_p}\tau_p = \frac{\hbar^2}{2m}(\tau_n + \tau_p) - \frac{\delta m}{2m}\frac{\hbar^2}{2m}(\tau_n - \tau_p) + \mathcal{O}\left(\frac{\delta m}{2m}\right)^2 \tag{3.7}$$

But the correction is very small since $\delta m/m < 10^{-3}$ and is neglected in common practice.

3.2.2 Coulomb term

The Coulomb energy density consists of the direct and exchange parts

$$\mathcal{E}_{\text{Coulomb}} = \frac{1}{2} V_{\text{C}}(\vec{r}) n_{\text{ch}}(\vec{r}) - \frac{3e^2}{4} \left(\frac{n_p(\vec{r})}{3\pi} \right)^{4/3}, \tag{3.8a}$$

$$V_{\text{C}}(\vec{r}) = e^2 \int d^3\vec{r}' \frac{n_{\text{ch}}(\vec{r}')}{|\vec{r} - \vec{r}'|} \tag{3.8b}$$

where e is the proton charge and n_{ch} is the charge density, which is obtained from the proton and neutron densities by convolution (here denoted with an asterisk, *) with the appropriate charge form factors:

$$n_{\text{ch}} = G_E^n * n_n + G_E^p * n_p. \tag{3.9}$$

Including the form factors does not significantly improve the fit of masses but improves somewhat the fit of the charge radii. Here we leave $G_E^n = 0$ and $G_E^p = 1$ thus $n_{\text{ch}}(\vec{r}) = n_p(\vec{r})$. In principle, one might allow the coefficient of the Coulomb exchange term to vary; this is done, for example, in atomic physics in order to obtain better estimates of the Coulomb exchange energy. We find, however, that fitting the nuclear binding energies leads with high accuracy to the same coefficient presented in Eq. (3.8a), so we leave it fixed and do not include this as a parameter in our model.

3.2.3 Homogeneous terms: Infinite nuclear and neutron matter

The homogeneous terms describe the equation of state (EoS) of the homogeneous infinite nuclear matter,

$$\begin{aligned} \mathcal{E}_{\text{homo}} &= \sum_{j=0}^{2} (a_j n^{5/3} + b_j n^2 + c_j n^{7/3}) \beta^{2j} \\ n &= n_n + n_p, \quad \beta = \frac{n_n - n_p}{n_n + n_p}. \end{aligned} \tag{3.10}$$

in which the spin-orbit, gradient, and Coulomb term vanish, and the semiclassical expansion of the kinetic energy density $\mathcal{E}_{\text{kin}}$ becomes exact in the leading Thomas-Fermi term Eq. (2.8).

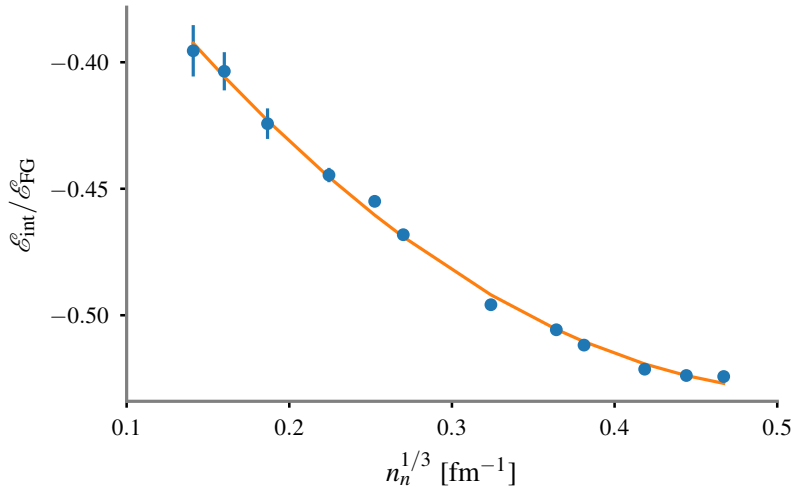

Figure 3.2: The QMC results of Wlazłowski *et al.* [83] for the interaction energy per neutron displayed as the ratio $\mathcal{E}_{\rm int}/\mathcal{E}_{\rm FG}$ defined in Eq. (3.12b) (with $\beta = 1$), where $\mathcal{E}_{\rm FG} = 3\hbar^2(3\pi^2)^{2/3}n_n^{5/3}/(10m_n)$. If $a_n = 0$ in Eq. (3.12b), the ratio $\mathcal{E}_{\rm int}/\mathcal{E}_{\rm FG}$ would tend to 0 for $n_n \to 0$.

Thus, neglecting the small mass difference between neutrons and protons $m_n \approx m_p \approx m$, the functional has the simple form:

$$\mathcal{E}(n_n, n_p) = \frac{3\hbar^2(3\pi^2)^{2/3}}{10m}\left(n_n^{5/3} + n_p^{3/2}\right) + \sum_{j=0}^{2}(a_j n^{5/3} + b_j n^2 + c_j n^{7/3})\beta^{2j}. \tag{3.11}$$

This portion of functional is essentially an expansion in powers of the Fermi momenta $k_F : k_{n,p} = (3\pi^2 n_{n,p})^{1/3}$ with only three terms k_F^5, k_F^6, k_F^7. This type of expansion is ubiquitous in many-body perturbation theory, and also applies to fitting the pure neutron matter EoS with high accuracy $(n_n = n, n_p = 0, \beta = 1)$:

$$\mathcal{E}_n(n) = \frac{3\hbar^2(3\pi^2)^{2/3}}{10m_n}n^{5/3} + \mathcal{E}_{\rm int} \tag{3.12a}$$

$$\mathcal{E}_{\rm int} = (a_n n^{5/3} + b_n n^2 + c_n n^{7/3}). \tag{3.12b}$$

The coefficients a_n, b_n, c_n are fixed by fitting the neutron matter EoS as calculated with QMC including up to next-to-next-to-next-to leading order (N^{3}LO) two-body and up to next-to-next-to leading order (N^{2}LO) three-body interactions from chiral perturbation theory [83].

$$a_n = a_0 + a_1 + a_2 = -32.6 \text{ MeV fm}^2 \tag{3.13a}$$

$$b_n = b_0 + b_1 + b_2 = 115.4 \text{ MeV fm}^3 \tag{3.13b}$$

$$c_n = c_0 + c_1 + c_2 = 109.1 \text{ MeV fm}^4 \tag{3.13c}$$

As seen from Fig. 3.2, all three terms (but no more) are needed in Eq. (3.12b) for an accurate reproduction of the neutron EoS. At this time, we do not have an equally accurate QMC calculation of nuclear matter with varying isospin composition, so we must rely instead on a phenomenological approach. Our main assumption is that we can describe the isoscalar $j = 0, \beta^0$, isovector $j = 1, \beta^2$ and the quartic $j = 2, \beta^4$ parts using the same three powers of Fermi momenta Eq. (3.12b) and Eq. (3.13) as required to fit the EoS of the pure neutron matter. The isoscalar part describes the symmetric nuclear matter $n_n = n_p = n/2$:

$$\mathcal{E}_{\text{sym}}(n) = \frac{3\hbar^2(3\pi^2/2)^{2/3}}{10m} n^{5/3} + a_0 n^{5/3} + b_0 n^2 + c_0 n^{7/3} \tag{3.14}$$

with three parameters a_0, b_0, c_0 which can be uniquely determined by three quantities:

(1) The saturation density n_0

$$\frac{\partial}{\partial n}\left(\frac{\mathcal{E}_{\text{sym}}}{n}\right)\bigg|_{n=n_0} = 0. \tag{3.15}$$

A typical value of n_0 can be deduced from the LDM $n_0 = \frac{3}{4\pi r_0^3} \approx 0.16 \text{ fm}^{-3}$.

(2) The equilibrium energy density in (symmetric) nuclear matter ϵ_0

$$\varepsilon_0 = \mathcal{E}_{\text{sym}}(n_0)/n_0. \tag{3.16}$$

A typical value of ϵ_0 can be deduced from the coefficient of the volume term in BW formula $\epsilon_0 \sim -a_V \approx -16$ MeV.

(3) The incompressibility K_0

$$K_0 = \frac{\partial^2}{\partial k_F^2}\left(\frac{\mathcal{E}_{\text{sym}}}{n}\right)\bigg|_{n=n_0}, \quad k_F = (3\pi^2 n/2)^{1/3}. \tag{3.17}$$

A typical value of K_0 is around 230 MeV.

One can relate a_0, b_0, c_0 with n_0, ε_0, K_0 via the following equations

$$0 = +\frac{3}{5} + \tilde{a}_0 + \frac{3}{2}\tilde{b}_0 + 2\tilde{c}_0, \tag{3.18a}$$

$$\frac{\varepsilon_0}{\varepsilon_F} = +\frac{3}{5} + \tilde{a}_0 + \tilde{b}_0 + \tilde{c}_0, \tag{3.18b}$$

$$\frac{K_0}{\varepsilon_F} = -\frac{6}{5} - 2\tilde{a}_0 + 4\tilde{c}_0, \tag{3.18c}$$

where $\varepsilon_F = \frac{\hbar^2}{2m}(3\pi^2 n_0/2)^{2/3}$ is the Fermi energy and $\tilde{a}_j, \tilde{b}_j, \tilde{c}_j$ are defined as

$$\tilde{a}_j = \frac{a_j n_0^{2/3}}{\varepsilon_F},\ \tilde{b}_j = \frac{b_j n_0}{\varepsilon_F},\ \tilde{c}_j = \frac{c_j n_0^{4/3}}{\varepsilon_F}. \tag{3.19}$$

In a global mass fit including a_0, b_0, c_0, we find that a_0 is unconstrained at the level of changing the energy rms by $\delta\chi_E < 0.1$ MeV and thus set 0. The relation Eq. (3.18a) is then reduced to $\frac{3}{5} + \frac{3}{2}\tilde{b}_0 + 2\tilde{c}_0 = 0$ and used as a constraint between b_0 and c_0 when the saturation density n_0 is fixed in our fit (See discussions in section 3.3).

The isovector ($j = 1$) and quartic ($j = 2$) terms describe the symmetry parameters in the nuclear matter, e.g. the symmetry energy S

$$\begin{aligned} S &= \frac{\mathcal{E}(n_0, 0) - \mathcal{E}(n_0/2, n_0/2)}{n_0} \\ &= \frac{3}{5}(2^{2/3} - 1)\varepsilon_F + (a_1 + a_2)n_0^{2/3} + (b_1 + b_2)n_0 + (c_1 + c_2)n_0^{4/3} \end{aligned} \tag{3.20}$$

and the slope of the symmetry energy L

$$\begin{aligned} L &= 3n\frac{d}{dn}\left[\frac{\mathcal{E}(n, 0)}{n}\right]\Bigg|_{n_0} = 3n_0\varepsilon_n'(n_0) \\ &= \frac{6}{5}\frac{\hbar^2}{2m}(3\pi^2 n_0)^{2/3} + 2a_n n_0^{2/3} + 3b_n n_0 + 4c_n n_0^{4/3}. \end{aligned} \tag{3.21}$$

The QMC neutron EoS alone fixes value of $L \approx 30$ MeV. The typical value of S deduced from the LDM is $S \sim a_A \approx 30$ MeV in Eq. (3.2).

The emergence of the quartic term ($j = 2$) is necessary. In our global mass fit for 2375 atomic nuclei $A \geq 16$ in AME2012 dataset [81, 82], if the quartic terms are missing, the neutron matter EoS will not be reproduced (see discussions in section 3.5.3). We found

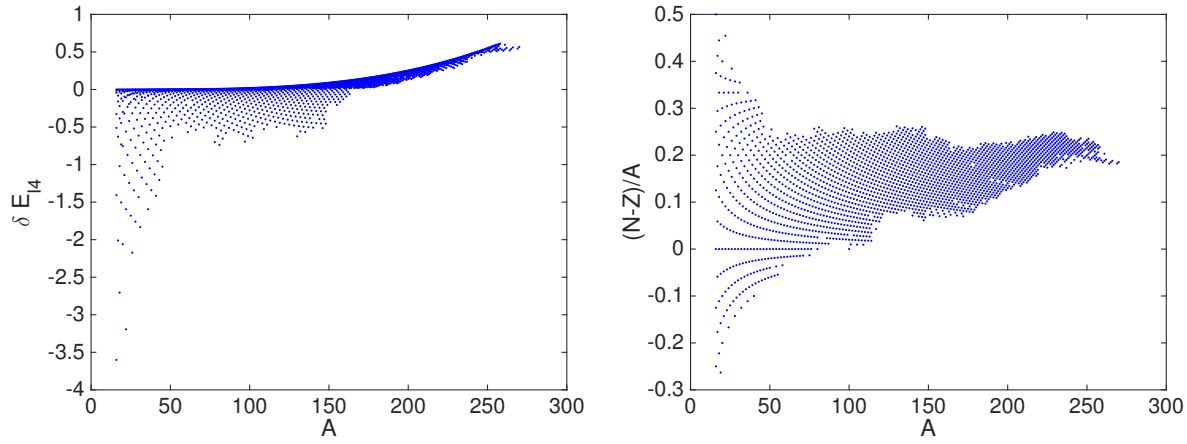

(a) (b)

Figure 3.3: **(a)** The contribution to the ground-state energies of the $j = 2$ terms in Eq. (3.10) for the 2375 nuclei ($A \geq 16$) in AME 2012 dataset [81, 82]. **(b)** The mass asymmetry parameter $(N - Z)/A$ for the same set of nuclei in **(a)**.

that the contribution of the quartic term in the ground state energy of nuclei is very small. Fig. 3.3a shows the contribution to the ground state energy of the quartic terms δE_{I4} calculated perturbatively in a certain parameter set [80] where the coefficients of quartic terms are 0. Except for some light nuclei, $\delta E_{I4} < 0.5$ MeV for most nuclei. The reason is that δE_{I4} is proportional to β^4, where the mass asymmetry factor $\beta \sim (N - Z)/A$. As shown in Fig. 3.3b, for most nuclei, $\beta \leq 1/4$ thus $\beta^4 \leq 1/256 \sim 10^{-3}$, which results in the small values of δE_{I4}. This fact gives us an important message: the neutron matter EoS is weakly constrained by the fit on finite nuclei, and one can construct a NEDF that reproduces the neutron matter EoS without any substantial influence on the global mass fit. Therefore, in our fitting procedure, the value of a_2 are determined from the values of a_n via $a_2 = a_n - a_0 - a_1$ and the same for b_2 and c_2.

Among the coefficients of the isovector terms ($j = 1$), the combination of $a_1 - b_1 n_0^{1/3}$ is found to be unconstrained at the level of changing the energy rms by $\delta\chi_E < 0.1$ MeV

and thus set 0. The other c_1 also has minor influence on the mass fit, but it can be used to tune the isovector symmetry properties, like the neutron skin thickness, together with $a_1 - b_1 n_0^{1/3}$, as discussed in section 3.5.3. Therefore we also include c_1 as a fitting parameter in the optimization of SeaLL1.

3.2.4 Gradient term

To describe the surface tension of the nucleus, we include a gradient term of the following form, similar to terms considered in the Skyrme NEDF [84], containing one phenomenological parameter η_s

$$\mathcal{E}_{\text{grad}} = \eta_s \sum_{q=n,p} \frac{\hbar^2}{2m} |\vec{\nabla} n_q|^2. \tag{3.22}$$

3.2.5 Spin-orbit coupling

Related to the gradient term is the spin-orbit coupling, which we include in the same form as in the Skyrme NEDF [84] with one parameter W_0:

$$\mathcal{E}_{\text{so}} = W_0 \vec{J} \cdot \vec{\nabla} n. \tag{3.23}$$

where $\vec{J} = \vec{J}_n + \vec{J}_p$ is the total spin current. Following Fayans [85], we only include the isoscalar portion here as the isovector contribution is small. One can also include the isovector terms

$$\mathcal{E}_{\text{so},1} = W_1 \vec{J}_1 \cdot \nabla n_1, \quad \vec{J}_1 = \vec{J}_n - \vec{J}_p, \quad n_1 = n_n - n_p \tag{3.24}$$

into the optimization to obtain a better agreement on the nuclear shell structure between the experimental and theoretical results, as discussed in section 3.5.4.

3.2.6 Pairing interaction

The pairing energy density depends on the anomalous density

$$\mathcal{E}_{\text{pair}} = \sum_{q=n,p} g_{\text{eff}}(\vec{r}) |\nu_q(\vec{r})|^2 \tag{3.25}$$

and the effective pairing coupling strength $g_{\rm eff}(\vec{r})$ is obtained via a renormalization [49, 50, 71] of the bare pairing strength, which may depend on neutron and proton densities.

3.3 Optimization

The full form of the functional SeaLL1 is

$$\mathcal{E}[n_n,n_p] = \overbrace{\frac{\hbar^2}{2m}(\tau_n+\tau_p)}^{\text{kinetic}} + \overbrace{\sum_{j=0}^{2}\left(a_j n^{5/3}+b_j n^2+c_j n^{7/3}\right)\beta^{2j}}^{\text{homogeneous}} + \overbrace{\eta_s\sum_{q=n,p}\frac{\hbar^2}{2m}|\vec{\nabla}n_q|^2}^{\text{gradient}}$$
$$+\underbrace{W_0\vec{J}\cdot\vec{\nabla}n}_{\text{spin-orbit}} + \underbrace{\sum_{q=n,p} g_{\rm eff}(\vec{r})|\nu_q(\vec{r})|^2}_{\text{pairing}} + \underbrace{\frac{e^2}{2}\int d^3\vec{r}'\frac{n_p(\vec{r})n_p(\vec{r}')}{|\vec{r}-\vec{r}'|} - \frac{e^2\pi}{4}\left(\frac{3n_p(\vec{r})}{\pi}\right)^{4/3}}_{\text{Coulomb}}, \tag{3.26}$$

which can be specified by seven parameters: b_0, c_0, characterizing isoscalar nuclear properties; b_1, c_1, defining the isovector nuclear properties; η_s, defining the surface tension; W_0, the strength of the isoscalar spin-orbit interaction; and the bare (unrenormalized) pairing coupling constant g_0 . In our fitting procedure, we keep g_0 fixed and add constraint between b_0 and c_0 by a fixed saturation density n_0:

$$\frac{3}{5}\frac{\hbar^2}{2m}(\frac{3\pi^2}{2})^{2/3} + \frac{3}{2}b_0 n_0^{1/3} + 2c_0 n_0^{2/3} = 0, \quad a_0 = 0. \tag{3.27}$$

Therefore in practice, for a given n_0, five parameters are included as the fitting parameters, which are obtained by minimizing the residuals

$$\chi_E^2 = \sum \frac{|E_{N,Z} - E(N,Z)|^2}{N_E}. \tag{3.28}$$

performed on $N_E = 196$ spherical even-even nuclei with $A \geq 16$ measured (not extrapolated) from AME 2012 dataset [81, 82]. To save the computational time, the ground state energies of spherical nuclei are solved by SLDA (formally self-consistent HFB) calculations using the modified HFBRAD code [86] in spherical coordinate.

In our earlier fits [80] we found that if there is no constraint in Eq. (3.27) for b_0 and c_0 one will obtain quite a low saturation density $n_0 \approx 0.14\,\mathrm{fm}^{-3}$, and a poorer fit to both

	SeaLL1	*hydro*	Comments
n_0	**0.154**	*0.154*	Adjusted (see Fig. 3.4a)
a_0	**0**	*same*	Insignificant
b_0	**−684.5(10)**	*−685.6(2)*	
c_0	**827.26**	*828.76*	$2c_0 n_0^{\frac{2}{3}} = -\frac{3\hbar^2}{10m}\left(\frac{3\pi^2}{2}\right)^{\frac{2}{3}} - \frac{3}{2}b_0 n_0^{\frac{1}{3}}$
a_1	**64.3**	*50.9*	$a_1 = n_0^{1/3} b_1$
b_1	**119.9(61)**	*94.9(14)*	
c_1	**−256(25)**	*−160.0*	Fixed in orbital-free theory
a_2	**−96.8**	*−83.5*	$a_2 = a_n - a_0 - a_1$
b_2	**449.2**	*475.2*	$b_2 = b_n - b_0 - b_1$
c_2	**−461.7**	*559.6*	$c_2 = c_n - c_0 - c_1$
a_n	**−32.6**	*same*	from neutron matter EoS (3.12b)
b_n	**−115.4**	*same*	from neutron matter EoS (3.12b)
c_n	**109.1**	*same*	from neutron matter EoS (3.12b)
η_s	**3.93(15)**	*3.370(50)*	
W_0	**73.5(52)**	*0.0*	Fixed in orbital-free theory
g_0	**−200**	*N/A*	g_0 fit in Ref. [50]
κ	**N/A**	*0.2*	Semi-classical (see section 3.4)
χ_E	**1.74**	*3.04*	606 even-even nuclei
		2.86	2375 nuclei
χ_r	**0.034**	*0.038*	345 charge radii
		0.041	883 charge radii

Table 3.1: Best fit parameters for the SeaLL1 functional (in bold) and the orbital-free approximation (next column in italic when different). The errors quoted for the fit parameters should be interpreted as estimating by how much this parameter can be independently changed while refitting the other and incurring a cost of at most $\delta\chi_E < 0.1\,\mathrm{MeV}$.

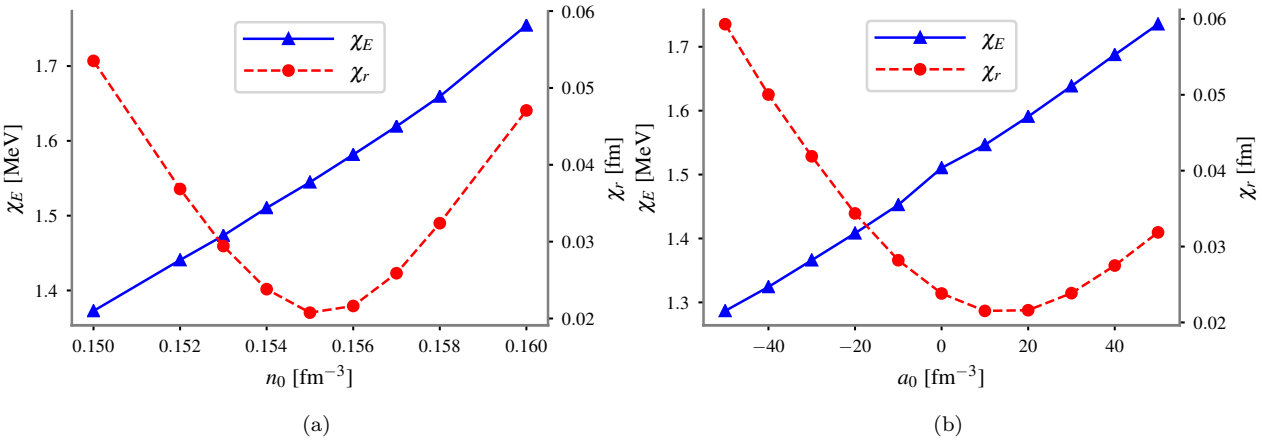

Figure 3.4: **(a)** Saturation density n_0 dependence of the energy residual χ_E and charge radii residual χ_r of the SeaLL1 functional. After holding n_0 fixed (through the parameter c_0), the remaining five shaded parameters in Table 3.1 were fit by minimizing only $\chi_E^2 = \sum|E_{N,Z} - E(N,Z)|^2/N_E$ over the $N_E = 196$ spherical even-even nuclei with $A \geq 16$ measured (not extrapolated) from [81, 82]. The value $n_0 = 0.154$ fm^{-3} fixed in the SeaLL1 functional represents a compromise between these residuals here both χ_E and χ_r increase by about 10%. **(b)** The changes in χ_E and χ_r for the $N_E = 196$ even-even spherical nuclei with $A \geq 16$, similarly to Fig. 3.4a as a function of the fixed parameter a_0, while the rest of the seven parameters of SeaLL1 specified in Table 3.1 are optimized.

charge radii and density profiles. To explore the influence of saturation density n_0 on the quality of the fit, we performed mass-only fits for the remaining five parameters with various saturation densities n_0 ranging from $0.15\,\mathrm{fm}^{-3}$ to $0.16\,\mathrm{fm}^{-3}$. For each fit, we also calculate the rms radii residuals $\chi_r^2 = \sum|\delta r|^2/N_r$ for the $N_r = 123$ corresponding nuclei in [87]. These results are shown in Fig. 3.4a, which demonstrates that the charge radii strongly prefer $n_0 \approx 0.155\,\mathrm{fm}^{-3}$ in contrast to the rather weak lower bias from the mass fits. To incorporate this preference in our fits, we fix the saturation density $n_0 = 0.154\,\mathrm{fm}^{-3}$ by adjusting c_0 using the Eq. (3.27). This represents a compromise between the two biases where both χ_E and χ_r increase by about 10%. With this fixed value of n_0, we fit the remaining five parameters of the SeaLL1 functional by minimizing only χ_E over the $N_E = 196$ spherical even-even nuclei as summarized in Table 3.1.

While we have chosen to keep the value of the parameter $a_0 = 0$, its value can be varied without affecting significantly the quality of the overall mass and charge radii fit, see Fig. 3.4b. By changing the adopted value $a_0 = \pm 20\,\mathrm{fm}^{-3}$ and keeping ε_0 and the saturation density fixed one can change the incompressibility by $\delta K_0 = \pm 2\delta\tilde{a}_0\varepsilon_F = \pm 2\delta a_0 n_0^{2/3} \approx \pm 23\,\mathrm{MeV}$.

3.4 Orbital-free functional

Besides the orbital-based SeaLL1 functional presented above, we also formulate an orbital-free version of SeaLL1 for saving the computational cost. The main challenge in formulating an orbital-free theory is to express terms with the auxiliary densities $\tau_{n,p}$, $\vec{J}_{n,p}$, and $\vec{j}_{n,p}$ by an appropriate functional of the number densities $n_{n,p}$, as discussed in section 2.1. We suggest using the following combination for the kinetic and spin-orbit contributions in an orbital-free theory:

$$\mathcal{E}_{\mathrm{kin}}[n_n, n_p] + \mathcal{E}_{\mathrm{SO}}[n_n, n_p] = \frac{\hbar^2}{2m} \sum_{q=n,p} \tau_{TF}[n_q] F(X_q) - \frac{W_0^2}{2} \frac{2m}{\hbar^2} n |\vec{\nabla} n|^2. \tag{3.29a}$$

where

$$F(X) = \frac{1 + (1+\kappa)X + 9\kappa X^2}{1 + \kappa X}, \qquad X = \frac{\tau_2[n]}{\tau_{TF}[n]}, \tag{3.29b}$$

$$\tau_{TF}[n] = \tfrac{3}{5}(3\pi^2)^{2/3} n^{5/3}, \qquad \tau_2[n] = \frac{1}{9} |\vec{\nabla}\sqrt{n}|^2. \tag{3.29c}$$

The ratio X characterizes the size of the gradients in the system in terms of the leading τ_{TF} and subleading τ_2 terms of the semiclassical expansion [88, 67, 69] of the kinetic density τ. The Padé approximation $F(X)$ suggested by DePristo and Kress [89] makes an interpolation between the semi-classical limit $X \ll 1$ valid in the interior region of nuclei, and the approximation $\tau \approx \tau_{TF} + |\vec{\nabla}\sqrt{n}|^2$ introduced by Ref. [90] which correctly reproduces the asymptotic fall off of the density when $X \gg 1$. When the spin-orbit interaction is missing, $\tau_{TF}[n_q]F(X_q)$ gives a semi-classical approximation of the kinetic density τ. This approximation requires a single additional parameter κ. The value of κ can be chosen approximately by comparisons between τ and $\tau_{TF}[n_q]F(X_q)$, and between their resulting kinetic energies E_{kin}, for the same

set of single-particle wavefunctions. We found $\kappa \approx 0.2$ will give a reasonable semi-classical approximation for τ and E_{kin}.

The semi-classical spin-orbit contribution is suggested by Brack *et al.* [68], which brings a parameter W_0 corresponding to the one in Eq. (3.23). Like the orbital-based approach, this parameter is also subdominant for mass fits and its contribution can be incorporated in the gradient the global mass fit. Furthermore, due to the missing of the shell structure in the orbital-free theory, this parameter is even more unconstrained.

The orbital-free formulation of the NEDF requires the additional parameter κ to approximate the gradient corrections. As discussed above we choose $\kappa = 0.2$. Following SeaLL1, we fix the saturation density $n_0 = 0.154\,\text{fm}^{-3}$, and fit the 3 parameters b_0, b_1 and η_s shaded in Table 3.1. The spin-orbit contribution is neglected as it can be absorbed in the gradient term. The unconstrained parameter c_1 is also fixed to obtain reasonable neutron skin thickness for ^{208}Pb and ^{48}Ca. The parameter values are determined by performing the same least squares minimization of the binding energy residuals as SeaLL1, but over all $N_E = 2375$ nuclei (including the deformed even-even, odd-even, and odd-odd ones) with $A \geq 16$ measured from [81, 82].

The parameter values and rms residuals of orbital-free theory are also summarized in Table 3.1. As expected, the rms residuals $\chi_E = 2.86\,\text{MeV}$ is larger than the χ_E of SeaLL1 due to the lack of shell corrections in the orbital-free theory, but are comparable with results from the liquid-drop formula.

3.5 Physical Properties

3.5.1 Global mass table

Since our orbital-based NEDF was fit on spherical even-even nuclei only, we validate its predictive power by performing fully microscopic calculation of the nuclear binding energies of 606 even-even nuclei with $A \geq 16$ in Refs. [81, 82]. We used an extension of the axial DFT solver HFBTHO code [91, 92, 93] that includes the SeaLL1 and the regularization of the

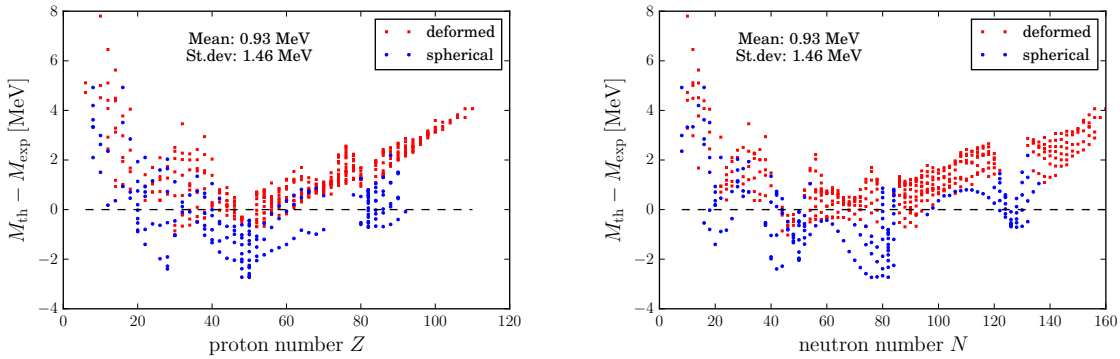

Figure 3.5: Mass residuals between SeaLL1 andmeasured masses for 606 even-even nuclei, of which 410 are deformed nuclei and 196 are spherical nuclei, plotted with red squares and blue bullets respectively as a function of proton number Z (left) and neutron number N (right).

pairing channel. Calculations were performed in a deformed basis of 20 harmonic oscillator shells. In the pairing channel, a cutoff of 100 MeV was adopted in accordance with Ref. [49].

Fig. 3.5 shows the residuals of the nuclear masses calculated with SeaLL1 with respect to the experimental values of these even-even nuclei. The r.m.s. of the residuals is $\chi_E = 1.74$ MeV. Besides the larger residuals in light nuclei, we observe the typical arc-like features common to many NEDF calculations, both for isotonic and isotopic chains. The poor performance of SeaLL1 in light nuclei is likely related to the c.m. corrections (not accounted for here) and is also observed in the UNEDF functionals [94, 95, 96]. Since the c.m. correction is larger for light nuclei, our parameter fit limited to spherical nuclei leads to an underestimate of the masses of heavier spherical nuclei; see Fig. 3.5.

Overall the masses have a bias $\epsilon_E = \langle \delta E \rangle = 0.93$ MeV and a standard deviation $\sigma_E = 1.46$ MeV. This bias enters the rms error $\chi_E^2 = \sigma_E^2 + \epsilon_E^2$ which leads to a value of $\chi_E = 1.74$ MeV. This σ_E is an upper estimate of the rms energy χ_E we expect if the SeaLL1 parameters would have been instead fitted to all even-even nuclei.

The residuals for the two-nucleon separation energies for the same set of even-even nuclei are shown in Fig. 3.6, and they are naturally less affected by the errors induced by errors on

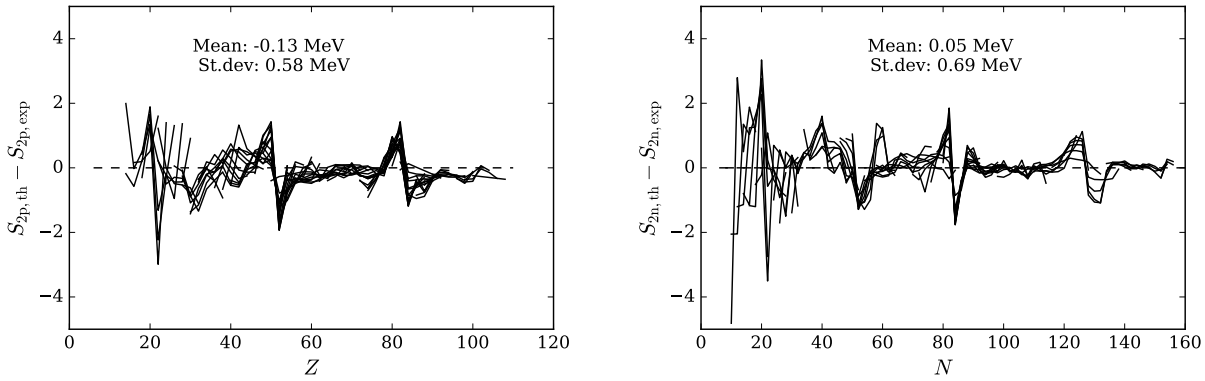

Figure 3.6: The residual of the two-nucleon separation energies between SeaLL1 and experiment for 606 even-even nuclei: $S_{2p}(Z)$ for constant N (left) and $S_{2n}(N)$ for constant Z (right) chains connected by lines.

binding energies.

3.5.2 Charge radii and density distributions

Using the parameters determined from the mass fits, SeaLL1 also models the neutron and proton densities in the nuclei, allowing us to extract the charge densities for these nuclei using Eq. Eq. (3.9). As a good benchmark, in Fig. 3.7 we compare the proton and charge densities of ^{48}Ca and ^{208}Pb calculated with SeaLL1 with the charge densities extracted from the electron scattering experiment [97]. The calculated ^{208}Pb has a slightly larger radius and slightly smaller diffuseness compared to those extracted from data, which is consistent with the charge radii comparison between SeaLL1 and experiment in Fig. 3.8.

The residuals of radii for 345 matching even-even nuclei in Ref. [87] are also calculated, with a bias $\epsilon_r = 0.022$ fm and a standard deviation $\sigma_r = 0.025$ fm, which gives a rms residual of $\chi_r = 0.034$ fm, as shown in Fig. 3.8.

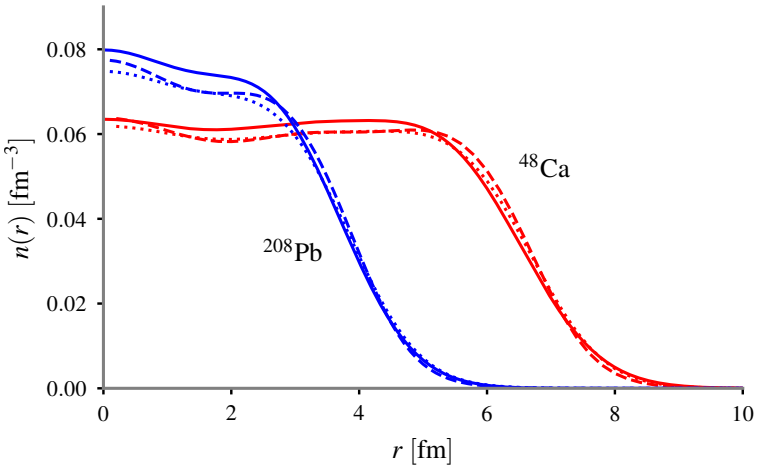

Figure 3.7: (Color online) The calculated proton $n_p(r)$ (dashed) and charge $n_{\rm ch}(r)$ (dotted) densities for ^{48}Ca (red) and ^{208}Pb (blue), calculated with SeaLL1 compared to charge densities (solid) extracted from electron scattering experiments [97].

3.5.3 Saturation and symmetry properties, neutron matter

The isoscalar parameters with $j = 0$ and quadratic isovector parameters with $j = 1$ (β^2) may be directly related to the saturation and symmetry properties respectively by expanding the energy per nucleon of homogeneous nuclear matter Eq. (3.10) about the symmetric saturation point $n_n = n_p = n_0/2$:

$$\frac{\mathcal{E}(n_n, n_p)}{n} = \epsilon_0(n) + \epsilon_2(n)\beta^2 + \epsilon_4(n)\beta^4 + \mathcal{O}(()\beta^6). \tag{3.30}$$

The saturation density n_0, energy per nucleon ε_0, and incompressibility K_0 are defined in Eq. (3.15), Eq. (3.16) and Eq. (3.17), and depend only on the $j = 0$ isoscalar parameters a_0, b_0, and c_0 by Eq. (3.18). Expanding about n_0 in $\delta = (n - n_0)/3n_0$ and in powers of $\beta = (n_n - n_p)/n$, one can define various "local" contributions to the symmetry energy $S_{2,4}$,

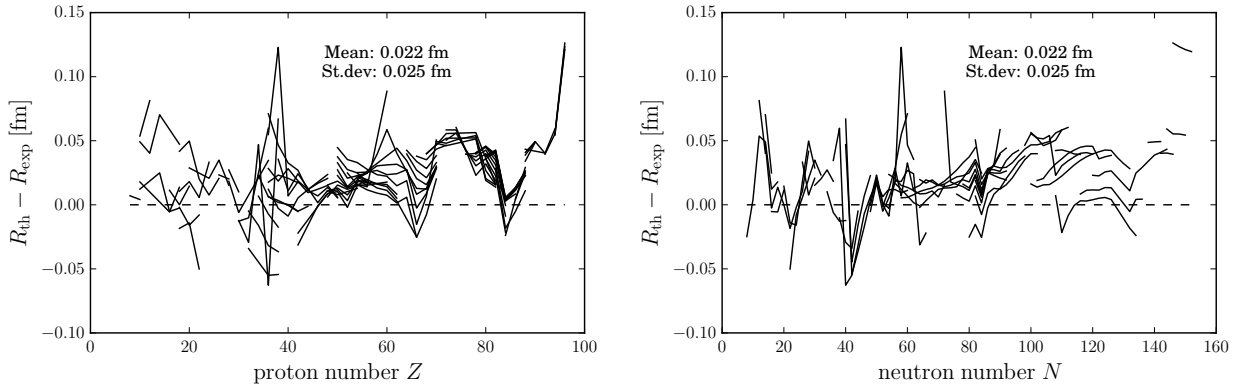

Figure 3.8: Radii residuals between SeaLL1 and experiment for 345 even-even nuclei. Isotonic (left) and isotopic (right) chains are connected by lines.

its density dependent slope $L_{2,4}$, etc.

$$\begin{aligned}
\epsilon_0(n) &= \tfrac{6}{5}\varepsilon_F \quad + a_0 n^{2/3} + b_0 n \quad + c_0 n^{4/3} \\
&= \varepsilon_0 \qquad\qquad + \tfrac{1}{2}K_0\delta^2 + \mathcal{O}(()\delta^3), \\
\epsilon_2(n) &= -\tfrac{4}{15}\varepsilon_F + a_1 n^{2/3} + b_1 n \quad + c_1 n^{4/3} \\
&= S_2 \quad + L_2\delta \quad + \tfrac{1}{2}K_2\delta^2 + \mathcal{O}(()\delta^3), \\
\epsilon_4(n) &= S_4 \quad + L_4\delta \quad + \tfrac{1}{2}K_4\delta^2 + \mathcal{O}(()\delta^3).
\end{aligned} \tag{3.31}$$

Since we include also quartic terms β^4, we must differentiate between these local symmetry parameters S_2, L_2, etc. and the full symmetry parameters defined as the difference between symmetric matter and pure neutron matter: S and L in Eq. (3.20) and Eq. (3.21). Using $a_1 = b_1 n_0^{1/3}$ (see Table 3.1), we obtain the values for S_2 and L_2 given by relations

$$S_2 = \frac{1}{3}\varepsilon_F + 2a_1 n_0^{2/3} + c_1 n_0^{4/3}, \tag{3.32a}$$

$$L_2 = \frac{2}{3}\varepsilon_F + 5a_1 n_0^{2/3} + 4c_1 n_0^{4/3}. \tag{3.32b}$$

As shown in Table 3.2, the binding energy of nuclear matter and the symmetry energy predicted by SeaLL1 fit agrees well with the value obtained with the mass formula Eq. (3.2).

							Neutron skin	
ρ_0	$-\epsilon_0$	K_0	S	S_2	L	L_2	^{208}Pb	^{48}Ca
[fm^{-3}]							[fm]	[fm]
0.154	15.6	230	31.7	27.7	32.4	32	0.131	0.159

Table 3.2: Saturation, symmetry, and neutron skin properties for SeaLL1. All values in MeV unless otherwise specified.

As mentioned in section 3.2.3, it is shown that the combination of $a_1 = b_1 n_0^{1/3}$ and c_1 are unconstrained by the global mass fit, but the related quantities S_2 and L_2 control the neutron skin thickness. We compute the neutron skin thickness of ^{48}Ca and ^{208}Pb, for which precision measurements CREX and PREX are underway; see Ref. [98] for details. The ^{208}Pb neutron skin is consistent with the value $0.156^{+0.025}_{-0.021}$ fm of Ref. [99], and with the recent measurement of 0.15(3) fm [100].

The neutron matter EoS is also well reproduced in the SeaLL1 EDF. Fig. 3.9 shows the energy per nucleon for pure neutron matter and symmetric neutron matter calculated from SeaLL1 EDF compared with the Fayans [85] and BCMP EDFs [101, 102, 103]. The result obtained from the QMC calculation using chiral effective theory [83] is also shown, with two-body plus three-body interactions (2N+3N) as well as the two-body only interactions (2N).

3.5.4 Spherical shell structure

Shell structure is a fundamental property of atomic nuclei. In an independent-particle picture, the shell structure can be associated with the single-particle spectra of the mean-field potential. Reproducing the correct ordering and distribution of single-particle levels is essential for nuclear structure theories, and also important for the application of the NEDF in nuclear dynamics, such as nuclear fissions and collisions. Fig. 3.10 displays the single-particle

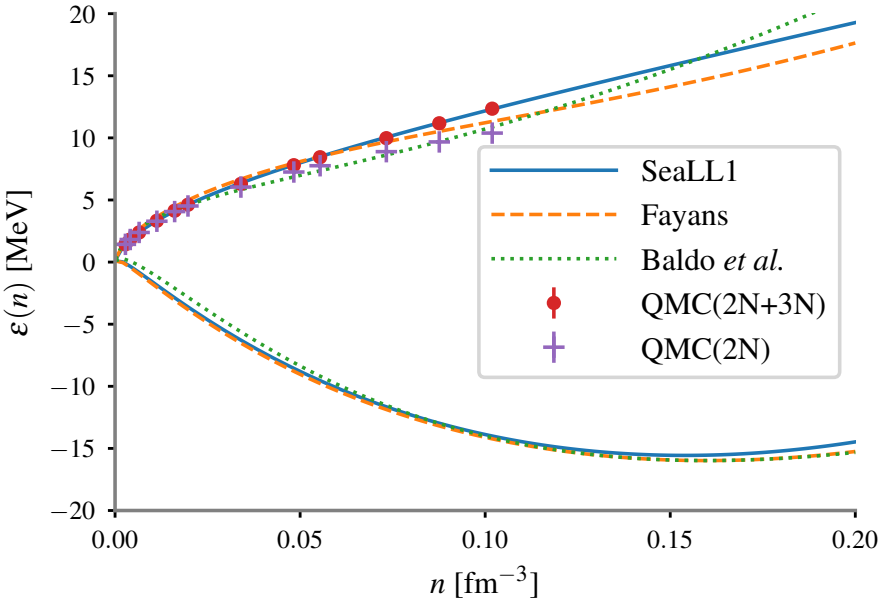

Figure 3.9: The energy per nucleon for pure neutron matter and symmetric neutron matter used in SeaLL1, compared to the corresponding energies used by [85] and [101, 102, 103]. For comparison we have shown with a dashed line the results of the quantum Monte Carlo (QMC) calculation of [83], with 2N and 3N interactions as well the result with the 2N interactions alone.

levels for neutrons and protons in ^{48}Ca and ^{208}Pb for the SeaLL1, UNEDF0, UNEDF1, and UNEDF2 NEDF. Single-particle energies were obtained by blocking calculations in the neighboring odd nuclei following the procedure outlined in Refs. [95, 96].

In ^{48}Ca, the rms deviations for the single-particle energies of UNEDF0, UNEDF1, UNEDF2, and SeaLL1 with the empirical values (Exp) [104] are 1.50, 1.71, 1.92, and 1.88 MeV and 1.22, 1.08, 1.22, and 1.17 MeV for neutrons and protons, respectively. In ^{208}Pb, these are 0.82, 0.61, 0.69, and 0.62 MeV and 0.77, 0.49, 0.50 and 0.54 MeV for neutrons and protons, respectively. Compared with the empirical values, the $N = 28$ and $Z = 20$ gaps in ^{48}Ca are clearly too small with SeaLL1. The single-particle proton levels in ^{208}Pb show that the $Z = 82$ gap is also smaller in SeaLL1. Such patterns are also observed in UNEDF2 functional which, however, included single-particle spin-orbit splittings in their fit [96]. This might point to the need to consider the contribution from the isovector spin-orbit contribu-

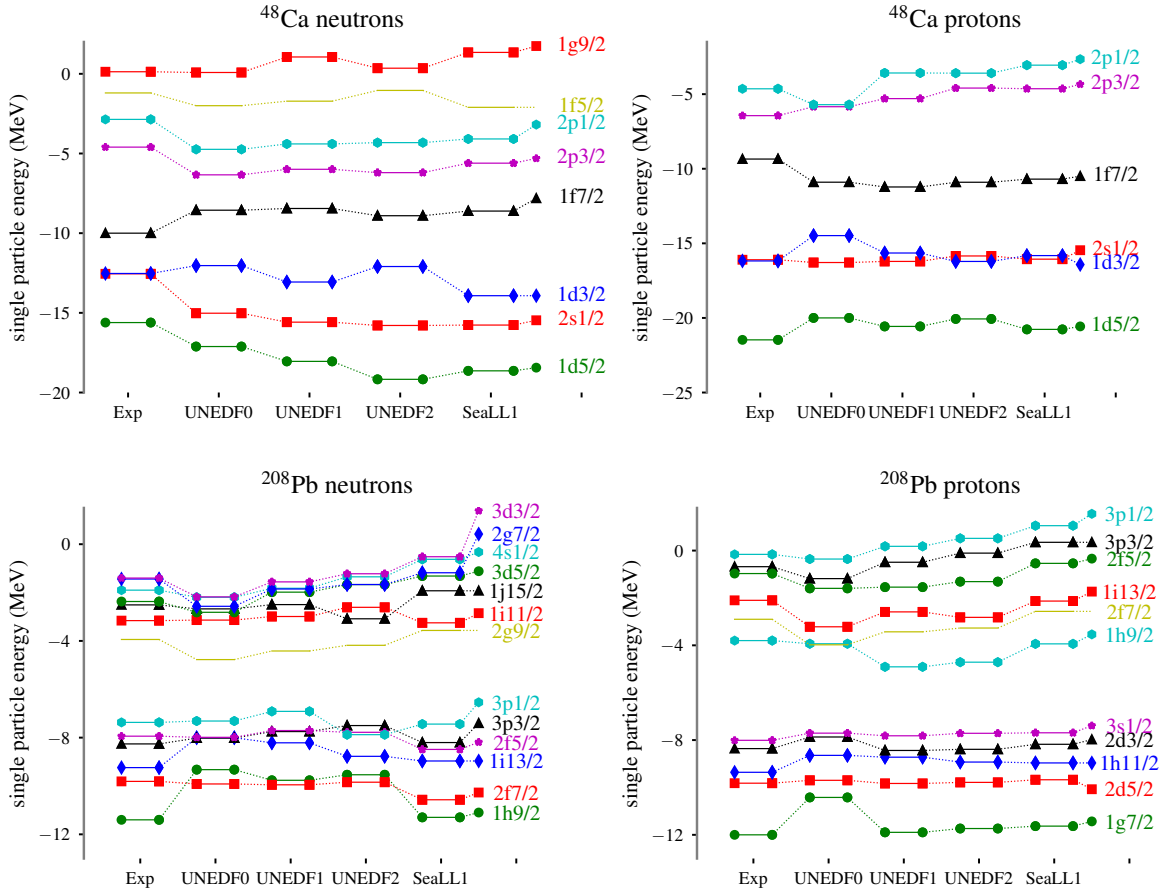

Figure 3.10: (Color online) Single particle energies in ^{48}Ca (upper panel) and ^{208}Pb (lower panel) for a variety of functionals UNEDF0-2 [94, 95, 96] and SeaLL1 (calculated using the HFBTHO DFT solver [91]).

tion in Eq. (3.24) proportional to W_1. Overall, however, the SeaLL1 single-particle spectra, as quantified in the corresponding rms, are of better quality than UNEDF2.

3.5.5 Fission pathway of ^{240}Pu

One of the important applications of nuclear DFT is the description of nuclear fission [22]. In this context, characteristics of fission pathways such as the excitation energy of fission isomers or the height of fission barriers are often used to gauge the predictive power of NEDFs. To this purpose, we computed the potential energy surface of ^{240}Pu with SeaLL1

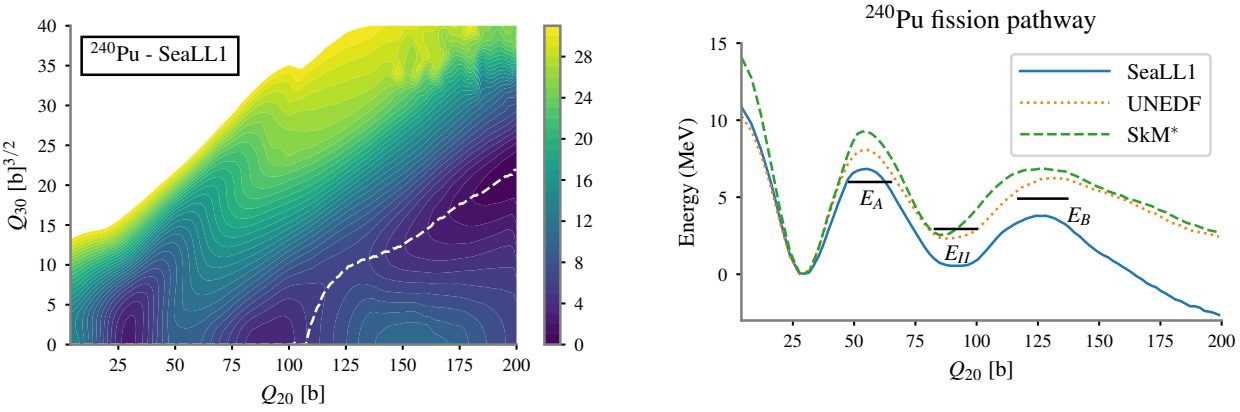

(a) (b)

Figure 3.11: **(a)**: Two-dimensional potential energy surface of ^{240}Pu with SeaLL1 for $0 \leq Q_{20} \leq 200$ b, $0 \leq Q_{30} \leq 40$ b$^{3/2}$. The least-energy fission path is marked as white dashed line. **(b)**: Fission pathway for ^{240}Pu along the mass quadrupole moment Q_{20} calculated using HFBTHO with SeaLL1, SkM*, and UNEDF1-HFB.

by performing constrained HFB calculations with constraints on the mass quadrupole Q_{20} and octupole moment Q_{30} in the region $0 \leq Q_{20} \leq 200\,\mathrm{b}, 0 \leq Q_{30} \leq 40\,\mathrm{b}^{3/2}$. The definitions and units of Q_{20} and Q_{30} are consistent with Ref. [105] and the characteristics of the harmonic oscillator (HO) basis used in the calculation are the same as in Ref. [106]. All calculations were performed with the HFBTHO DFT solver [91]. The results are shown in Fig. 3.11a.

From this two-dimensional potential energy surface, we extracted the least-energy trajectory starting at the ground state. Fig. 3.11b shows the potential energy curve of ^{240}Pu as a function of Q_{20} along this (asymmetric) fission pathway. To gain an idea of the quality of SeaLL1, we repeated the calculations with the SkM* [107], and UNEDF1-HFB [108] energy functionals, both of which were designed for fission studies.

Since all these calculations were done with the HFBTHO DFT solver, triaxiality is not included and the height of the first fission barrier is typically overestimated for all three functionals by about 2 MeV [106]. Compared with SkM* and UNEDF1-HFB, SeaLL1 underestimates the excitation energy of the fission isomer ($E_I = 0.54$ MeV compared with an

experimental value of 2.8 MeV) and the heights of both fission barriers ($E_A = 6.84\,\mathrm{MeV}$ vs. $6.05\,\mathrm{MeV}$, and $E_B = 4.20\,\mathrm{MeV}$ vs. $5.15\,\mathrm{MeV}$, respectively, for the inner and outer barriers) agree within $1\,\mathrm{MeV}$.

This result deserves a few comments. First, we note that both SkM* and UNEDF1 were constrained specifically on the height of the first fission barrier (SkM*) or excitation energy of the fission isomer (UNEDF1). By contrast, we did not include any specific information for nuclei at large deformation in the fit protocol of SeaLL1. It is, therefore very encouraging that, without any such constraint, the resulting NEDF is still in reasonable agreement with experimental results, especially the height of the two barriers. Our results are definitely better than predictions with, e.g., SLy4 [84], another popular NEDF without constraints on large deformations, which predicts the second fission barrier much higher than the first one [75]. Second, the error in fission barriers of NEDFs designed for fission can reach $2.5\,\mathrm{MeV}$, as can be seen in Ref. [96] where fission barriers and the energy of the second isomer in chains of Ra, Th, U, Pu, Cm, and Cf, are compared to the UNEDF1-2, Gogny D1S [109], and FRLDM [110] functionals. We also point to a recent study of the surface energy coefficient a_s (see Eq. (3.2)) for 76 parameterizations of the Skyrme NEDF [111] and the rather complex interplay between the roles of the shell-effects and of the surface energy on the values of the fission barriers in ^{240}Pu. The energy of the fission isomer and the height of the outer fission barrier, are shown to vary by several MeVs with respect to the ground state energy. Third, we should repeat here the usual warnings about taking at face value calculations of fission barrier heights: these quantities are not physical observables, but are extracted from data in a (very) model-dependent manner.

Ultimately, the predictive power of SeaLL1 (or any other NEDF for that matter) should be judged on their ability to reproduce fission half-lives, or fission fragment distributions. We will discuss in chapter 4 that, in the TDSLDA approach, the SeaLL1 NEDF provides a very accurate description of the features of the dynamics for the induced fission in ^{240}Pu, comparable to that of SkM*, whose fission properties are similar to UNEDF1-HFB.

Chapter 4

FISSION DYNAMICS

As discussed in chapter 1, fission dynamics is one of the most complicated problems in nuclear physics and still lacks a pure microscopic interpretation. The real-time method in the TDSLDA framework provides a powerful tool to study fission dynamics. As shown in the work [45], the saddle-to-scission process in the induced fission of ^{240}Pu was simulated in the TDSLDA framework and the resulting fission fragments (FFs) properties matched pretty well with the mean values of experimental observations. In this proof-of-concept study [45], the authors chose arbitrarily to use the SLy4 NEDF [84], which accurately describes a large body of nuclear observables throughout the nuclear mass table, even though this functional is not particularly popular among fission practitioners. Besides, no efforts were made in tuning various input parameters and their impacts on the resulting FF properties are not clear.

In this chapter [1], we adopt the SeaLL1 NEDF introduced in chapter 3 and the SkM* NEDF in the simulations. These two NEDFs demonstrate good deformation properties discussed in section 3.5.5. We also study the sensitivity of TDDFT trajectories with respect to their initial configurations. The role of pairing correlations in fission dynamics is also studied quantitatively. We have a comprehensive presentation on various FFs properties like mass split, total kinetic energy (TKE), temperature, shape, and neutron emission. Finally, we also discuss the adiabaticity of fission dynamics and show that the dynamics is a non-adiabatic, overdamped one.

---

[1] This chapter is based on the work by A. Bulgac, S. Jin, K. Roche, N. Schunck and I. Stetcu, *Fission Dynamics*, arXiv:1806.00694 [112] with minor modifications.

4.1 Simulation set-up

The initial states of TDSLDA equation Eq. (2.39) are prepared by direct diagonalizations of the self-consistent Hamiltonian in a 3D symmetry-unrestricted lattice (see appendix A for details). The self-consistent solutions are generated using the code HFBTHO [91] with appropriate constraints on the expectation value of the quadrupole, $\langle\hat{Q}_{20}\rangle$, and octupole, $\langle\hat{Q}_{30}\rangle$ moments defined in Eq. (2.57). HFBTHO calculations are performed in a stretched basis of $N_0 = 28$ shells with the deformation β and the oscillator frequency ω_0 set as in Ref. [106]. The matrix of the Bogoliubov transformation is then transformed in the coordinate space representation on a spatial lattice of size $N_xN_yN_z \times 4N_xN_yN_z$ according to

$$\begin{pmatrix} u_{k\sigma}(\vec{r}) \\ v_{k\sigma}(\vec{r}) \end{pmatrix} = \begin{pmatrix} \sum_n U_{nk}\psi_{n\sigma}(\vec{r}) \\ \sum_n V_{nk}\psi^*_{n\sigma}(\vec{r}) \end{pmatrix}, \tag{4.1}$$

where $\psi_{n\sigma}(\vec{r})$ are the harmonic oscillator basis spinors, see Refs. [93, 113]. The qpwfs are used to reconstruct the densities and the potentials which define the HFB hamiltonian in Eq. (2.24).

In our typical simulations, the size of the 3D box is $30\times30\times60$ fm^3 with a lattice constant $l = 1.25$ fm,which corresponds to a momentum cutoff $p_c = \hbar\pi/l \approx 500$ MeV/c in each spatial direction. We use the fast Fourier transform (FFT) to calculate the spatial derivatives, since it reduces the number of floating point operations significantly, while practically ensuring machine precision for derivatives. The number of coupled nonlinear time-dependent 3D partial differential equations (PDEs) solved increased significantly from $\approx$ 56,000 in Ref. [45] to $16 \times N_xN_yN_z$ = 442,368 PDEs. While evaluating the neutron emission rates, we have used in a couple of instances an even larger simulation box $30^2 \times 120$ fm^3, which amounted to evolving in time 884,736 PDEs.

4.2 Role of pairing correlations

The importance of pairing correlations in nuclear shape dynamics has been discussed in section 1.1. Without pairing the redistribution of s.p. levels of nucleons cannot be realized and

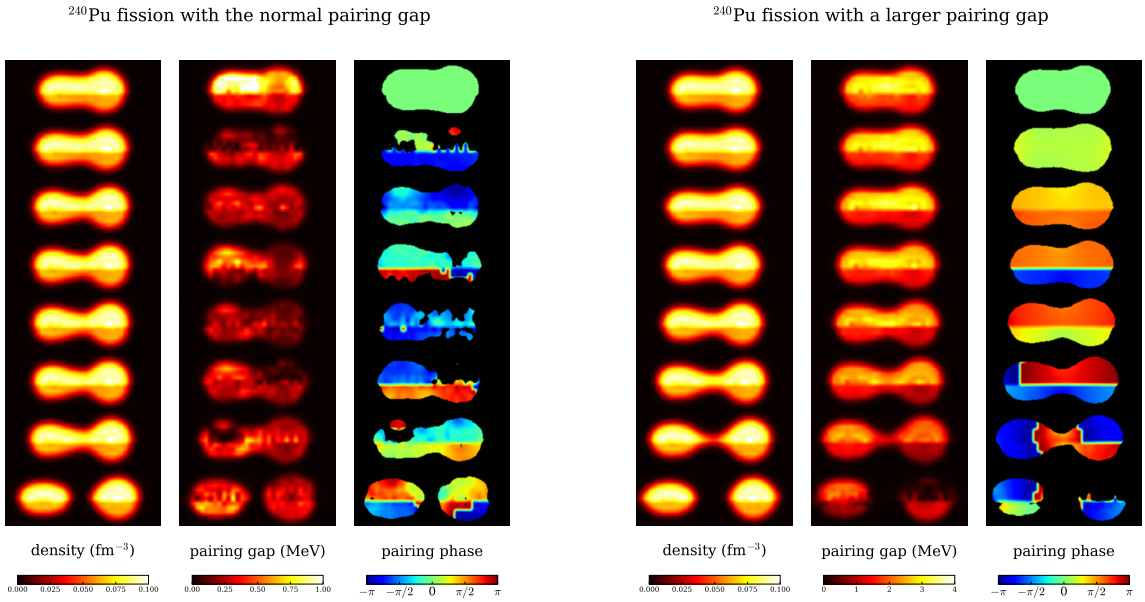

(a) (b)

Figure 4.1: The left three columns shows the induced fission of ^{240}Pu with normal pairing strength, which lasts up to 14,000 fm/c($\approx 47 \times 10^{-21}$ s) from saddle-to-scission. The columns show sequential frames of the density (1st column), the magnitude of the pairing field (2nd column), and the phase of the pairing field (3rd column). The upper/lower part of each frame shows the neutron/proton density, the magnitude of neutron/proton pairing fields, and of the phase of the pairing field respectively [45]. The right three columns shows the corresponding snapshots of the induced fission of ^{240}Pu with enhanced pairing strength, which lasts about 1,400 fm/c.

the fission will be hindered. To illustrate the crucial role played by the pairing correlations in fission dynamics quantitatively, we performed a TDSLDA simulation with an initial configuration identical to the S3 case of Ref. [45], but enforcing stronger pairing correlations by increasing the absolute value of bare coupling constant g_0. The corresponding average pairing gaps of neutrons and protons in the initial state increase from 0.73 and 0.33 MeV to 2.57 and 1.62 MeV. By increasing the strength of the pairing field, the fission dynamics proceeds approximately ten times faster. Fig. 4.1 shows the snapshots of the number density, magnitude of pairing field, and phase of pairing field for neutron and proton respectively in these two simulations. The left three columns show the induced fission of ^{240}Pu with realistic pairing strength, which lasts up to 14,000 fm/c from saddle-to-scission, while the right three columns show the dynamics with an enhanced pairing strength, which lasts only about 1,400 fm/c. In the case with normal pairing strength, the pairing field on the way from saddle-to-scission fluctuates noticeably in magnitude and phase. Therefore, strictly speaking the pairing field during its time evolution stops being a superfluid condensate of Cooper pairs, which otherwise would show a long-range-order. However, in the case with a larger pairing strength, the pairing field shows the expected characteristics of a slowly evolving superfluid condensate, the nuclear fluid behaving almost like a perfect or ideal fluid. This pattern was also observed in case of collision of two superfluid heavy-ions [114]. In the absence of pairing correlations the dynamics can come to a stop [41, 42, 43]. Even though realistic pairing correlations are rather weak they still provide enough "lubricant" for the saddle-to-scission evolution to take place.

4.3 Results

We have chosen an ensemble of initial conditions in the Q_{20}, Q_{30} collective coordinates, in total 56 different initial conditions, as shown in Fig. 4.2. One set of initial conditions (SeaLL1-1) corresponds to configurations of ^{240}Pu with mean excitation energies (variance) 7.9(1.7) MeV in the neighborhood of the outer saddle point, which can be reached in low energy neutron induced fission. The other set of initial conditions (SeaLL1-2) corresponds to exci-

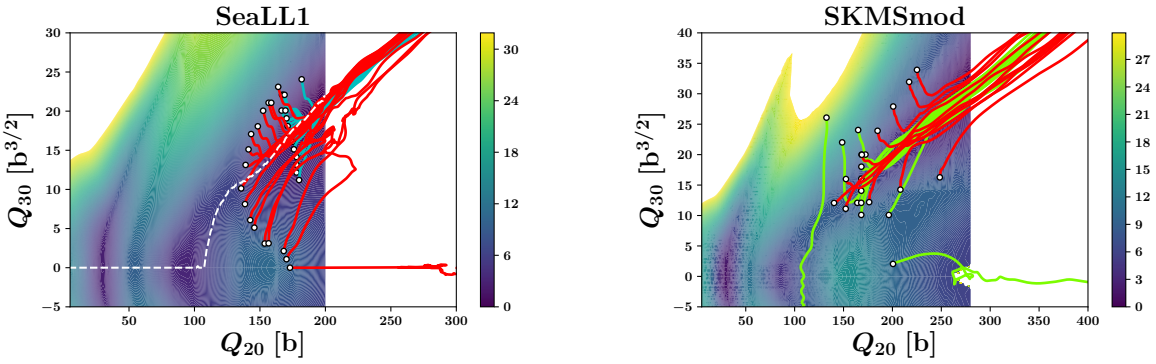

(a) (b)

Figure 4.2: Fission trajectories for SeaLL1 (a) and SkM* (b). The red (SeaLL1-1) and cyan (SeaLL1-2) lines in (a) correspond to initial configurations closer to and further from the outer fission barrier. The SeaLL1-1sy trajectory had a small initial left-right asymmetry. The green lines in (b) correspond to SKM*-1asy and and the red lines to the trajectories obtained with SkM*-asy2. The white dashed line shows the least-energy fission path.

tation energies (variance) 2.6(1.8) MeV, which can be reached either in spontaneous fission or with photo-excitation excitation of ^{240}Pu. The third set of initial conditions (SkM*-1) is similar to SeaLL1-1, with excitation energies (variance) 8.2(3.0) MeV, but with an increased pairing strength. The fourth set (SkM*-2) was characterized by realistic pairing strength. In the simulations with SLy4 NEDF [84] and SkM*, we have neglected the correction for the center-of-mass kinetic energy, namely we neglected the correction term $1/A$ in the s.p. kinetic energy $1 - 1/A$. We have checked that this term has a negligible influence on the profile of the potential energy surface. Without this correction term these NEDFs satisfy local Galilean invariance.

4.3.1 Fission fragments properties

The most surprising outcome of these simulations is that in all these sets of initial conditions, which correspond to vastly different initial values of Q_{20}, Q_{30}, we observed a very strong

focusing effect and the final states are remarkably similar, see Fig. 4.2. The heavy fragment has neutron and proton numbers between those of the double magic ^{132}Sn ($N = 82, Z = 50$) and of the octupole shaped ^{144}Ba, with $Z = 56$ and $N = 88$, and thus demonstrates a shape quite close to spherical. The lighter fragment has an elongated shape (see also Table 4.2). The Ref. [115] has recently shown that the octupole shell stabilization of nuclei close to ^{144}Ba with $Z = 56$ drive the fission dynamics towards proton numbers larger than 50, as we also appear to confirm. The neutron and proton numbers (and thus the mass) of the FFs match pretty well to the mean values of the experimental systematics, but show a very small dispersion, see Table 4.1.

The total kinetic energy (TKE) and total excitation energy (TXE) are also calculated. The TKE at a relatively large finite separation between the fragments (≈ 25 fm) and in the center-of-mass reference frame is evaluated with the formula

$$\mathrm{TKE} = \frac{1}{2} m A_{\mathrm{H}} \vec{v}_{\mathrm{H}}^2 + \frac{1}{2} m A_{\mathrm{L}} \vec{v}_{\mathrm{L}}^2 + E_{\mathrm{Coul}}, \tag{4.2a}$$

with the velocity of the fragment $f = H, L$ given by

$$\vec{v}_f = \frac{\hbar}{m A_f} \int_{V_f} d^3 r \vec{j}(\vec{r}), \quad A_f = \int_{V_f} d^3 r n(\vec{r}), \tag{4.2b}$$

where $\vec{j}(\vec{r})$ and $n(\vec{r})$ are the total current and number densities respectively defined in Eq. (2.37), and the integral is performed over the appropriate half-box V_f where each fragment is located. The Coulomb interaction energy (direct term only) is given by

$$E_{\mathrm{Coul}} = e^2 \int_{V_{\mathrm{H}}} d^3 r_1 \int_{V_{\mathrm{L}}} d^3 r_2 \frac{n_p(\vec{r}_1) n_p(\vec{r}_2)}{|\vec{r}_1 - \vec{r}_2|} \tag{4.2c}$$

where $n_p(\vec{r})$ is the proton number density.

The excitation energy of each FF is calculated by extracting the computed ground state energy of each FF from the energy of each FF in its rest frame. The FF ground state energy is computed with the HFBTHO code [91] for the corresponding FF neutron and proton numbers. The proton and neutron numbers of FFs are evaluated from

$$Z_f = \int_{V_f} d^3 r n_p(\vec{r}), \quad N_f = \int_{V_f} d^3 n_n(\vec{r}), \tag{4.3}$$

and the TXE is evaluated from

$$\mathrm{TXE} = E^*_{\mathrm{H}} + E^*_{\mathrm{L}}. \tag{4.4}$$

The energy variances of the TKE and TXE are only slightly larger than those of the initial energies. Compared to SeaLL1-2, the SeaLL1-1 starts at a larger excitation, and it has a longer average saddle-to-scission time ($\tau_{s\to s}$) and larger average TXE for the fission fragments, while their average TKEs are almost the same. When comparing the FFs characteristics emerging from simulations with SLy4 in Fig. 4.1 (see also section 4.2), we notice that in the case of enhanced pairing the scission configuration corresponds to a longer neck and lower TKE. This is also confirmed by the results obtained with NEDF SkM*-1 (enhanced pairing strength) and SkM*-2 (realistic pairing strength). Another particular aspect that emerges from our simulations is the character of the excitation energy sharing between the light and heavy fragments. In the case of SeaLL1-1 the light fragment has a larger excitation energy than the heavy fragment, while the case of SeaLL1-2 has the opposite pattern. These differences lead us to conclude that the excitation energy sharing in the cases of spontaneous fission and induced fission are different. This conclusion is in qualitative agreement with the observed wider mass yields for ^{239}Pu(n,f) when compared to ^{240}Pu (s.f.) [116, 117] .

It is instructive to express excitation energy of the FFs in terms of an internal temperature. We have used two different methods to extract this temperature. In the first approach, we have estimated the temperatures of the light and heavy fragments by the simple formula $E^*_f = A_f T_f^2/a$, where T_f is its temperature and $a \approx 10$ [4]. Such simple estimates are often used in simulations of the decay of the fission fragments using either Hauser-Fesbach or statistical evaporation models [121, 122, 123, 124].

We have also used a second approach to determine the FFs temperatures. We have performed full finite-temperature HFB calculations with the HFBTHO solver. Calculations were performed by constraining N_f, Z_f, $\langle\hat{Q}^f_{20}\rangle$ and $\langle\hat{Q}^f_{30}\rangle$ to the values extracted in the relaxed fragments, see Table 4.1, Table 4.2, and section 4.3.4. For each FF, we extract the temperature from the function $E^*_f(T)$ and find the corresponding T_f for the given E^*_f. This

NEDF	$E^*_{\rm ini}$	TKE	$N_{\rm H}$	$Z_{\rm H}$	$N_{\rm L}$	$Z_{\rm L}$	$E^*_{\rm H}$	$E^*_{\rm L}$	TXE	TKE+TXE	$\tau_{s\to s}$ (fm/c)
SeaLL1-1asy	7.9(1.7)	177.8(3.1)	83.4(0.4)	53.2(0.4)	62.9(0.5)	41.1(0.4)	17.1(3.0)	20.3(2.0)	37.4(3.1)	215.2(2.5)	2317(781)
SeaLL1-2asy	2.6(1.8)	178.0(2.3)	82.9(0.4)	52.9(0.2)	63.3(0.5)	41.5(0.3)	19.5(3.8)	14.0(1.9)	33.5(5.1)	211.5(3.3)	1460(176)
SeaLL1-sy	9.2	147.1	77.5	48.9	68.8	45.4	45.2	29.0	74.2	221.3	10103
SkM*-1asy	8.2(3.0)	174.5(2.5)	84.1(0.9)	53.0(0.5)	61.8(0.9)	40.9(0.5)	16.6(3.1)	14.9(2.3)	31.5(3.8)	206.0(2.4)	1214(448)
SkM*-1sy	9.6	149.0	73.4	47.2	72.6	46.7	29.4	28.5	57.9	206.9	3673
SkM*-2asy	8.1(0.2)	182.8(4.4)	82.6(1.0)	52.4(0.6)	63.6(1.0)	41.7(0.5)	14.3(3.9)	13.0(3.0)	27.3(3.4)	210.1(1.8)	1349(309)

Table 4.1: The NEDF, the initial excitation energy $E^*_{\rm ini}$, TKE, neutron, proton number number and excitation energies $N_{\rm H}$, $N_{\rm L}$, $Z_{\rm H}$, $Z_{\rm L}$ of the heavy and light fragments, total excitation energy of fragments TXE, and the sum of TKE and TXE, and the average saddle-to-scission times and their corresponding variances in parentheses. All energies are in MeV and S***sy, S***asy stand for symmetric and antisymmetric channels. Using Wahl's charge systematics [118] and data from Ref. [119] one obtains neutron ($N_L^{syst} \approx 61$ and $N_H^{syst} \approx 85$) and proton ($Z_L^{syst} \approx 40$ and $Z_H^{syst} \approx 54$. From Ref. [120] one obtains $\mathrm{TKE}^{syst} = 177 \ldots 178$.

calculation is more realistic than the simple estimate, even though (i) by constraining only $\langle \hat{Q}_{20} \rangle$ and $\langle \hat{Q}_{30} \rangle$, we do not obtain exactly the same shape as the actual fission fragments and (ii) the temperature thus obtained should be thought of as the maximum allowable value; see discussion in [125]. In Table 4.2, column 2 and 3 list the average and standard deviations of the temperature of light and heavy fragments in the first approach, and column 4 and 5 list the values in the second approach. These two approaches give comparable results that in SeaLL1-1 the light fragments have higher temperature than the heavy fragments while in SeaLL1-2 the opposite is true. The relaxed values of the average and of the standard deviations of the quadrupole and of the octupole moments of fragments, see Fig. 4.6 and section 4.3.4, are listed in column 6 to 9. In column 10 and 11 the ratio of the long to the short semi-axes of relaxed FFs are listed. As the initial state excitation energy increases, from SeaLL1-2 to SeaLL1-1, one notices that the extra energy mostly goes to the light FF. This suggests that the prompt fission spectrum of spontaneous and neutron-induced fission could be significantly different.

NEDF	$T_{\rm L}$ [MeV]	$T_{\rm H}$ [MeV]	$T_{\rm L}$ [MeV]	$T_{\rm H}$ [MeV]	$Q_{20}^{\rm L}$ [b]	$Q_{20}^{\rm H}$ [b]	$Q_{30}^{\rm L}$ [b$^{3/2}$]	$Q_{30}^{\rm H}$ [b$^{3/2}$]	$(c/a)_H$	$(c/a)_L$	$\tau_{s\to s}$ [fm/c]
SeaLL1-1	1.40(0.07)	1.11(0.08)	1.28(0.07)	1.16(0.07)	15.7(0.9)	2.6(0.5)	0.08(0.17)	−0.20(0.06)	1.06(0.01)	1.59(0.03)	2392(800)
SeaLL1-2	1.15(0.08)	1.19(0.12)	1.00(0.08)	1.21(0.08)	17.1(1.1)	2.6(0.6)	0.23(0.08)	−0.19(0.06)	1.06(0.01)	1.63(0.03)	1460(176)
SeaLL1-sy	1.54	1.99			27.4	27.0	0.9	-1.1	1.87	1.73	10103
SkM*-1asy	1.20(0.09)	1.10(0.10)			11.3(1.3)	3.5(0.9)	0.1(0.1)	−0.4(0.1)	1.08(0.02)	1.42(0.04)	1214(448)
SkM*-1sy	1.56	1.55			24.2	25.6	0.9	-1.0	1.72	1.75	3673
SkM*-2asy	1.11(0.14)	1.02(0.14)			14.5(1.7)	2.3(0.7)	0.09(0.08)	−0.3(0.1)	1.05(0.02)	1.53(0.06)	1349(309)

Table 4.2: Internal temperatures for the light $T_{\rm L}$ and heavy $T_{\rm H}$ fragments computed according to the simple estimate (columns 2 and 3) or finite-temperature HFB calculations (columns 4 and 5). The axial quadrupole and octupole moments of the fragments, the ratios of the long to the short semi-axes, as well as the average scission times are also listed

4.3.2 Collective flow energy

In some approaches that study fission dynamics, the saddle-to-scission process is regarded as an adiabatic process. The adiabatic assumption relies on the observations that the time scale of collective motions, which is in the range $\tau_{\rm ss} \sim 10^{-21}$ to 10^{-19} s, can be separated well with that one of the single particle excitations, which is estimated as $\tau_{\rm sp} = \hbar/\lambda_F c \approx 10^{-22}$ s. As a result, one may assume equilibrium at all times and decouple the large-amplitude motion of the system as a whole from internal excitations. In practice, this can be achieved by introducing a small set of collective variables such as multipole moments, pairing fields, etc., and precalculating the potential energy surface (PES) of the nucleus as a function of these variables. This strategy has been used to calculated the fission fragments yields, such as the time-dependent generator-coordinate method (TDGCM) [126, 127] and Langevin approaches [24, 32, 128, 129, 130]. However, adiabaticity, as defined in thermodynamics, means entropy remains constant and should not be confused with a quasistatic process. Fission dynamics from the saddle-to-scission is a quasistatic process, but not an adiabatic one.

The NEDF should satisfy the local Galilean covariance, which implies that the total

energy of the system, which is conserved, can be represented as a sum [131, 76, 132]

$$E_{\rm tot} = E_{\rm coll}(t) + E_{\rm int}(t) \equiv \int d^3\vec{r}\frac{mn(\vec{r},t)\vec{v}^2(\vec{r},t)}{2} + \int d^3\vec{r}\,\mathcal{E}\left(\tau(\vec{r},t) - n(\vec{r},t)m^2\vec{v}^2(\vec{r},t), n(\vec{r},t), \cdots\right), \tag{4.5}$$

where $n(\vec{r},t)$ is the number density, $\tau(\vec{r},t)$ is the kinetic density, and $\vec{p}(\vec{r},t) = mn(\vec{r},t)\vec{v}(\vec{r},t)$ are linear momentum and local collective/hydrodynamic velocity densities, and ellipses stand for various other densities. The first term in Eq. (4.5) is the collective/hydrodynamic energy flow $E_{\rm coll}$ and the second term is the intrinsic energy $E_{\rm int}$ in the local rest frame. For the sake of simplicity we have suppressed the spin and isospin DoF, even though they are included in the numerical examples discussed below. The collective energy $E_{\rm coll}(t)$ is not vanishing only in the presence of currents and vanishes exactly for stationary states. The inertia tensor in $E_{\rm coll}(t)$ in the case of irrotational collective motion is fully equivalent to the Werner-Wheeler inertial tensor [133]. The intrinsic energy $E_{\rm int}(t)$ is determined only by the matter distribution. A similar partition of the total energy of the nucleus exists in the TDGCM approach, see Ref. [134].

We have evaluated the collective flow energy during the saddle-to-scission evolution

$$E_{\rm coll} = \int d^3r \frac{\hbar^2}{2m}\frac{\vec{j}^2(\vec{r},t)}{n(\vec{r},t)}. \tag{4.6}$$

In the case of pure adiabatic evolution one expects a full conversion of the collective potential energy into a collective flow energy of $\approx 15\cdots20$ MeV.

Surprisingly, our simulations point to an unexpectedly small $E_{\rm coll}$ in the saddle-to-scission process, corresponding to a collective speed $v_{\rm coll}/c \approx 0.002\cdots0.004$, significantly smaller than the Fermi velocity $v_F/c \approx 0.25$, see Fig. 4.3 and Fig. 4.4. Since in TDDFT one simulates the one-body dynamics exactly, it is natural to discuss adiabaticity at the mean-field level. The transition rate between sp states is suppressed if the time to cross an avoided level-crossing configuration satisfies the restriction $\Delta t \ll \hbar/\Delta\epsilon \approx 400$ fm/c, where $\Delta\epsilon = 1/\rho_{\rm sp}(\epsilon_F)$ is the average s.p. energy level spacing at the Fermi level. Since on the way from saddle to scission several dozen of avoided level crossings occur [5, 135], this condition is clearly violated. The

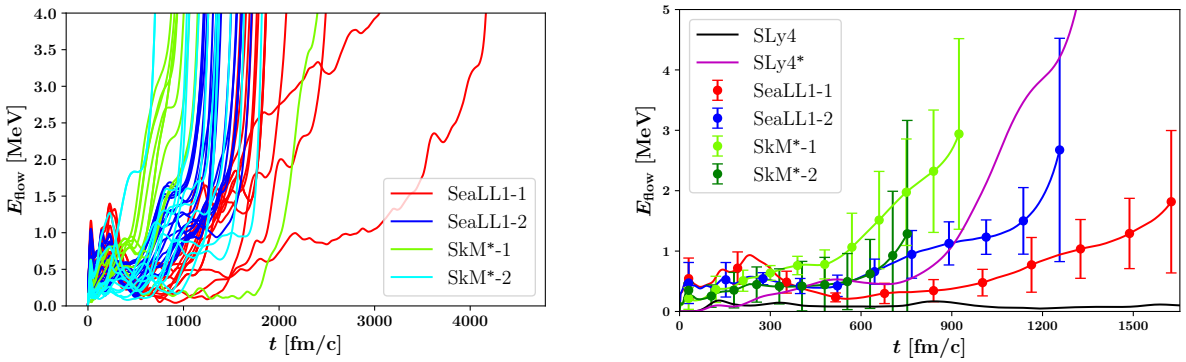

(a) (b)

Figure 4.3: The collective flow energy evaluated for NEDFs with realistic pairing SLy4 [45], enhanced pairing SLy4*, and for SkM*, and SeaLL1 sets. The error bars illustrate the size of the variations due to different initial conditions. In the case of enhanced pairing NEDF Sly4* the time has been scaled by a factor of 1/10.

collective motion is thus expected to be strongly overdamped. From saddle to scission the nucleus behaves as a very viscous fluid, the role of collective inertia is strongly suppressed, and the trajectories follow predominantly the direction of the steepest descent with the terminal velocity determined by the balance between the friction and the driving conservative forces, see Fig. 4.2.

This result serves as the first microscopic justification for the assumption of the overdamped Brownian motion model [24] and partially to the scission-point model [136, 137]. In both these phenomenological models it is assumed that the preformed FF are thermal equilibrium and that the collective energy flow is either vanishing or very small. The main difference is that in the scission-point model there is no mechanism to ensure that are such equilibrium scission configurations could be reached dynamically, while the nucleus evolves from the saddle-to-scission. It is equally surprising that in the case of enhanced pairing, when the pairing condensates retain their long-range order throughout the entire saddle-to-scission evolution, the collective dynamics has the same general characteristics. The present results put a lower limit of the role of the viscosity on fission times, as fluctuations can only lead

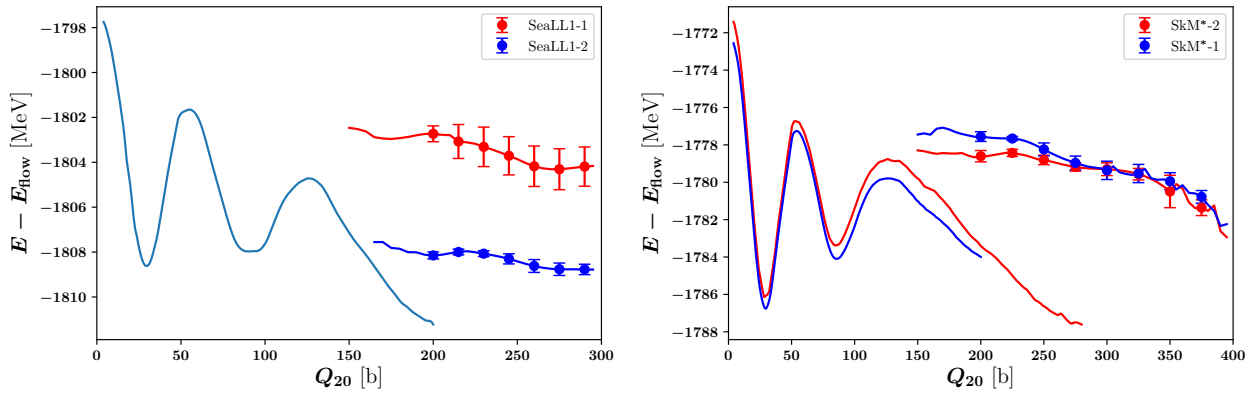

(a) (b)

Figure 4.4: The intrinsic energy $E_{\mathrm{int}}(t)$ along the fission path for SeaLL1 (upper panel) and SkM* (lower panel) along with the collective energy determined in a constrained calculation. In the case of an adiabatic evolution along the fission path $E_{\mathrm{int}}(t)$ would trace rather closely the potential energy determined in the constrained calculation. Scission configuration corresponds to a quadrupole momentum of the entire nuclear system $Q_{20} \approx 400$ b.

to longer trajectories (see chapter 5). The character of the collective dynamics unveiled here suggests that in physically realistic Langevin [24, 32, 128, 129, 130] and TDGCM [126, 127] studies the dynamics of the intrinsic DoF should be generated at (an approximately) fixed intrinsic energy, since E_{coll} is small up to scission. If the thermalization of the intrinsic DoF is achieved fast enough, the force driving the collective dynamics is determined by the free energy gradient [138]

$$\mathbf{F}_{\mathbf{Q}} = -\nabla_{\mathbf{Q}}[E_{\mathrm{int}}(\mathbf{Q}, T) - TS(\mathbf{Q}, T)], \tag{4.7}$$

where $S(\mathbf{Q}, T)$ is the entropy and

$$E_{\mathrm{tot}} = E_{\mathrm{int}}(\mathbf{Q}, T) + E_{\mathrm{coll}}(t) \approx E_{\mathrm{int}}(t). \tag{4.8}$$

In that case, for each set $\mathbf{Q}$ the temperature T shall be adjusted so that $E_{\mathrm{int}}(\mathbf{Q}, T)$ remains practically equal to its starting value, due to the smallness of $E_{\mathrm{coll}}(t)$. The intrinsic DoF

carry most of the entropy of the fissioning nucleus and that drives the fission dynamics until scission. Phenomenologically, such issues have been recently addressed by Randrup *et al.* [26, 139, 140], assuming that the collective motion is overdamped.

4.3.3 Relaxation of the collective degrees of freedom

To demonstrate the overdamped character of the fission dynamics, we performed the following theoretical experiment. We have applied at random times (the red dots in Fig. 4.5a), collective kicks to the nucleus of random intensities η according to the prescription

$$\begin{pmatrix} u_\alpha(\vec{r},t) \\ v_\alpha(\vec{r},t) \end{pmatrix} \rightarrow \begin{pmatrix} \exp[i\eta(2z^2-x^2-y^2)]u_\alpha(\vec{r},t) \\ \exp[-i\eta(2z^2-x^2-y^2)]v_\alpha(\vec{r},t) \end{pmatrix}, \tag{4.9}$$

which immediately resulted in an increase of the collective flow energy only. Immediately after such a kick the density distribution has the same profile as just before the kick, as the phase of the qpwfs do not affect number densities, but affect the currents and the kinetic energy density. After a relatively short time, of the order of a few 10's fm/c, this excess collective flow energy is rapidly dissipated into intrinsic energy and the nucleus is thus heated up, and this energy is never returned into the collective flow energy. After each collective "kick" the intrinsic energy of the nucleus increases, see Fig. 4.5b. Even though the intrinsic energy increases by $\approx$ 150 MeV after many collective "kicks", the absorption rate of the additional energy does not change obviously. This serves an additional argument that the one-body dissipation mechanism is very effective in bringing the collective flow velocity to the terminal velocity, which is achieved when the friction force cancels the driving force.

4.3.4 Shape relaxation of fission fragments

The one-body dissipation is important both before and after scission. The light fragment at scission is very elongated and both fragments have also a noticeable amount of octupole deformation, very different than the corresponding moments in the ground state. In Fig. 4.6 we show the evolution of Q_{20} and Q_{30} for both FFs before and after scission. All these

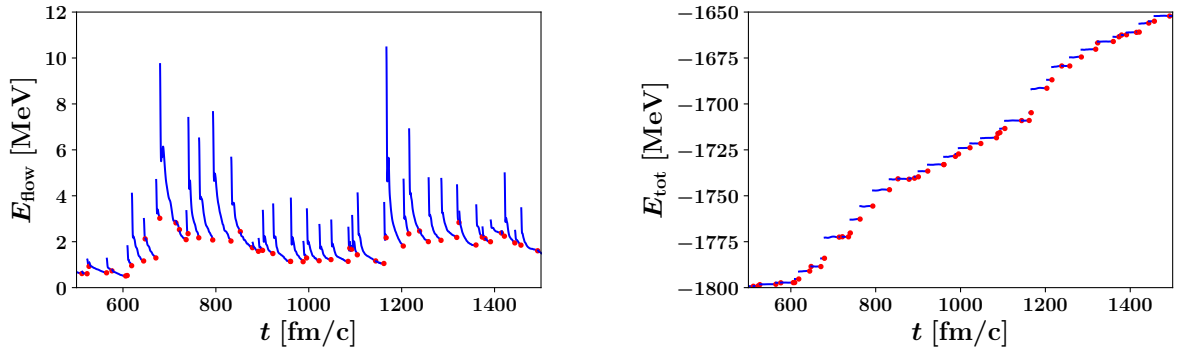

(a) (b)

Figure 4.5: (a) At times indicated with red dots we have applied collective quadrupole momentum kicks to both neutrons and protons, see Eq. (4.9), with random values of η, see Eq. (4.9). (b) The time evolution of the total energy of the nucleus, in the rest frame of the nucleus, after we have applied collective kicks were to both neutrons and protons with random values of η, see Eq. (4.9).

moments relaxed rather rapidly, without performing any oscillations to the values very close to the ground state values. Remember however that both FFs are not cold. The absence of shape oscillations is another strong indication that one-body dissipation is strong and that even the individual FFs large amplitude collective motion is overdamped always. The relatively large quadrupole deformation energy of the light fragment is thus converted into heat and its quadrupole moment is reduced. Both fragments are octupole deformed at scission, and these octupole moments relax to relatively small values.

4.3.5 Neutrons emitted by fission fragments

Neutron emission is an important mechanism in the de-excitation of FF. We have also estimated the neutron emission rates before the FFs are fully separated, 4.0×10^{-4} neutrons/(fm/c), which are rather stable with respect to the variation of initial conditions, deformation, initial energy, or NEDF. By the time the FFs reach a separation of ≈ 60 fm we find that about 0.4 neutrons are emitted on average, in fair agreement with theoretical

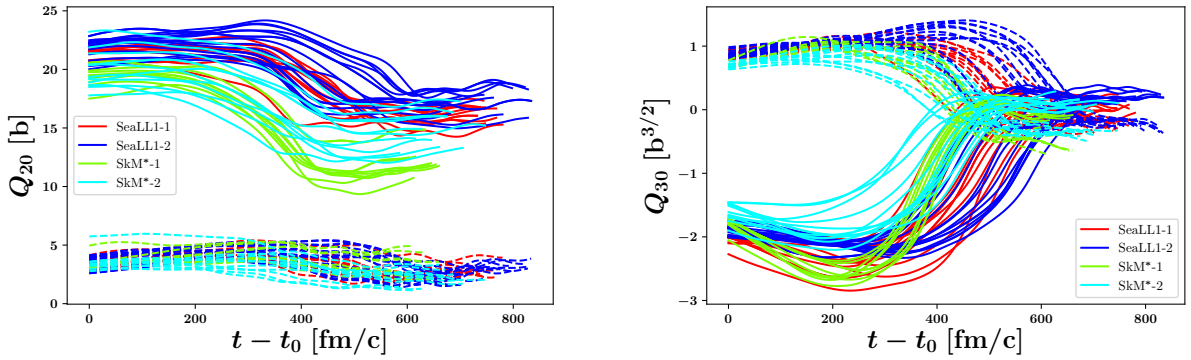

(a) (b)

Figure 4.6: The evolution of the quadrupole Q_{20} and octupole Q_{30} moments of the light (solid lines) and heavy (dashed lines) FFs before and after scission. The time t_0 stands for the moment when the distance of two fragments is 15 fm and the neck of mother nucleus is formed. Scission occurs at $t - t_0 \approx 300$ fm/c.

estimates obtained in the sudden limit approximation [141] and with experimental hints of neutrons emitted before full acceleration [142, 143, 144, 145].

In Fig. 4.7 we show the number of neutrons in the volume where the number density $n(\boldsymbol{r}, t) \leq 10^{-5}$ fm^{-3} as a function of time after scission for all the fission trajectories we have evaluated. The neutron emission rates (the slopes) demonstrate a robust independence on the initial conditions or the NEDF used. These neutrons are emitted preferentially parallel to the FFs motion, a conclusion likely affected by the finite transverse size of simulation boxes.

4.4 Summary

The present study is the first in literature in which no restrictions have been imposed on the meanfield dynamics and the pairing field was beyond the BCS approximation. In TDHF+BCS treatments reported so far in literature a relatively low-energy cutoff was always imposed on the energy band where pairing correlations are active. Arguments are often presented that such a limited space for pairing correlation is sufficient, as the energy gain

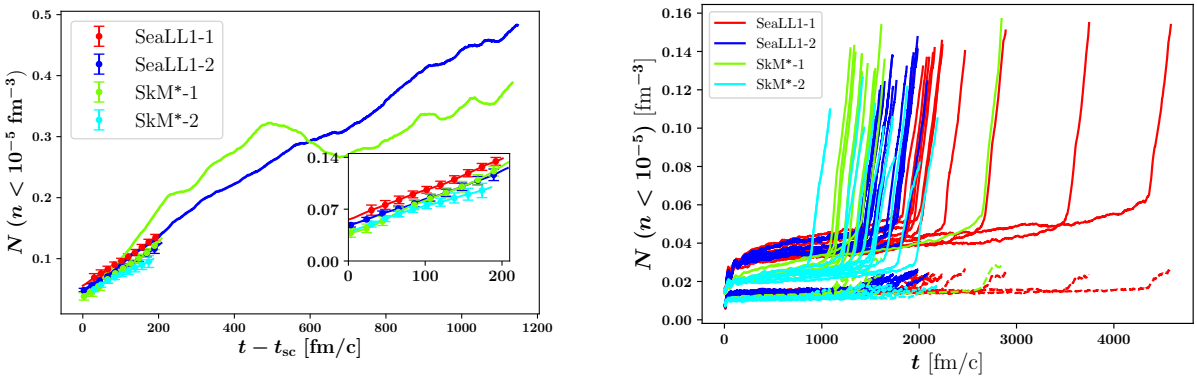

(a) (b)

Figure 4.7: (a) The number of neutrons emitted predominantly after scission. The error bars quantify the size of the fluctuations between trajectories corresponding to different initial conditions; (b) The number of neutrons emitted in each trajectories in the inset of (a).

is reproduced with enough accuracy. But as Anderson notes [146], when he discusses the "Quantum Chemists' Fallacy No. 1 and 2," of which even Wigner was partially guilty, "you may get pretty good energetics out of qualitatively wrong state." On the other hand it is well known that pairing correlation in nuclei, unlike in superconductors for example, are due to short range attractive forces, and that is inconsistent with the assumption that pairing correlations are active in a narrow energy window only. In particular this is also true for the popular finite range Gogny force [147], in which case the pairing cutoff energy could be as high as $\mathcal{O}(100)$ MeV. As we do not implement any arbitrary energy cutoff on pairing correlations, we are able to perform for the first time in literature a microscopic test on whether the LACM fission dynamics is indeed adiabatic in character.

Adiabaticity in LACM is typically conflated with slowness of the collective motion [148, 149, 150, 70, 133, 22], an assumption which allows one to introduce collective DoF which are uncoupled from the intrinsics DoF. Until now the validity of this assumption has not been checked, since the required simulations exceeded the computer capabilities of previous

researchers. The only previous attempt we are aware of was performed by [151], who however were unable to arrive at a conclusive decision, basically because the phase space they were able to consider at the time, was clearly too small.

One-body dissipation [152] is automatically incorporated in TDDFT and it was considered for many years to be important in LACM. Ref. [36] concluded that one-body dissipation is important in fission dynamics, based however on studying only three TDHF trajectories for fission of ^{238}U, with three values for a static pairing field $\Delta = 0.7$, 2.0, and 6.0 MeV and comparing these results with classical Langevin simulation of fission dynamics, with one-body dissipation estimated for a Fermi gas model. From this type of comparison these authors concluded that one-body dissipation is important in fission dynamics. Over the years the practitioners of the Langevin type of simulations have claimed that both one-body and two-body dissipation are both important in low energy fission dynamics [138, 32, 128, 129, 130], using phenomenologically adjusted dissipation coefficients, though it is not always clear how one can disentangle the two forms of dissipation, see e.g. discussion by Ref. [32]. Not all Langevin implementations are compatible with one another, though the level of agreement with data is about the same. Moreover there are TDGCM simulations [127, 153], in which the nature of fluctuations is qualitatively different, but the quality of the agreement with experiment for FFs mass yields are comparable with those achieved in Langevin approaches. All this might suggest that the FFs mass yields are likely not very sensitive to the nature and details of various models.

Only in the last few years Randrup and collaborators [24, 25, 26, 139, 140] took this assumption to the extreme and suggested that fission dynamics is actually overdamped and one should replace the Langevin approach with the Smoluchowski approach. In this case the role of the collective inertia becomes irrelevant and surprisingly extremely accurate description of fission yields, TKE, and TXE can be achieved.

If dissipation is important in fission dynamics the introduction of collective DoF freedom, of a potential energy surface and of a collective inertia, and the decoupling of the DoF into collective and intrinsic becomes highly questionable. We have establish that one-body

dissipation is very strong and that in fission LACM is strongly overdamped under almost any reasonable assumptions. Under such circumstances the role of "collective inertia" becomes irrelevant and the theoretical arguments in favor of TDGCM/ATDHF approach or Langevin approach become questionable as well as the mere definition of collective variables.

We have determined that the memory of the initial conditions near the outer barrier are rather quickly forgotten, in a relaxation time $\tau_{\rm relax} \approx \mathcal{O}(10^2)$ fm/c. As the saddle-to-scission is $\tau_{s\to s} \approx \mathcal{O}(10^3 \ldots 10^4)$ fm/c, the widths of the FFs mass, charge, TKE, TXE, and spin distributions are determined during this relatively fast non-equilibrium evolution interval, due to the presence of non-negligible fluctuations.

We have used three different NEDFs (SLy4, SeaLL1, and SkM*), with some variations in treating the pairing correlations, and our conclusions were quite robust. All these NEDFs satisfy basic constraints: the nuclear matter is liquid in nature (thus mostly incompressible), the surface tension, the isospin asymmetry, the spin-orbit, and the pairing correlations have realistic values. When all these basic requirements are satisfied the emerging most likely values for the TKE, atomic, and charge numbers are in agreement with experiment without the need of any additional fitting. In addition we were able to extract the excitation energy sharing between the FFs. Depending on the initial energy of the fissioning nucleus the excitation energy sharing changes in a manner which appears to be in agreement with experimental data. The only disadvantage of the present approach is that it lacks fluctuations, which likely could be later added (see chapter 5). Upon introductions of fluctuations one should be able extract FFs mass, charge, TKE, and TXE distributions. Many other quantities of interest for various applications could also be extracted, such as the angular momentum distributions of the FFs and their parities.

Chapter 5

FLUCTUATIONS AND DISSIPATIONS

5.1 Introduction

The main results we presented in chapter 4 show that the difference in initial conditions is largely washed out during the long time evolution in TDDFT, leading to very small distribution widths of various observables . This behavior illustrates one of the major limitations of DFT, which lacks a method to evaluate two-body observables such as the width of the FFs mass and charge yields and of the total TKE of the FFs. A long time ago, Balian and Veneroni (BV) proposed a prescription to estimate these quantities within the framework of the TDHF approach [154], and this prescription, also named the time-dependent random phase approximation (TDRPA), was applied to estimating the width of particle number distributions in the fragments of ^{258}Fm fission [40]. However, the width predicted by TDRPA in Ref. [40] is also much less than the experimental observations.

Since an accurate solution of the time-dependent Schrödinger equation with realistic nucleon interactions will be out of reach for a very long time (if ever), the question arises: what would be a reliable microscopic approach? A Feyman's real-time path integral formulation [155, 156] of quantum many-body systems is particularly appealing as it can lead to good approximate and accurate at the same time treatments. The many-body wave function is represented as a sum over all possible paths joining the initial and final configurations, with appropriate weights:

$$\Psi(t) = \int \mathcal{D}[\sigma(t)] W[\sigma(t)] \exp\left(-\frac{i}{\hbar}\int_{t_i}^{t_f} \hat{h}[\sigma(t)]\right) \Psi(0). \tag{5.1}$$

where $\mathcal{D}[\sigma(t)]$ is an appropriate measure depending on all auxiliary fields, $W[\sigma(t)]$ is a Gaussian weight and $\hat{h}[\sigma(t)]$ is a one-body Hamiltonian built with the auxiliary one-body fields

$\sigma(t)$. $\Psi(0)$ is the initial wavefunction, often chosen as a (generalized) Slater determinant. Thus, the true many-nucleon wavefunction is now a time-dependent linear superposition of many time-dependent (generalized) Slater determinants. In this respect the true many-nucleon wavefunction has a similar mathematical structure with the wavefunction in the time-dependent generator coordinate method (TDGCM) introduced by Wheeler *et al.* [14, 157]. One cannot fail but see here also the analogy in treating fluctuations around the mean field trajectory with the classical Langevin description of nuclear collective motion as well [138].

The description of the dynamics of a small system in interaction with a very large reservoir is one of the oldest problems in many-body physics, starting perhaps with the 1828 work of Robert Brown and Brownian motion, followed by the illustrious theoretical studies of Einstein, Langevin, Fokker, Planck, Kramers, and a great number of others [158, 159]. If there are no memory effects, for a free Brownian particle of mass m, in the Markov approximation one can use the stochastic Langevin equation, which in one dimension reads

$$m\ddot{x}(t) = F(x(t)) - m\gamma\dot{x}(t) + m\xi(t). \tag{5.2}$$

Here $\xi(t)$ is a Gaussian white noise

$$\langle\xi(t)\rangle = 0, \quad \langle\xi(t)\xi(t')\rangle = \Gamma\delta(t-t'), \tag{5.3}$$

where the angle brackets stand for statistical averaging. The strength of the damping γ and of stochastic forces Γ are related by the Einstein dissipation fluctuation theorem

$$m\Gamma = 2\gamma T, \tag{5.4}$$

where T is the temperature.

Appropriate implementations of the Langevin equation have been used in nuclear fission for decades, see Refs. [31, 24, 128, 32, 129, 130] and earlier references therein, in order to describe the dissipative character of the the fission fragments yields. In previous works, the authors typically select a few characteristics of the number density $n(\vec{r}, t)$ (e.g. elongation of the nucleus, mass asymmetry, neck size, and two quadrupole deformations of the fragments).

For these collective variables one constructs a potential energy surface, an inertia and a dissipation tensor and assumes the existence of coupled Langevin equations solved in a collective space spanned by the collective coordinate x_i like

$$\frac{dp_i}{dt} = -\frac{p_j p_k}{2}\frac{\partial}{\partial x_i}(\mathcal{M}^{-1})_{jk} - \frac{\partial V}{\partial x_i} - \eta_{ij}(\mathcal{M}^{-1})_{jk}p_k + g_{ij}\Gamma_j(t), \tag{5.5a}$$

$$\frac{dx_i}{dt} = (\mathcal{M}^{-1})_{ij}p_j, \tag{5.5b}$$

where p_i represents the momentum conjugate to x_i, η_{ij} is the dissipation tensor, $g_{ij}\Gamma_j(t)$ is the random (Langevin) force with $\Gamma(t)$ being a time-dependent stochastic variable with a Gaussian distribution, and g_{ij} is the random-force strength tensor. The potential energy V is obtained from the macroscopic-microscopic method [31, 24, 128, 32] or self-consistent mean-field method [129, 130]. The inertia tensor $\mathcal{M}_{ij}$ is derived from phenomenological models or by the generator coordinate method (GCM). Due to the limitation of computational resources, the number of collective variables x_i is usually no more than five.

In this chapter [1], instead of limiting the number of collective DoF to a small number of chosen characteristics or moments of the number density $n(\vec{r}, t)$, we will consider the entire number density as our chosen set of collective DoF and treat them in a fully quantum formalism at a finite temperature, which is controlled by the intrinsic DoF. We argue that one can add carefully chosen additional terms to the usual TDDFT equations to simulate both dissipation and fluctuations of the nuclear collective motion and maintain at the same time the unitary character of the evolution, a distinctive characteristic of TDDFT. Since fluctuations are random, observables will have to be evaluated as ensemble averages over these realizations.

5.2 Theoretical formalism

It is well-known that the TDDFT and other time-dependent mean-field methods like TDHF(B) can provide a good description for the average properties of one-body DoF. The mean-field

[1] This chapter is based on the work by A. Bulgac, S. Jin and I. Stetcu, *Unitary evolution with fluctuations and dissipation*, arXiv:1805.08908 [160] with minor modifications.

equations, number density, current density and local collective velocity, and the continuity equation have the generic form

$$i\hbar\dot{\psi}_k(\vec{r},t) = h[n]\psi_k(\vec{r},t), \tag{5.6a}$$

$$n(\vec{r},t) = \sum_k |\psi_k(\vec{r},t)|^2, \tag{5.6b}$$

$$\vec{j}(\vec{r},t) = \frac{\hbar}{2i}\sum_k (\psi_k^*(\vec{r},t)\vec{\nabla}\psi_k(\vec{r},t) - \psi_k(\vec{r},t)\vec{\nabla}\psi_k^*(\vec{r},t)), \tag{5.6c}$$

$$\dot{n}(\vec{r},t) + \vec{\nabla}\cdot\vec{j}(\vec{r},t) = 0. \tag{5.6d}$$

What is missing in this approach is the quantum fluctuations in the collective motion. Over the years, many efforts have been made to introduce stochastic elements into the mean-field methods [161, 162, 163]. Generally one needs to add an additional contribution to the equations for the single particle wavefunctions:

$$i\hbar\dot{\psi}_k(\vec{r},t) = h[n]\psi_k(\vec{r},t) + \delta h_k(\vec{r},t) \tag{5.7}$$

The addition term δh_k should reflect the impact of the rapid fluctuations brought by the intrinsic nucleon motions. After long time averaging the contributions of δh_k should vanish, which makes the Eq. (5.7) return to the original mean-field equations Eq. (5.6a). Since we want to produce quantum fluctuations on the collective motion, we first try to modify the collective flow $\vec{j}(\vec{r},t)$ by adding a "stochastic" velocity field $\vec{u}(\vec{r},t)$ to the kinetic term of the hamiltonian by

$$\frac{(\hat{\vec{p}} - m\vec{u})^2}{2m} = \frac{\hat{\vec{p}}^2}{2m} - \frac{1}{2}(\vec{u}\cdot\hat{\vec{p}} + \hat{\vec{p}}\cdot\vec{u}) + \frac{m\vec{u}^2}{2}. \tag{5.8}$$

and the resulting Schrödinger equations become

$$i\hbar\dot{\psi}_k(\vec{r},t) = h[n]\psi_k(\vec{r},t) - \frac{1}{2}(\vec{u}\cdot\hat{\vec{p}} + \hat{\vec{p}}\cdot\vec{u})\psi_k(\vec{r},t) + \frac{m\vec{u}^2}{2}\psi_k(\vec{r},t) \tag{5.9}$$

The presence of this random velocity field leads to an additional contribution to the total energy of the system

$$E_{\rm tot} \to E_{\rm tot} - \int d^3r\vec{u}(\vec{r},t)\cdot\vec{j}(\vec{r},t) + \int d^3r\frac{m\vec{u}^2(\vec{r},t)}{2}n(\vec{r},t). \tag{5.10}$$

The fluctuations in Eq. (5.9) can be introduced in another way. Consider a gauge transformation for the wavefunctions by

$$\psi_k(\vec{r},t) = \phi_k(\vec{r},t)\exp[i\chi(\vec{r},t)]. \tag{5.11}$$

Then the gauge invariance implies that if

$$i\hbar\dot{\psi}_k(\vec{r},t) = \frac{\vec{p}^2}{2m}\psi_k(\vec{r},t) + U(\vec{r},t)\psi_k(\vec{r},t), \tag{5.12}$$

then the new wavefunctions $\phi_k(\vec{r},t) = \psi_k(\vec{r},t)\exp[-i\chi(\vec{r},t)]$ satisfy the equations

$$i\hbar\dot{\phi}_k(\vec{r},t) = \frac{[\vec{p}-\hbar\vec{\nabla}\chi(\vec{r},t)]^2}{2m}\phi_k(\vec{r},t) + [U(\vec{r},t)+\hbar\dot{\chi}(\vec{r},t)]\phi_k(\vec{r},t). \tag{5.13}$$

Comparing Eq. (5.9) and Eq. (5.13), if the vector field $\vec{u}(\vec{r},t)$ is irrotational $\vec{\nabla}\times\vec{u}(\vec{r},t) = 0$, representing the single particle wavefunctions in Eq. (5.9) as $\psi_k(\vec{r},t) = \phi_k(\vec{r},t)\exp[i\chi(\vec{r},t)]$ one can then eliminate the vector potential $m\vec{u}(\vec{r},t) = \hbar\vec{\nabla}\chi(\vec{r},t)$ in the favor of a "stochastic" scalar potential $\hbar\dot{\chi}(\vec{r},t)$

$$i\hbar\dot{\phi}_k(\vec{r},t) = h[n]\phi_k(\vec{r},t) + \hbar\dot{\chi}(\vec{r},t)\phi_k(\vec{r},t). \tag{5.14}$$

In general, one could produce both rotational and irrotational velocity fields by including both scalar and vector channels of the fluctuations into the equations like

$$i\hbar\dot{\psi}_k(\vec{r},t) = h[n]\psi_k(\vec{r},t) - \frac{1}{2}\left[\vec{u}(\vec{r},t)\cdot\hat{\vec{p}} + \hat{\vec{p}}\cdot\vec{u}(\vec{r},t)\right]\psi_k(\vec{r},t) + u_0(\vec{r},t)\psi_k(\vec{r},t), \tag{5.15}$$

where $\vec{u}(\vec{r},t)$ and $u_0(\vec{r},t)$ are treated as independent components of the four-vector $u_\nu(\vec{r},t), \nu = 0,1,2,3$. Following the same idea in the Langevin approach, we formulate $u_\nu(\vec{r},t)$ to be a stochastic function both in time and space with the summations of Gaussian-like functions.

$$u_\nu(\vec{r},t) = \sqrt{\Gamma}\sum_{k=1}^{N_k}\frac{1}{(\pi\tau_k^2)^{1/4}}\exp\left[-\frac{(t-t_k)^2}{2\tau_k^2}\right]\eta_k(\vec{r}), \tag{5.16}$$

$$\eta_k(\vec{r}) = \sqrt{\frac{1}{N_{kb}}}\sum_{l=1}^{N_{kb}}\frac{s_{kl}}{(\pi a_{kl}^2)^{3/4}}\exp\left[-\frac{(\vec{r}-\vec{r}_{kl})^2}{2a_{kl}^2}\right], \tag{5.17}$$

$$\langle t_k - t_{k-1}\rangle \propto \langle\tau_k\rangle, \tag{5.18}$$

$$\langle\tau_k\rangle = \mathcal{O}\left(\frac{mR_A}{\hbar k_F}\right), \langle\tau_k\tau_l\rangle \propto \delta_{kl}, \tag{5.19}$$

$$\langle N_{kb}\rangle = \mathcal{O}(A), \langle N_{kb}N_{lc}\rangle \propto \delta_{kl}\delta_{bc} \tag{5.20}$$

$$\langle s_{kl}\rangle = 0, \quad \langle s_{kl}s_{mn}\rangle = \delta_{km}\delta_{ln}, \tag{5.21}$$

$$\langle|\vec{r}_{kl}|\rangle = \mathcal{O}(R_A), \langle\vec{r}_{kl}\vec{r}_{mn}\rangle \propto \delta_{km}\delta_{ln}, \tag{5.22}$$

$$\langle a_{kl}\rangle = \mathcal{O}\left(\frac{\pi}{k_F}\right), \langle a_{kl}a_{mn}\rangle \propto \delta_{km}\delta_{ln} \tag{5.23}$$

where $R_A = r_0 A^{1/3}$ is the radius of the nucleus, $\varepsilon_F = \hbar^2 k_F^2/2m$ is the Fermi energy, A is the particle number, Γ is a parameter controlling the variance of the time-averaged "stochastic" noise, t_k are random times at which "kicks" are applied, τ_k is the time-width of an individual "kick" comparable to the nucleon crossing the system time, which can be made random as well, $\eta_k(\vec{r})$ is the spatial profile of the "kick," which is the sum of gaussian "kicks" centered at random positions $\vec{r}_{kl}$, of random spatial widths a_l, and random strengths s_{kl}. The number of the spatial kicks N_{kb} should be comparable to the number of nucleons A. All these random numbers are assumed to be uncorrelated. One then clearly has the following relations

$$\int d^3\vec{r}\langle\eta_k(\vec{r})\rangle = 0, \ \int d^3\vec{r}\langle\eta_k(\vec{r})\eta_l(\vec{r})\rangle = \delta_{kl}, \tag{5.24}$$

$$\int_0^t dt'\int d^3\vec{r}\langle u_\nu(\vec{r},t')\rangle = 0, \int_0^t dt'\int d^3\vec{r}\langle u_\nu^2(\vec{r},t')\rangle \approx \Gamma\langle N_k\rangle, \tag{5.25}$$

$$\int_0^t dt'\int d^3\vec{r}\langle u_\nu(\vec{r},t')u_\nu(\vec{r},t'+\Delta t)\rangle \approx 0, \ \Delta t \gg \langle\tau_k\rangle, \tag{5.26}$$

where $t \approx \langle N_k\rangle\langle\tau_k\rangle$. In the limits $\lim_{\tau\to 0} F^2(t,\tau) = \delta(t)$, $\lim_{a\to 0} G^2(\vec{r},a) = \delta(\vec{r})$, $\tau_k \to 0$, and $N_{kb} = 1$ one recovers the Gaussian white noise used in typical treatment of stochastic equations [164, 158].

Besides the fluctuation terms introduced in Eq. (5.15), one also needs to introduce a dissipation term in analogy to the one in the Langevin equation Eq. (5.5). The TDDFT dynamics automatically incorporates the one-body dissipation mechanism [152]. Additional "quantum friction" term is needed to conteract the heating due to the stochastic fields $u_0(\vec{r},t)$ and $m\vec{u}(\vec{r},t)$. We use the potential introduced in Ref. [165] as a quantum friction to damp the collective motion of the system.

$$V_{\text{fric}}(\vec{r},t) \propto \gamma\dot{n}(\vec{r},t) = -\gamma\vec{\nabla}\cdot\vec{j}(\vec{r},t). \tag{5.27}$$

One can show that in the presence of this "quantum friction" term alone the system will be cooled $\dot{E}_{\text{tot}} \leq 0$ and the collective velocity will vanish $\lim_{t\to\infty}\vec{v}(\vec{r},t) = 0$ [165], similarly to the classical Langevin equation. In the case of a Brownian particle, one follows the dynamics of the Brownian particle alone, but not the effects on the dynamics of the fluid and the total energy of the fluid and Brownian particle are not conserved. In a TDDFT augmented with dissipation and fluctuations one follows the coupled dynamics of both collective and intrinsic DoF within a stochastic framework.

Finally, the TDDFT evolution equations augmented to incorporate dissipation and fluctuations we introduce have the form

$$\begin{aligned} i\hbar\dot{\psi}_k(\vec{r},t) &= h[n]\psi_k(\vec{r},t) + \gamma\dot{n}(\vec{r},t)\psi_k(\vec{r},t) \\ &- \frac{1}{2}\left[\vec{u}(\vec{r},t)\cdot\hat{\vec{p}} + \hat{\vec{p}}\cdot\vec{u}(\vec{r},t)\right]\psi_k(\vec{r},t) + u_0(\vec{r},t)\psi_k(\vec{r},t). \end{aligned} \tag{5.28}$$

The ratio $\Gamma/\gamma \propto \mathrm{T}$ controls the temperature of the intrinsic system, similarly to Einstein fluctuation-dissipation theorem. There are at least two independent coupling strengths Γ (of appropriate dimension), one for $\vec{u}(\vec{r},t)$ and the other for $u_0(\vec{r},t)$.

5.3 Results

5.3.1 Test case: 1D harmonic oscillator

As a benchmark, We first implement this approach in the case of a nucleon in a 1D harmonic oscillator with a "quantum friction potential" as described above and a stochastic field

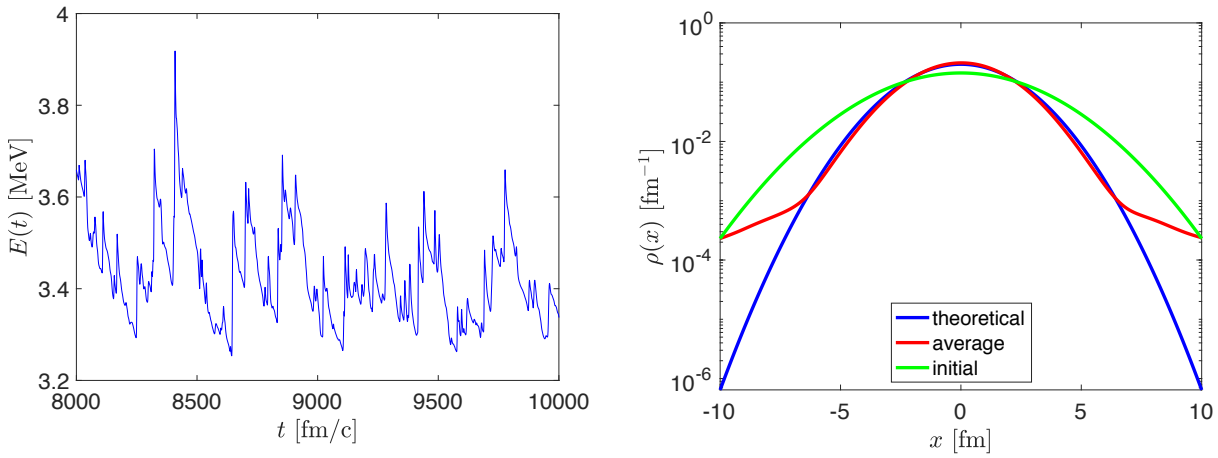

(a) (b)

Figure 5.1: (a): The expectation value of the energy of the 1D harmonic oscillator as a function of time. (b): The initial, final $\rho(x) = \frac{1}{\tau}\int_0^\tau dt|\psi(x,t)|^2$, and expected theoretical density distribution, using the temperature estimated from Eq. (5.30). By increasing the simulation time one can improve on the tails of the calculated density distribution.

$\Gamma(x,t) = u_0(x,t)$ only

$$i\hbar\frac{\partial}{\partial t}\dot{\psi}(x,t) = -\frac{\hbar^2}{2m}\nabla^2\psi(x,t) + \frac{1}{2}m\omega^2x^2\psi(x,t) + \gamma\dot{n}(x,t)\psi(x,t) + \Gamma(x,t)\psi(x,t), \tag{5.29}$$

where $\hbar\omega = 6$ MeV. Starting with a somewhat arbitrary initial state, after some time the harmonic oscillator reaches a steady-state solution at a temperature $T = 1/\beta$ determined from the condition

$$\begin{aligned}
&\frac{1}{\tau}\int_0^\tau dtE(t) = \frac{1}{Z(\beta)}\sum_{n=0}^{\infty}e^{-\beta\varepsilon_n}\varepsilon_n,\\
&Z(\beta) = \sum_{n=0}^{\infty}e^{-\beta\varepsilon_n}, \quad \varepsilon = \hbar\omega\left(n+\frac{1}{2}\right),\\
&\rho(x) = \lim_{\tau\to\infty}\frac{1}{\tau}\int_0^\tau dt|\psi(x,t)|^2 \approx \frac{1}{Z(\beta)}\sum_{n=0}^{\infty}e^{-\beta\varepsilon_n}|\phi_n(x)|^2,
\end{aligned} \tag{5.30}$$

where $\phi_n(x)$ are the 1D harmonic oscillator eigenfunctions.

In Fig. 5.1a we display the mean value of the energy of the 1D oscillator as a function of the simulation time, illustrating that the system attained a steady-state regime. In Fig. 5.1b we show the initial, expected, and computed equilibrium density distributions. We put a minimal effort into the fine-tuning of the parameters of the "quantum friction potential," the stochastic field, and the length of the simulation time.

5.3.2 Fission yields by hydrodynamics approach

The Langevin approach usually requires a considerable number of random trajectories for each initial condition. For the full TDDFT approach, the time cost for each trajectory is already very expensive. To reduce computational cost we first implement this fluctuations and dissipation in the nuclear hydrodynamics approach. At zero temperature within Landau's two-fluid hydrodynamics, only the superfluid components survive and the dynamics reduces to that of a neutron and a proton perfect fluids. In hydrodynamics, the complex "wavefunction" for each neutron and proton channel has the form

$$\psi_q(\vec{r}) = \sqrt{n_q(\vec{r})}\exp(i\phi_q(\vec{r})) \tag{5.31}$$

with the number density $n_q(\vec{r})$ and the phase $\phi_q(\vec{r})$, which is related to the local fluid velocity

$$\vec{v}_q(\vec{r}) = \frac{\hbar}{m}\vec{\nabla}\phi_q(\vec{r}). \tag{5.32}$$

The energy density functional for the hydrodynamics model should satisfy the Galilean invariance, which has the form

$$\mathcal{E}_{\rm tot} = \sum_q \frac{\hbar^2}{2m}|\vec{\nabla}\psi_q(\vec{r})|^2 + \overbrace{\mathcal{E}_{\rm homo} + \mathcal{E}_{\rm Coul} + \mathcal{E}_{\rm surf}}^{\mathcal{E}_{\rm int}}. \tag{5.33}$$

The homogeneous part $\mathcal{E}_{\rm homo}$ and the Coulomb part $\mathcal{E}_{\rm Coul}$ have the same forms with the ones in the SeaLL1 EDF in chapter 3, which reproduces the symmetric nuclear matter density,

the saturation density, the symmetry energy, and the Coulomb energy. The surface term has the form

$$\mathcal{E}_{\rm surf} = \frac{\hbar^2}{2m}(\vec{\nabla} n(\vec{r}))^2 (C + Dn(\vec{r})) \tag{5.34}$$

where $n(\vec{r}) = n_n(\vec{r}) + n_p(\vec{r})$ is the isocalar number density. The values of C and D

$$C = -2.8622 \text{ fm}^3, \quad D = 9 \text{ fm}^6 \tag{5.35}$$

are chosen to accurately reproduce the nuclear surface tension

$$\sigma = \int dz \left[\mathcal{E}_{\rm int}\left(n(z)\right) - \mu n(z)\right] \approx 1 \text{ MeV/fm}^2. \tag{5.36}$$

where $\mu = -15.6$ MeV is the chemical potential for infinite symmetric nuclear matter and $n(z)$ and $\tau(z)$ are the number and kinetic density distribution for semi-infinite symmetric nuclear matter.

Including the (isoscalar) fluctuations and dissipation, the derived hydrodynamics equation is

$$i\hbar\dot{\psi}_q(\vec{r},t) = -\frac{\hbar^2}{2m}\nabla^2\psi_q(\vec{r},t) + \frac{\delta\mathcal{E}_{\rm int}}{\delta n(\vec{r},t)}\psi_q(\vec{r},t) + \gamma[n]\dot{n}(\vec{r},t)\psi_q(\vec{r},t) + u_0(\vec{r},t)\psi_q(\vec{r},t). \tag{5.37}$$

We solve the hydrodynamics equation for ^{258}Fm fission. The hydrodynamic equations do not include pairing and shell effects and the ground states for typical nuclei have spherical symmetry. Starting from the ground state of ^{258}Fm, we give a boost on the initial wavefunction by introducing the phase factor $\phi_q(\vec{r},0) \propto (2z^2 - x^2 - y^2)$, which corresponds to an initial excitation energy around $E^* = 7$ MeV. Without any fluctuations (and dissipation) incorporated in the evolution, symmetric fission fragments will be obtained. The inclusion of dissipation and fluctuations leads to wide mass distributions which are comparable with the observed ones. Fig. 5.2 shows the mass and TKE distributions with different strengths of fluctuations Γ. The mass distributions display a symmetric pattern centered on $A_L = A_H = 129$. The mean of the TKE distribution in a hydrodynamic approach is significantly smaller than the observed one (> 200 MeV), as the fissioning nucleus develops

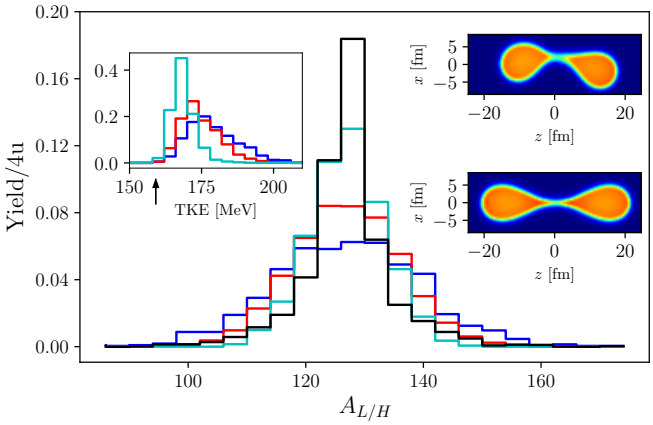

Figure 5.2: (Color online) The mass yields obtained solving the quantum hydrodynamics equations Eq. (5.37) including fluctuations and dissipations, obtained using different strengths $\Gamma = 0.1$ (blue), 0.05 (red), and 0.02 (cyan) MeV of the fluctuating field $u_0(\vec{r}, t)$ (keeping Γ/γ fixed), compared to experimental data (black) [166] for induced fission of ^{258}Fm. The widths of either the mass or of the TKE distributions are approximately proportional to $\sqrt{\Gamma}$. In the insets we show the TKE distributions and typical nuclear shapes at scission with and without fluctuations and dissipation. The arrow points to the TKE for symmetric splitting in the absence of dissipation and fluctuations.

unexpectedly long thin necks, reminiscent of the nuclear shapes obtained in the liquid drop model with a large viscosity [23]. Within that the nuclear shape develops a longer neck as the viscosity increases in the numerical implementation of the hydrodynamical approach of Ref. [23], a result at odds with our findings. Davies *et al.* [23] restricted the nuclear shape to a parametrization using 5 DoF only, while in the present work we have included all shape DoF. These authors also expressed some doubts concerning the accuracy of the calculated inertia and viscosity tensors at large deformations. Shell effects and pairing correlations can be accounted for by a variation of the macroscopic-microscopic formalism [11, 31]. From the known neutron and proton number densities one can construct the single-particle nucleon Hamiltonian, including spin-orbit and pairing interactions, and subsequently determine the corresponding energy density, which can then be used for the next time-step in Eq. (5.37). The full TDDFT description is likely a more efficient solution however.

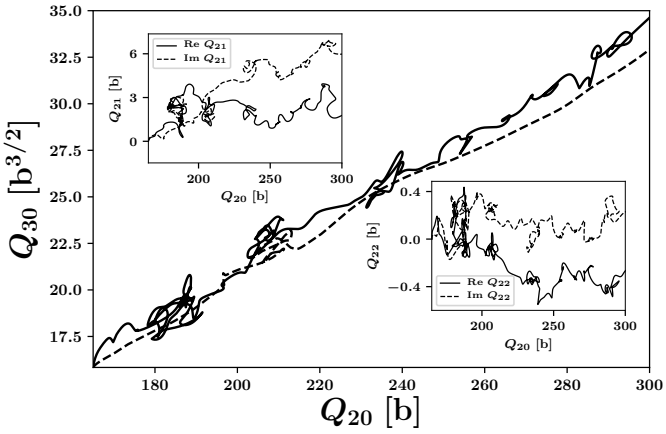

Figure 5.3: In the main panel we show two typical full TDDFT trajectories for ^{240}Pu projected into the $Q_{20} = \langle 2z^2 - x^2 - y^2 \rangle$ and $Q_{30} = \langle (5z^2 - 3r^2)z \rangle$ plane obtained by evolving in time the TDDFT equations without (dashed line) and with (full line) dissipation and fluctuations included, using the SeaLL1 EDF [80]. In the insets we show the fluctuations of the moments $Q_{2m} = \langle z^{2-m}(x + iy)^m \rangle$, for $m = \pm 1, \pm 2$, which vanish in the absence of fluctuations and which break axial symmetry.

5.3.3 TDDFT trajectories

For realistic calculations one has to resort to the full TDDFT description, using the evolution equations Eq. (5.28), with quasi-particle wave functions with spin and isospin DoF, and pairing correlations fully accounted for. In Fig. 5.3 we show a projection onto the planes (Q_{20}, Q_{30}) and (Q_{20}, Q_{2m}) with $m = 1, 2$ of a typical full TDDFT trajectory obtained without dissipation and fluctuations and including dissipation and fluctuations using Eq. (5.28), in the case of induced fission of ^{240}Pu. To this end we integrate in time 442,368 complex coupled nonlinear stochastic partial differential equations on a 3D $24^2 \times 48$ spatial lattice with a lattice constant 1.25 fm, a time step 0.03 fm/c for 130,255 time-steps. Only 6 DoF are illustrated in this figure, even though all collective DoF were allowed to fluctuate. Both trajectories give almost the same fission fragment configurations, though the trajectory including fluctuations and dissipations is more convoluted and costs longer time to scission. We have also performed a considerable number of trajectories with varying strengths of fluctuations (and dissipation)

and obtained the similar results, i.e. the FF properties are not affected by the fluctuations and one cannot get a wide distribution in the mass or TKE in the hydrodynamics approach showed in Fig. 5.2.

The difference between the results obtained by the hydrodynamics method and the full TDDFT method can be understood as follows. In the hydrodynamics model the neutrons and protons are perfect fluids and there is no one-body dissipation, i.e. the collective energy will not transfer to the intrinsic excitations. Therefore, the collective motion can be easily modified by the fluctuation fields, like the Langevin equations solved in the collective space, but with larger DoF. However, in TDDFT the one-body dissipation is highly strong and the collective motion is overdamped, as discussed in the last chapter. Therefore, the fluctuations introduced in the collective flow $\vec{j}(\vec{r},t)$ will be absorbed into the single particle excitations very quickly, which heats up the nucleus and the collective flow energy will return to a small value (< 1 MeV), as shown in Fig. 4.5. The presence of the quantum friction Eq. (5.27) is not very efficient in cooling the system in TDDFT method also because of the smallness of the collective flow energy. In our practice, we usually need a larger strength of dissipation γ to balance the heat up of the system by the same fluctuation strength Γ in TDDFT method than the hydrodynamics approach. The increasing values of γ finally will bring too much high frequency noises brought by the $\vec{\nabla}\cdot\vec{j}$ term into the mean-field potentials, which makes the simulation not stable. Besides, in the hydrodynamics model there are no shell effects, which have a considerable impact on the formation of the fragments. The self-consistent potential energy surface (PES) demonstrates a narrow fission valley where the TDDFT trajectories are trapped (see Fig. 4.2) unless fluctuations are strong enough. In our recent investigations such fission valley is even "deeper" as the temperature of the nucleus increases, which is never taken into account in other Langevin methods where the PES remains the same during the dynamics.

5.4 Summary

Though we do not obtain perfect results in our current study, this extension of the TDDFT formalism still contains several promising features: i) the present formalism is fully quantum; ii) it includes all collective DoF; iii) the evolution is unitary in spite of including explicitly dissipation; iv) all meanfield symmetries are broken during the evolution, as expected for example in a full path-integral description of the dynamics of an interacting many-fermion system, while in Langevin description for example, axial symmetry was never broken; v) upon the inclusion of fluctuations in TDDFT, the fission dynamics remains overdamped, collective kinetic energy remains as small as in their absence, and trajectories become more convoluted and longer in length and time and more random in the collective space; vi) the meanfield adjusts naturally to the changes in the nuclear shape; vii) without fluctuations one obtains only a lower limit of fission times. The formalism described here is applicable to many other situations: dissipative heavy-ion collisions, non-equilibrium phenomena in cold atom physics; dynamics of vortices in neutron star crust, quantum turbulence [167].

Chapter 6

CONCLUSION AND OUTLOOK

In this thesis, we investigate the fission dynamics and its related (static) nuclear structure problems within the SLDA and TDSLDA formalism, which have been validated by observations in a range of static and time-dependent situations in both nuclear and cold atom systems.

The prediction power of TDDFT depends largely on the quality of the NEDF. At present hundreds of NEDFs exist and most of them depend on a large number of fitting parameters [94, 95, 96]. For fission studies, the properties of nucleus in large deformation, like the height of fission barriers (inner and outer) and the excitation energy of the fission isomer are important benchmark quantities for the optimization of NEDFs [95, 168]. In chapter 3, we develop a qualitatively new NEDF named "SeaLL1", which depends on only 7 uncorrelated parameters. SeaLL1 has excellent performances on various properties like nuclear masses, charge radii, shell structure, and generates a reasonable fission pathway of ^{240}Pu.

Following the pioneering work by Bulgac *et al.* [45], which realized the first simulation of induced fission of ^{240}Pu in TDSLDA, in chapter 4 we perform a detailed study of fission dynamics by tuning various input parameters, such as the NEDF, the initial configurations, and the strength of pairing correlations. We find increasing the pairing strength can significantly accelerating the saddle-to-scission process. By choosing different initial configurations on the potential energy surface of SeaLL1 and SkM* EDF, we find a strong focusing effect on the trajectories and obtain almost the same results in the fission fragments (FFs) properties. We conclude that the fission dynamics in saddle-to-scission process is an overdamped, non-adiabatic one. The difference of the potential energy is almost totally transferred into the intrinsic excitation of the nucleus, which results in very small collective flow energies

before scission ($< 1\,\mathrm{MeV}$). The neutron emission rate of FFs is also studied.

To overcome the limitation of TDDFT that the variance of observables are highly suppressed, we introduce a novel scheme, in the spirit of the classical Langevin equations, to include fluctuations and dissipation into the mean-field potentials. We get promising results in the nuclear hydrodynamics simulations of ^{258}Fm fission yields. However, when implementing this scheme in the full TDSLDA calculation, we still cannot produce a wide distribution of FFs properties. Correctly implementing fluctuations and dissipation in the full TDSLDA calculation is still a challenging problem in our future work.

Appendix A

NUMERICAL IMPLEMENTATIONS

The appendices are concerned with the technical details of the codes we developed over the years for the SLDA and TDSLDA simulations presented in the main text.

A.1 Discretization

In both static and dynamics code, all the spatial functions are discretized on a 3D Cartesian lattice of size N_x, N_y, N_z with lattice constants $dx = dy = dz = a$. In each dimension of length $L = Na$, the spatial coordinate x_n and Fourier component k_n are discretized as follows

$$x_n = (-N/2 + n)a, \quad n = 0, \cdots, N-1, \tag{A.1}$$

$$k_n = \begin{cases} 2n\pi/L, & n = 0, \cdots, N/2-1 \\ (2n-N)\pi/L, & n = N/2, \cdots, N-1 \end{cases}, \tag{A.2}$$

consistent with boundary conditions. When discretized in the (3D) lattice, both wavefunctions and Hamiltonian are represented in the discrete variable representation (DVR) [132], which is sometimes referred to the Lagrange-mesh method [169] in numerical analysis. In one dimension, the functions are represented as

$$\psi(x) = \sum_k a\psi(x_k) f_k(x), \tag{A.3}$$

where the DVR basis states f_ks form an orthonormal set

$$\begin{aligned} f_k(x_l) &= \sum_{n=-N/2}^{N/2-1} \frac{1}{L} \exp[ik_n(x_l - x_k)] \\ &= \begin{cases} \frac{\sin \pi(k-l)}{Na} \cot \frac{\pi(k-l)}{N} = 0 & k \neq l, \\ 1/a & k = l, \end{cases} \end{aligned} \tag{A.4a}$$

and

$$\langle f_k|f_l\rangle = \sum_n a f_k(x_n) f_l(x_n) = \delta_{kl}. \tag{A.4b}$$

In the static SLDA calculation, one needs to diagonalize the matrix of hamiltonian in Eq. (2.24) in each self-consistent iteration. All the local potential matrix elements have a simple diagonal representation

$$\langle f_k|U|f_l\rangle = \sum a f_k^*(x_n) U(x_n) f_l(x_n) = U(x_k)\delta_{kl}. \tag{A.5}$$

The non-diagonal matrix elements source from the spatial first ∂_x and second derivative ∂_{xx} in the kinetic and spin-orbit terms, which in DVR basis can be represented as

$$(\partial_x)_{nm} = \frac{\pi}{Na}(-1)^{n-m}(1-\delta_{nm})\cot\left(\frac{\pi(n-m)}{N}\right), \tag{A.6a}$$

$$(\partial_{xx})_{nm} = \frac{\pi^2}{2N^2a^2}\frac{(-1)^{(n-m)}(\delta_{nm}-1)}{\sin^2\frac{\pi(n-m)}{N}} - \frac{\pi^2}{3a^2}\left(1+\frac{2}{N^2}\right)\delta_{nm}. \tag{A.6b}$$

In the time-dependent calculation, the Hamiltonian matrix is not explicitly evaluated. Instead, we directly compute the matrix-vector products $H\psi$ in each time-step. Besides the trivial products of the local potentials and wavefunctions, the most time-consuming part is the calculations of gradient and lapaclean of wavefunctions. In order to make this operation as efficeint as possible, we use the fast Fourier transforms (FFT)

$$\mathcal{F}[f(x)] : \tilde{f}(k_n) = \sum_{l=0}^{N-1} \exp(-ik_n x_l) f(x_l), \tag{A.7a}$$

$$\mathcal{F}^{-1}[\tilde{f}(k)] : f(x_l) = \frac{1}{N}\sum_{n=0}^{N-1} \exp(ik_n x_l)\tilde{f}(k_n), \tag{A.7b}$$

with $\mathcal{F}$ and $\mathcal{F}^{-1}$ the direct and inverse Fourier transforms. Hence, the application of the derivative operator m times is efficiently evaluated as follows

$$\mathcal{D}^{(m)} f(x) = \mathcal{F}^{-1}\left[(ik)^m \tilde{f}(k)\right]. \tag{A.8}$$

For odd derivatives there is a loss of symmetry that can induce small imaginary part into derivatives that should be purely real. In order to avoid issues, we set $\tilde{f}(k_{N/2}) = 0$ [170].

For better numerical accuracy, we avoid computing first-order derivatives if possible. For example, the kinetic energy term in Eq. (2.25) can be rewritten as

$$-\vec{\nabla}\cdot\frac{\hbar^2}{2m^*(\vec{r})}\vec{\nabla}v(\vec{r}) = -\frac{1}{2}\left[\frac{\hbar^2}{2m^*(\vec{r})}\nabla^2 v(\vec{r}) + \nabla^2\left(\frac{\hbar^2}{2m^*(\vec{r})}v(\vec{r})\right) - \left(\nabla^2\frac{\hbar^2}{2m^*(\vec{r})}\right)v(\vec{r})\right], \tag{A.9}$$

which corresponds to a symmetric matrix representation T in the static solver as

$$T_{nm} = \left(-\vec{\nabla}\cdot\frac{\hbar^2}{2m^*(\vec{r})}\vec{\nabla}\right)_{nm} = -\frac{1}{2}(\nabla^2)_{nm}\left(\frac{\hbar^2}{2m_n^*} + \frac{\hbar^2}{2m_m^*}\right) + \frac{1}{2}\left(\nabla^2\frac{\hbar^2}{2m^*}\right)_n\delta_{nm} \tag{A.10}$$

where the laplacian operator ∇^2 is a symmetric matrix as in Eq. (A.6b).

In our practice, we also find that better accuracy can be achieved when a special symmetrization is performed for the spin-orbit term

$$\frac{1}{i}\vec{W}(\vec{r})\cdot\left(\vec{\nabla}\times\vec{\sigma}\right) = \frac{1}{2i}\left[\vec{W}(\vec{r})\cdot\left(\vec{\nabla}\times\vec{\sigma}\right) + \vec{\nabla}\cdot\left(\vec{\sigma}\times\vec{W}(\vec{r})\right)\right]. \tag{A.11}$$

A.2 The Coulomb potential

To calculate the Coulomb potential $V_c(\vec{r})$ generated by the charge(proton) density $n_p(\vec{r})$, we actually solve the Poisson equation

$$\vec{\nabla}^2\Phi(\vec{r}) = 4\pi e^2 n(\vec{r}) \tag{A.12a}$$

$$\Phi(\vec{r}) = \int d^3\vec{r}'\frac{e^2 n(\vec{r})}{|\vec{r}-\vec{r}'|} \tag{A.12b}$$

In numerical implementation [79, 45, 58, 171, 114] the convolution Eq. (A.12b) is solved by FFT $\mathcal{F}$ via

$$\Phi(\vec{r}) = \int\frac{d^3k}{(2\pi)^3}\frac{4\pi e^2\tilde{n}(\vec{k})}{k^2}\exp(i\vec{k}\cdot\vec{r}) = e^2\mathcal{F}^{-1}[\tilde{n}(\vec{k})\tilde{f}(\vec{k})], \tag{A.13}$$

$$\tilde{n}(\vec{k}) = \mathcal{F}[n(\vec{r})] \tag{A.14}$$

To avoid the infrared divergence for $\vec{k} \to 0$ we use a truncated kernel $\tilde{f}(k)$ [172], considering a modified Coulomb potential

$$f(r) = \begin{cases} 1/r, & \text{for } r < D \\ 0, & \text{otherwise} \end{cases} = \int \frac{d^3k}{(2\pi)^3} \tilde{f}(\vec{k}), \tag{A.15}$$

$$\tilde{f}(\vec{k}) = \begin{cases} 4\pi e^2 \left[1 - \cos(|\vec{k}|D)\right] / k^2, & |\vec{k}| \neq 0 \\ 2\pi e^2 D, & |\vec{k}| = 0 \end{cases} . \tag{A.16}$$

In a cubic box $L_x = L_y = L_z = L$ if we choose $D = \sqrt{3}L$ we can compute the Coulomb potential due to the charge distribution inside the box, eliminating any contribution from the neighboring cells. In a rectangular 3D box, we select L to be the longest dimension among L_x, L_y, L_z and the Eq. (A.13) is realized by the summation

$$\Phi(\vec{r}) = \frac{1}{27N^3} \sum_{\vec{k} \in (3L)^3} e^2 \tilde{n}(\vec{k}) \tilde{f}(\vec{k}) \exp(i\vec{k} \cdot \vec{r}). \tag{A.17}$$

with the number of floating point operations in is $27N^3 \log(27N^3)$ where N is the lattice number in the longest dimension. To super-deformed system this calculation will be considerably expensive.

Because of the summation over $27N^3$ points, in the case when one dimension is much larger than the other two, as we chose often in the case of fission dynamics, the calculation becomes considerably expensive. In such a case, the computational cost can be reduced by the following method. Consider a function $f(x)$ on the interval $(0, L)$ which we extend to the interval $(-L, 2L)$ by adding zeros outside the main interval and the new function called $g(x)$

$$g(x) = \begin{cases} f(x), & \text{if } 0 \leq x \leq L \\ 0, & \text{otherwise.} \end{cases} \tag{A.18}$$

Apart from normalization one can define two Fourier transforms, one on the interval $(0, L)$ the other on the interval $(-L, 2L)$,discretized with the same lattice constant Δx. The discrete Fourier transform on the interval $(0, L)$ will have Fourier components at momenta

$$k_i = -\frac{\pi}{\Delta x} + \frac{2\pi i}{L} \text{ for } i = 0, \ldots N-1, \tag{A.19}$$

while the other one will have components at momenta

$$\tilde{k}_i = -\frac{\pi}{\Delta x} + \frac{2\pi i}{3L} \text{ for } i = 0, \ldots 3N-1, \tag{A.20}$$

hence $\tilde{k}_{3i} = k_i$, for $= 0, \ldots N-1$. Indeed, N of the momenta on the $3N$ discretization are the same with the momenta on the N discretization, the other $2N$ momenta being defined as $k_i + 2\pi/(3L)$ and $k_i + 4\pi/(3L)$, with $i = 0, \ldots N-1$. For the arbitrary function $f(x)$, we can perform the following three Fourier transforms:

$$h_n = \sum_l f(x_l) \exp(-ik_n x_l) \tag{A.21a}$$

$$h_{n+1/3} = \sum_l f(x_l) \exp\left(-i\frac{2\pi}{3L}x_l\right) \exp(-ik_n x_l) \tag{A.21b}$$

$$h_{n+2/3} = \sum_l f(x_l) \exp\left(-i\frac{4\pi}{3L}x_l\right) \exp(-ik_n x_l). \tag{A.21c}$$

In terms of h_n, $h_{n+1/3}$, and $h_{n+2/3}$, one can prove the following relationship for function $g(x)$ defined in Eq. (A.18)

$$\begin{aligned} g(x_l) = \frac{1}{3}\Bigg[&\sum_n h_n \exp(ik_n x_l) + \exp\left(i\frac{2\pi}{3L}x_l\right) \sum_n h_{n+1/3} \exp(ik_n x_l) \\ &+ \exp\left(i\frac{4\pi}{3L}x_l\right) \sum_n h_{n+2/3} \exp(ik_n x_l)\Bigg], \end{aligned} \tag{A.22}$$

where the 1/3 factor comes from the different normalizations of the discrete Fourier transforms using discretizations with N and $3N$ points, respectively. Hence, instead of performing one forward and one backward Fourier transforms on the interval $(-L, 2L)$, one would perform three forward and three backward Fourier transforms on the interval $(0, L)$. In 3D this will mean that instead of performing $\mathcal{O}(27N^3 \log 27N^3)$ operations one performs only $\mathcal{O}(27N^3 \log N^3)$ operations, which produces noticeable efficiency, especially because the Coulomb contribution is a bottle neck in the computation. Moreover one can do all these

Fourier transforms in parallel. The complete form of such decomposition of Eq. (A.17) is

$$\begin{aligned}\Phi(\vec{r}) =& \frac{1}{27N^3}\sum_{k,l,m=0}^{2}\left[\sum_{k\in L^3} e^2\tilde{n}_{klm}(\vec{k})\tilde{f}\left(\vec{k}+\left(k\frac{2\pi}{3L},l\frac{2\pi}{3L},m\frac{2\pi}{3L}\right)\right)\exp(i\vec{k}\cdot\vec{r})\right] \\ &\times\exp\left(i\left(k\frac{2\pi}{3L}x+l\frac{2\pi}{3L}y+m\frac{2\pi}{3L}z\right)\right)\end{aligned} \tag{A.23a}$$

where

$$\tilde{n}_{klm}(\vec{k}) = \sum_{\vec{r}\in L^3} n(x,y,z)\exp\left(-i\left(k\frac{2\pi}{L}x+l\frac{2\pi}{L}y+m\frac{2\pi}{L}z\right)\right)\exp(-i\vec{k}\cdot\vec{r}). \tag{A.23b}$$

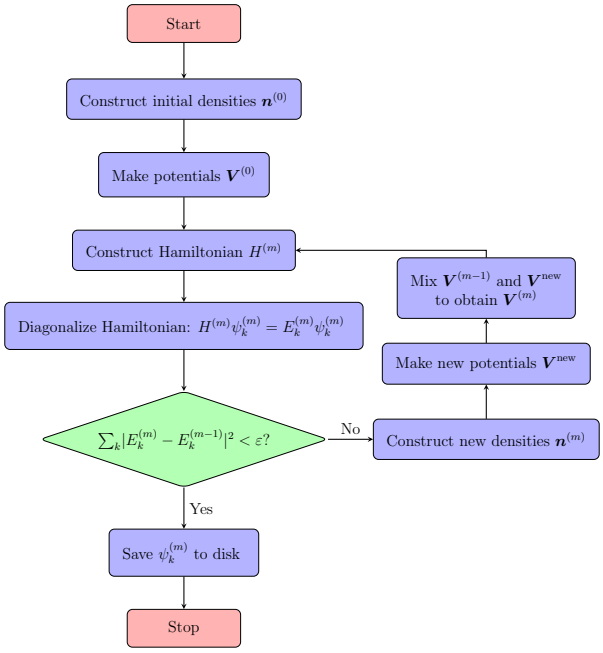

Figure A.1: Flowchart of static SLDA solver.

A.3 Static SLDA

A.3.1 Self-consistent iterations

The static solution is obtained by solving the SLDA equation Eq. (2.24) self-consistently. The static solver starts from a set of initial local densities denoted generically by $\boldsymbol{n}^{(0)}$. Two

options are provided for starting the calculations:

- the initial guess of local densities $\boldsymbol{n}^{(0)}$ are constructed from periodic 3D Gaussian-like functions with appropriate saturation and surface properties for the desired nucleus;

- the inital densities $\boldsymbol{n}^{(0)}$ are read from the disk; in this case, previously calculated densties with this solver or generated with other solvers can be used to continue the calculation on the lattice, or to produce the initial conditions by performing one diagonalization.

The various local potentials $\boldsymbol{V}^{(0)}$ and the resulting Hamiltonian matrix are generated using densties $\boldsymbol{n}^{(0)}$. In self-consistent iteration m, the qpwfs $\psi_k^{(m)}$ and their corresponding quasiparticle energies $E_k^{(m)}$ are obtained by a direct diagonalization of the Hamiltonian using the `pzheevd()` function included in the ScaLapack library. Next, the new local densities are constructed from the qpwfs using **??** and the new potentials $\boldsymbol{V}^{\text{new}}$ are generated as well . The chemical potential μ should also be updated for the convergence of the particle number. In this code we use the relation between the change in chemical potential and the change of particle number from the Thomas-Fermi (TF) approximation (separately for neutrons and protons)

$$\delta\mu = \frac{2}{3} E_F \frac{\delta N}{N} \tag{A.24}$$

where $E_F = \hbar^2 k_F^2 / 2m \approx 35$ MeV is the Fermi energy of the infinite symmetric nuclear matter. Thus the new chemical potential is updated like

$$\mu^{\text{new}} = \mu^{(m-1)} - \frac{2}{3} E_F (N^{(m)} - N_0)/N_0, \tag{A.25}$$

where N_0 is the desired particle number.

To reach convergence, the new potentials and chemical potentials are mixed with the ones in the last iteration by a linear combination:

$$\boldsymbol{V}^{(m)} = (1-\alpha)\boldsymbol{V}^{(m-1)} + \alpha \boldsymbol{V}^{\text{new}} \tag{A.26a}$$

$$\mu^{(m)} = (1-\alpha)\mu^{(m-1)} + \alpha \mu^{\text{new}} \tag{A.26b}$$

with a constant mixing factor α. As an additional option, another mixing procedure is available; it is based on the Broyden method, see Ref. [173] for details. However, we advise caution in using this option, as it often deviates from finding the solution. Note that we concurrently perform interations for proton and neutron density, by splitting the MPI world into two equal groups.

The convergence criteria of the self-consistent iterations is that the norm of the quasi-particle energy difference is less than the tolerance ε:

$$\sum_k |E_k^{(m)} - E_k^{(m-1)}|^2 < \varepsilon.$$

When a converged solution is obtained, the qpwfs are written into files to be used by the time-dependent code.

A.3.2 Constraints

In practical calculations, one often requires a HFB minimum in certain configurations, for example, multiple mass moments defined in Eq. (2.57) to have fixed values. Then in a constrained HFB calculation, one needs to add a constraint term into the s.p. Hamiltonian in Eq. (2.25)

$$h' = h + \sum_i \lambda_i (\hat{Q}_i - Q_i^{(0)}), \tag{A.27}$$

where $\hat{Q}_i$'s are different constraint operators, λ_is are their corresponding Lagrange multipilers, and $Q_i^{(0)}$ are the expectation values of operators $\hat{Q}_i$'s input by the user. Between iterations, for a given constraint $\hat{Q}$, the Lagrange multiplier λ is updated in the *augmented Lagrangian method* (ALM) [174]

$$\lambda_i^{k+1} = \lambda_i^k + 2c_i(q_i - Q_i^{(0)}), \tag{A.28}$$

where q_i is the expectation value of $\hat{Q}_i$ in the iteration k. The coefficients c_i should be small enough to guarantee the stability of the self-consistent iterations. In the static code, we

implemented the constraints of the center of mass positions of the nucleus $\vec{r}_{\rm cm}$ and quadruple mass moment Q_{20} with additive operators $\{\hat{x}, \hat{y}, \hat{z}, \hat{Q}_{20}\}$ associated with the Lagrange multipliers $\{\lambda_x, \lambda_y, \lambda_z, \lambda_{q2}\}$.

A.4 TDSLDA

A.4.1 Time evolution

A common approach to solving the time-dependent mean-field equations like TDHF is the series expansion method [38]. In this method, the PDE 2.39 can be formally rewritten into an integral equation as

$$\psi_k(t + \Delta t) = \hat{U}(t, t + \Delta t)\psi_k(t), \tag{A.29a}$$

where $\psi_k(t)$ denotes the qpwf $[u_{k\uparrow}(\vec{r}, t), u_{k\downarrow}(\vec{r}, t), v_{k\uparrow}(\vec{r}, t), v_{k\downarrow}(\vec{r}, t)]^T$. The evolution operator $\hat{U}$ is defined as

$$\hat{U}(t, t + \Delta t) = \mathcal{T} \exp\left(-\frac{i}{\hbar}\int_t^{t+\Delta t} \hat{H}(t')dt'\right). \tag{A.29b}$$

where $\mathcal{T}$ the time-ordering operation and $\hat{H}(t)$ is the Hamiltonian at time t. For higher accuracy, we have implemented a predictor-corrector method as follows:

(1) At time t, we perform a predictor step with the Hamiltonian $H(t)$ constructed from the densties $\boldsymbol{n}(t)$ computed using the qpwf $\psi_k(t)$

$$\psi_{\rm pre} = \exp\left(-\frac{i}{\hbar}\hat{H}(t)\Delta t\right)\psi_k(t). \tag{A.30}$$

(2) From the trial solution $\psi_{\rm pred}$ we obtain a set of predictor densities denoted as $\boldsymbol{n}_{\rm pred}$, that are used to compute a set of corrector densites $\boldsymbol{n}_{\rm cor} = (\boldsymbol{n}_{\rm pre} + \boldsymbol{n}(t))/2$. The corrector Hamiltonian $\hat{H}_{\rm cor}$ is then constructed with densities $\boldsymbol{n}_{\rm cor}$, and if Δt is small enough, $\hat{H}_{\rm cor}$ is a good approximation to the self-consistent Hamiltonian at time $t + \Delta t/2$.

(3) Finally, the qpwf at time $t + \Delta t$ is calculated as

$$\psi_k(t + \Delta t) = \exp\left(-\frac{i}{\hbar}\hat{H}_{\rm cor}\Delta t\right)\psi_k(t). \tag{A.31}$$

In our numerical implementation, the time-evolution operator $\exp\left(-\frac{i}{\hbar}\hat{H}\Delta t\right)$ is replaced with the series expansion

$$\exp\left(-\frac{i}{\hbar}\hat{H}\Delta t\right) = \sum_n \frac{(-i)^n}{\hbar^n n!}\hat{H}^n \Delta t^n, \tag{A.32}$$

and in practice we find an expansion to order $n = 4$ is enough for a good accuracy, with the error of order $\mathcal{O}(\Delta t^5)$. Within an expansion approach, we need to compute $4 \times 2 = 8$ times matrix-vector (MV) products $H\psi$ in each time step, which is the most time-consuming part of the code. The ABM method [175] provides an alternative to the series expansion method with the same accuracy, but only 2 MV products in each time step. For a PDE that can be generically written as $y' = f(y)$, in the 5th order predictor-modifier-corrector ABM method, the y_{n+1} solution is constructed from y_n as follows:

$$p_{n+1} = \frac{y_n + y_{n-1}}{2} + \frac{h}{48}\left(119y'_n - 99y'_{n-1} + 69y'_{n-2} - 17y'_{n-3}\right) + \frac{161}{480}h^5 y^{(5)} \tag{A.33a}$$

$$m_{n+1} = p_{n+1} - \frac{161}{170}(p_n - c_n) + \frac{923}{2880}h^6 y^{(6)} \tag{A.33b}$$

$$c_{n+1} = \frac{y_n + y_{n-1}}{2} + \frac{h}{48}\left(17m'_{n+1} + 51y'_n + 3y'_{n-1} + y'_{n-2}\right) - \frac{9}{480}h^5 y^{(5)} \tag{A.33c}$$

$$y_{n+1} = c_{n+1} + \frac{9}{170}(p_{n+1} - c_{n+1}) - \frac{43}{2880}h^6 y^{(6)} \tag{A.33d}$$

where p, m, c denote the predictor, modifier and corrector, and a prime marks the derivative with respect to time. The drawback of the ABM method is that it cannot start itself from step 0 because the time derivatives y' at time steps $-1, -2, -3$ and y_{-1} are unknown, unless the starting state is a stationary solution, and in that case $y'_{-3} = y'_{-2} = y'_{-1} = 0$ and $y_{-1} = y_0$. However, the series expansion method can serve as a starting procedure for up to four steps during which the time derivatives of the wavefunctions are calculated and stored in each step to be used for the ABM method.

When computing the time evolution of the qpwfs via Eq. (2.39), an irrelevant phase factor

$$\exp\left[-\frac{i}{\hbar}\int_0^t \langle\psi_k(t')|\hat{H}(t')|\psi_k(t')\rangle dt'\right] \tag{A.34}$$

is introduced. This factor induces oscillations in time and downgrades the numerical accuracy and stability. In our implementation this trivial phase is removed removing the instantaneous quasiparticle energy,

$$i\hbar\dot{\psi}_k(t) = (\hat{H} - \eta_k)\psi_k(t) \tag{A.35}$$

with

$$\eta_k(t) = \langle\psi_k(t)|\hat{H}|\psi_k(t)\rangle. \tag{A.36}$$

While not necessary as the evolution is unitary, at the end of each time step we also normalize each qpwf ψ_k to 1. This insures that the numerical roundoff errors are kept to a minimum.

Appendix B

PARALLELIZATION AND GPU ACCELERATION

B.1 Static Code

In static SLDA calculation one needs to diagonalize the $N \times N$ Hamiltonian matrix (for each isospin) in Eq. (2.24) with $N = 4N_xN_yN_z$, which could be $10^5 \sim 10^6$ in practical calculations. Therefore the total matrix could cost a memory of $10^2 \sim 10^3$ giga bytes, which exceeds the maximum memory of single CPU. In the static code, we use the message passing interface (MPI) library to realize the parallelization. For totally `np` processes of index `iam` each, we divide them into two MPI groups evenly for two isospins respectively. In each MPI group, the processes are reformulated as a 2D grid of dimension (p,q). The elements of the full Hamiltonian matrix will be split into different processes. The map between the global index of element `(gi,gj)` in the full matrix and the local index `(li,lj)` in each processes follows the 2D *Block-Cylic Distribution* [176].

In this distribution, for a general matrix of dimension `(ma, na)`, the rows and columns are split into different blocks of dimension `(mb, nb)`. For each element of global index `(gi, gj)`, it will fall into one of the process grids of index `(ip, iq)` as

```
ip = (gi / mb) mod p
iq = (gj / nb) mod q
```

Then the local index `(li, lj)` in process `(ip, iq)` is mapped as

```
li = (gi / mb) / p * mb + (gi mod mb)
lj = (gj / nb) / q * nb + (gj mod nb)
```

and inversely

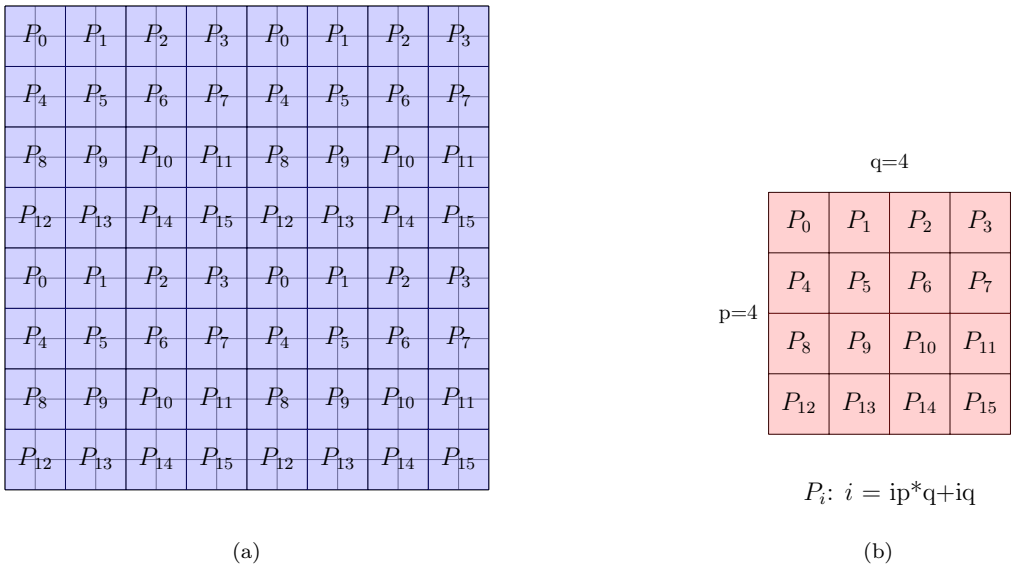

Figure B.1: Distribution of the elements of a 16×16 matrix on 16 processes. Block size `mb=nb=2`.

```
gi = ip * mb  + (li / mb) * p * mb + li mod mb
gj = iq * nb  + (lj / nb) * q * nb + lj mod nb
```

In Fig. B.1a, we show the distribution of a 16×16 matrix on 16 processes. Each process is labeled as $P_i, i = 0, \cdots 15$. The size of the block is `mb=nb=2`. The 4×4 grid of processes is also shown in Fig. B.1b.

The diagonalization of the matrix is realized by the `pzheevd()` routine in the ScaLapack library [177]. After the diagonalization, the resulting eigenvectors (qpwfs) are distributed in different processes as a matrix in the same way of the hamiltonian. The rows of the matrix represent the $4N_{xyz}$ components of each qpwfs while the columns represent the indices of qpwfs. To calculate various local densities, one needs to do summations of qpwfs as shown in Eq. (2.17), which is realized by a `for` loop over the column indices `j` of the eigenvector matrix. Inside the loop, for a given qpwf (column `j=j0`), one fills its segments in different processes by collecting the elements which have global column indices `gj == j0`. Then all the segments are combined into the full column by a global reduction inside each MPI Group

using the `MPI_AllReduce()` routine. The local densities calculated in one MPI group will be shared with the other group for updating the mean-field potentials and constructing the new hamiltonian matrix. The exchange of the densities are realized by point-point communications between MPI groups using the `MPI_Send()` and `MPI_Recv()` routines.

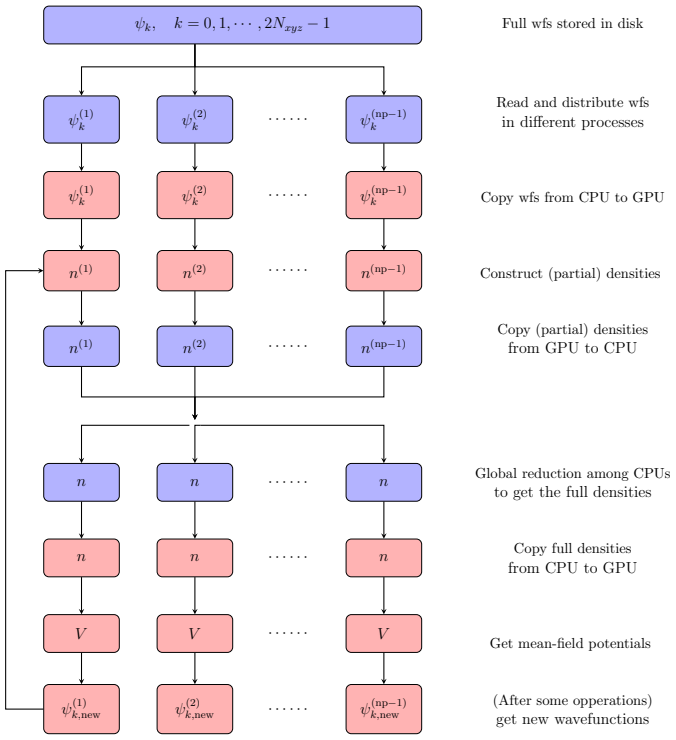

Figure B.2: Parallelization structure of the TDSLDA code.

B.2 Time-dependent Code

B.2.1 CPU-GPU hybrid structure

The TD code has a more straightforward parallelization structure than the static code and takes advantage of the GPU acceleration, as shown in Fig. B.2. At the beginning, the whole qpwfs stored in the disk are read and distributed in different (CPU) processes uniformly, i.e. each process has certain number of qpwfs with full components. Then the qpwfs will be

copied to the paired GPU device in each process, and the partial local densities are calculated as Eq. (2.37a). To obtain the full densities, the partial densities are firstly transferred from GPU to CPU, then a reduction operation is performed by the `MPI_Allreduce` routine to reduce and broadcast the full densities to all (CPU) processes. Finally, the full densities are transferred back to GPUs to construct the mean-field potentials for use in the evolution of qpwfs in the next time step.

B.2.2 FFT in batch

The most time-consuming calculation is the spatial derivatives of wavefunctions with FFTs. In this code we use CuFFT, the FFT library for GPUs to perform such operations. To take full advantage of the GPU acceleration, we do FFTs (and inverse FFTs) for a batch of functions simultaneously. In the code, the wavefunctions are stored in a 1-D array of size `4*nxyz*nwfip*sizeof(cufftDoubleComplex)` . Then the size of CuFFT buffer is `batch*nxyz*sizeof(cufftDoubleComplex)`. Currently the value of `batch` is set to 8. But as the development of the GPU hardware this number could be larger to gain optimized performance.

B.2.3 Checkpoint and restart

During the evolution, for every `time_cp` (in fm/c) the wavefunctions are copied from GPUs to CPUs and then saved to disk for checkpoint. The same checkpoint procedure will be performed after the finalization of the program as well. During the checkpoint, only the latest wavefunctions (for neutron and proton) are saved and the program can restart from this one directly with the starting procedure described in appendix A.4.

Appendix C

PERFORMANCES OF THE CODES

The performance of the static code has been illustrated in Ref. [171] and then we will not discuss it in the thesis because it just serves as a utility code for the TD code and computational cost of the former one is much smaller than the latter one for large scale simulations. Our TD code has been benchmarked on Titan and Summit at OLCF, Oak Ridge, USA and Piz Daint in Lugano, Switzerland. In Table C.1 we list the time cost of our code on different supercomputers. As a measure we have used the required computation time per lattice point of one of the components of a single qpwf, when performing a complete calculation of all the qpwfs

$$\text{Cost} = \frac{(\#\text{ CU}) \times (\text{wall-time})}{(\#\text{ time-steps}) \times (\#\text{ PDEs}) \times (\#\text{ lattice-points})}, \tag{C.1}$$

where # CU stands for the number of computing units, either GPUs in case of the TDSLDA code or CPUs in case of other CPU codes in the market for TDHF. The difference of cost is mainly due to the difference of GPU hardwares on these computers. The NVIDIA Tesla P100 GPU on Piz-Daint is almost 3x faster than the NVIDIA Tesla K20 GPU on Titan. The newest NVIDIA V100 GPU on Summit is 30% faster than P100.

The scaling properties of different sections in the code are also studied. Here we divide the runtime of the TDSLDA code into three parts:

- ABM: the time cost on the GPU kernels in `adams_bashforth_pm_gpu()`, `adams_bashforth_cy_gpu()`, and `adams_bashforth_dfdt_gpu()`.

- Density: the time cost on the GPU kernels in `compute_densities_gpu()`, which includes the calculation of the gradients and laplaceans of qpwfs and partial local densities.

Code	CUs	Computer	PDEs	Lattice	Cost (sec.)
TDSLDA	514	Titan	442,368	$24^2 \times 48$	4.35×10^{-8}
TDSLDA	240	Piz Daint	442,368	$24^2 \times 48$	1.61×10^{-8}
TDSLDA-opt	240	Piz Daint	442,368	$24^2 \times 48$	1.23×10^{-8}
TDSLDA	240	Summit	442,368	$24^2 \times 48$	1.12×10^{-8}
TDSLDA-opt	240	Summit	442,368	$24^2 \times 48$	7.18×10^{-9}

Table C.1: Comparison between different existing codes for performing TDDFT calculations on a variety of architectures. The TDSLDA code demonstrates an almost perfect strong scaling on Piz Daint (Lugano) and Summit (Oak Ridge), where further significant optimizations are likely. TDSLDA-opt is an optimized version of our GPU code which reduces the number of calls of CPU-based routines. TDSLDA-simp is a simplified and un-optimized version of our GPU code, performing the same type of calculations as codes [38, 178] used in literature for TDHF+TDBCS simulations.

- Communications: the time cost on the communications between CPU and GPU (`cudaMemcpy()`), CPU and CPU (`MPI_Allreduce()`).

In practice we made a few test runs of TDSLDA code for the same problem described in Table C.1 up to 400 time steps, with different number of nodes on Summit. In each run, we measure the wall-time (in seconds) of each section with internal clock and calculate their corresponding node hours on Summit as node hrs. = wall-time $\times$ # nodes / 3600. As shown in Fig. C.1, the GPU kernels in ABM and Density cost almost constant node hours as the increase of nodes, which demonstrates a good strong scaling property. The Comm. section roughly costs constant or even more wall-time as the increase of nodes, and contributes the increased node hours. In Fig. C.2 we plot the speed-up of the wall-time cost on GPU kernels, i.e. excluding the communication time from the total runtime, and compare with the speed-up if the scaling property is perfect. It's shown that the GPU kernels have perfect scaling properties for number of GPUs less than 720. Beyond this number, the workload on each GPU is too small and the threads in GPUs are not utilized completely.

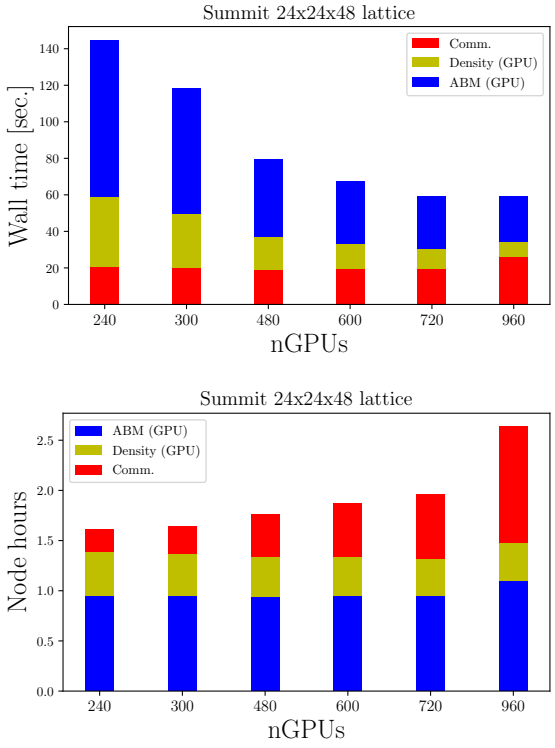

Figure C.1: The strong scaling capability of the TDSLDA codes on Summit.

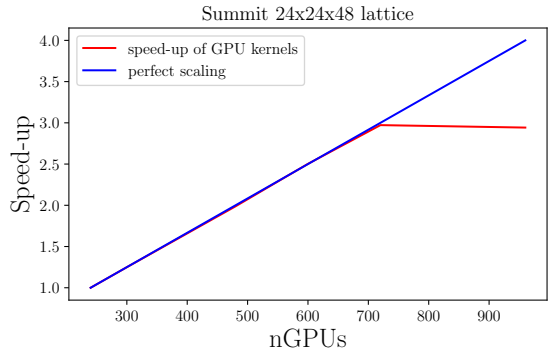

Figure C.2: The speed-up of GPU kernels on Summit

We also compared the efficiency of our code with that of the-state-of-the-art codes in literature for TDHF calculations [38, 178], see Table C.2. The TDHF Sky3D code [38] evolves at most $\approx 1,000$ PDEs for the collision of two heavy-ions treating pairing correlations within the BCS approximation. The wall-time using a number of CPUs equal to the number of GPUs in our approach is almost 100x longer for similarly sized problems. We attribute the superior performance of the TDSLDA solver to the use of a more efficient while very accurate time-integration algorithm, as well as to the use of GPUs. The use of highly efficient and precise FFT for the computation of spatial derivatives could also be a factor. Since in our calculations we have to manipulate large amounts of data, we have taken advantage of fast I/O methods and fast algorithms to exchange data between computing nodes.

Code	CUs	Computer	PDEs	Lattice	Cost (sec.)
TDSLDA-simp	2	Titan	684	$20^2 \times 60$	7.55×10^{-8}
Sky3D [38]	128	Titan	1,024	$18^2 \times 30$	3.86×10^{-6}
U&S [178]	16	Linux cluster	714	$40^2 \times 70$	8.72×10^{-5}

Table C.2: Comparison between different existing codes for performing TDDFT calculations on a variety of architectures. The TDSLDA code demonstrates an almost perfect strong scaling on Piz Daint (Lugano) and Summit (Oak Ridge), where further significant optimizations are likely. TDSLDA-opt is an optimized version of our GPU code which reduces the number of calls of CPU-based routines. TDSLDA-simp is a simplified and un-optimized version of our GPU code, performing the same type of calculations as codes [38, 178] used in literature for TDHF+TDBCS simulations.

BIBLIOGRAPHY

[1] O. Hahn and F. Strassmann. Über den nachweis und das verhalten der bei der bestrahlung des urans mittels neutronen entstehenden erdalkalimetalle. *Naturwissenschaften*, 27(1):11–15, Jan 1939.

[2] Lise Meitner and O. R. Frisch. Disintegration of uranium by neutrons: a new type of nuclear reaction. *Nature*, 143:239 EP –, 02 1939.

[3] Niels Bohr and John Archibald Wheeler. The mechanism of nuclear fission. *Phys. Rev.*, 56:426–450, Sep 1939.

[4] Aage Bohr and Ben R. Mottelson. *Nuclear Structure*, volume I. Benjamin Inc., New York, 1969.

[5] F. Barranco, G.F. Bertsch, R.A. Broglia, and E. Vigezzi. Large-amplitude motion in superfluid fermi droplets. *Nuclear Physics A*, 512(2):253 – 274, 1990.

[6] Maria Goeppert Mayer. On closed shells in nuclei. ii. *Phys. Rev.*, 75:1969–1970, Jun 1949.

[7] Otto Haxel, J. Hans D. Jensen, and Hans E. Suess. On the "magic numbers" in nuclear structure. *Phys. Rev.*, 75:1766–1766, Jun 1949.

[8] M.G. Mayer and J.H.D. Jensen. *Elementary Theory of Nuclear Shell Structure*. Literary Licensing, LLC, 2013.

[9] V.M. Strutinsky. Shell effects in nuclear masses and deformation energies. *Nuclear Physics A*, 95(2):420 – 442, 1967.

[10] V.M. Strutinsky. "shells" in deformed nuclei. *Nuclear Physics A*, 122(1):1 – 33, 1968.

[11] M. Brack, Jens Damgaard, A. S. Jensen, H. C. Pauli, V. M. Strutinsky, and Wong C. Y. Funny hills: The shell-correction approach to nuclear shell effects and its applications to the fission process. *Rev. Mod. Phys.*, 44:320–405, Apr 1972.

[12] S. Bjørnholm and J. E. Lynn. The double-humped fission barrier. *Rev. Mod. Phys.*, 52:725–931, Oct 1980.

[13] Aurel Bulgac and Yongle Yu. Local density approximation for pairing correlations in nuclei. *arXiv:nucl-th/0109083*.

[14] David Lawrence Hill and John Archibald Wheeler. Nuclear constitution and the interpretation of fission phenomena. *Phys. Rev.*, 89:1102–1145, Mar 1953.

[15] J.J. Sakurai and J.J. Napolitano. *Modern Quantum Mechanics*. Pearson Education, 2014.

[16] Leon N. Cooper. Bound electron pairs in a degenerate fermi gas. *Phys. Rev.*, 104:1189–1190, Nov 1956.

[17] J. Bardeen, L. N. Cooper, and J. R. Schrieffer. Theory of superconductivity. *Phys. Rev.*, 108:1175–1204, Dec 1957.

[18] L.D. Landau and E.M. Lifshitz. *Quantum Mechanics: Non-Relativistic Theory*. Course of Theoretical Physics. Elsevier Science, 1981.

[19] G. Bertsch. The nuclear density of states in the space of nuclear shapes. *Physics Letters B*, 95(2):157 – 159, 1980.

[20] George F. Bertsch and Aurel Bulgac. Comment on "spontaneous fission: A kinetic approach". *Phys. Rev. Lett.*, 79:3539–3539, Nov 1997.

[21] John W. Negele. Microscopic theory of fission dynamics. *Nuclear Physics A*, 502:371 – 386, 1989.

[22] N Schunck and L M Robledo. Microscopic theory of nuclear fission: a review. *Reports on Progress in Physics*, 79(11):116301, 2016.

[23] K. T. R. Davies, A. J. Sierk, and J. R. Nix. Effect of viscosity on the dynamics of fission. *Phys. Rev. C*, 13:2385–2403, Jun 1976.

[24] Jørgen Randrup and Peter Möller. Brownian shape motion on five-dimensional potential-energy surfaces:nuclear fission-fragment mass distributions. *Phys. Rev. Lett.*, 106:132503, Mar 2011.

[25] J. Randrup, P. Möller, and A. J. Sierk. Fission-fragment mass distributions from strongly damped shape evolution. *Phys. Rev. C*, 84:034613, Sep 2011.

[26] J. Randrup and P. Möller. Energy dependence of fission-fragment mass distributions from strongly damped shape evolution. *Phys. Rev. C*, 88:064606, Dec 2013.

[27] P. Moller, J.R. Nix, W.D. Myers, and W.J. Swiatecki. Nuclear ground-state masses and deformations. *Atomic Data and Nuclear Data Tables*, 59(2):185 – 381, 1995.

[28] M. D. Usang, F. A. Ivanyuk, C. Ishizuka, and S. Chiba. Analysis of the total kinetic energy of fission fragments with the langevin equation. *Phys. Rev. C*, 96:064617, Dec 2017.

[29] Chikako Ishizuka, Mark D. Usang, Fedir A. Ivanyuk, Joachim A. Maruhn, Katsuhisa Nishio, and Satoshi Chiba. Four-dimensional langevin approach to low-energy nuclear fission of ^{236}**U**. *Phys. Rev. C*, 96:064616, Dec 2017.

[30] Y. Aritomo, S. Chiba, and F. Ivanyuk. Fission dynamics at low excitation energy. *Phys. Rev. C*, 90:054609, Nov 2014.

[31] P. Möller, D. G. Madland, A. J. Sierk, and A. Iwamoto. Nuclear fission modes and fragment mass asymmetries in a five-dimensional deformation space. *Nature*, 409:785 EP –, 02 2001.

[32] Arnold J. Sierk. Langevin model of low-energy fission. *Phys. Rev. C*, 96:034603, Sep 2017.

[33] Erich Runge and E. K. U. Gross. Density-functional theory for time-dependent systems. *Phys. Rev. Lett.*, 52:997–1000, Mar 1984.

[34] Cédric Simenel. Nuclear quantum many-body dynamics. *The European Physical Journal A*, 48(11):152, Nov 2012.

[35] Takashi Nakatsukasa, Kenichi Matsuyanagi, Masayuki Matsuo, and Kazuhiro Yabana. Time-dependent density-functional description of nuclear dynamics. *Rev. Mod. Phys.*, 88:045004, Nov 2016.

[36] J. W. Negele, S. E. Koonin, P. Möller, J. R. Nix, and A. J. Sierk. Dynamics of induced fission. *Phys. Rev. C*, 17:1098–1115, Mar 1978.

[37] Ka-Hae Kim, Takaharu Otsuka, and Paul Bonche. Three-dimensional tdhf calculations for reactions of unstable nuclei. *Journal of Physics G: Nuclear and Particle Physics*, 23(10):1267, 1997.

[38] J.A. Maruhn, P.-G. Reinhard, P.D. Stevenson, and A.S. Umar. The tdhf code sky3d. *Computer Physics Communications*, 185(7):2195 – 2216, 2014.

[39] C. Simenel and A. S. Umar. Formation and dynamics of fission fragments. *Phys. Rev. C*, 89:031601, Mar 2014.

[40] Guillaume Scamps, Cédric Simenel, and Denis Lacroix. Superfluid dynamics of ^{258}Fm fission. *Phys. Rev. C*, 92:011602, Jul 2015.

[41] Yusuke Tanimura, Denis Lacroix, and Guillaume Scamps. Collective aspects deduced from time-dependent microscopic mean-field with pairing: Application to the fission process. *Phys. Rev. C*, 92:034601, Sep 2015.

[42] Philip Goddard, Paul Stevenson, and Arnau Rios. Fission dynamics within time-dependent hartree-fock: Deformation-induced fission. *Phys. Rev. C*, 92:054610, Nov 2015.

[43] Philip Goddard, Paul Stevenson, and Arnau Rios. Fission dynamics within time-dependent hartree-fock. ii. boost-induced fission. *Phys. Rev. C*, 93:014620, Jan 2016.

[44] Guillaume Scamps, Denis Lacroix, G. F. Bertsch, and Kouhei Washiyama. Pairing dynamics in particle transport. *Phys. Rev. C*, 85:034328, Mar 2012.

[45] Aurel Bulgac, Piotr Magierski, Kenneth J. Roche, and Ionel Stetcu. Induced fission of ^{240}Pu within a real-time microscopic framework. *Phys. Rev. Lett.*, 116:122504, Mar 2016.

[46] P. Hohenberg and W. Kohn. Inhomogeneous electron gas. *Phys. Rev.*, 136:B864–B871, Nov 1964.

[47] W. Kohn and L. J. Sham. Self-consistent equations including exchange and correlation effects. *Phys. Rev.*, 140:A1133–A1138, Nov 1965.

[48] L. N. Oliveira, E. K. U. Gross, and W. Kohn. Density-functional theory for superconductors. *Phys. Rev. Lett.*, 60:2430–2433, Jun 1988.

[49] Aurel Bulgac and Yongle Yu. Renormalization of the hartree-fock-bogoliubov equations in the case of a zero range pairing interaction. *Phys. Rev. Lett.*, 88:042504, Jan 2002.

[50] Yongle Yu and Aurel Bulgac. Energy density functional approach to superfluid nuclei. *Phys. Rev. Lett.*, 90:222501, Jun 2003.

[51] Aurel Bulgac and Michael McNeil Forbes. Unitary fermi supersolid: The larkin-ovchinnikov phase. *Phys. Rev. Lett.*, 101:215301, Nov 2008.

[52] Aurel Bulgac and Sukjin Yoon. Large amplitude dynamics of the pairing correlations in a unitary fermi gas. *Phys. Rev. Lett.*, 102:085302, Feb 2009.

[53] Aurel Bulgac, Yuan-Lung Luo, Piotr Magierski, Kenneth J. Roche, and Yongle Yu. Real-time dynamics of quantized vortices in a unitary fermi superfluid. *Science*, 332(6035):1288–1291, 2011.

[54] Aurel Bulgac, Yuan-Lung Luo, and Kenneth J. Roche. Quantum shock waves and domain walls in the real-time dynamics of a superfluid unitary fermi gas. *Phys. Rev. Lett.*, 108:150401, Apr 2012.

[55] I. Stetcu, A. Bulgac, P. Magierski, and K. J. Roche. Isovector giant dipole resonance from the 3d time-dependent density functional theory for superfluid nuclei. *Phys. Rev. C*, 84:051309, Nov 2011.

[56] Aurel Bulgac, Michael McNeil Forbes, Michelle M. Kelley, Kenneth J. Roche, and Gabriel Wlazłowski. Quantized superfluid vortex rings in the unitary fermi gas. *Phys. Rev. Lett.*, 112:025301, Jan 2014.

[57] Gabriel Wlazłowski, Aurel Bulgac, Michael McNeil Forbes, and Kenneth J. Roche. Life cycle of superfluid vortices and quantum turbulence in the unitary fermi gas. *Phys. Rev. A*, 91:031602, Mar 2015.

[58] Piotr Magierski, Kazuyuki Sekizawa, and Gabriel Wlazłowski. Novel Role of Superfluidity in Low-Energy Nuclear Reactions. *Phys. Rev. Lett.*, 119(4):042501, 2017.

[59] Gabriel Wlazłowski, Kazuyuki Sekizawa, Piotr Magierski, Aurel Bulgac, and Michael McNeil Forbes. Vortex pinning and dynamics in the neutron star crust. *Phys. Rev. Lett.*, 117:232701, Nov 2016.

[60] Gabriel Wlazłowski, Kazuyuki Sekizawa, Maciej Marchwiany, and Piotr Magierski. Suppressed solitonic cascade in spin-imbalanced superfluid fermi gas. *Phys. Rev. Lett.*, 120:253002, Jun 2018.

[61] The Message Passing Interface. *https://computing.llnl.gov/tutorials/mpi/*.

[62] Homepage of Nvidia CUDA. *http://www.nvidia.com/object/cuda_home_new.html*.

[63] The top 500 supercomputers.

[64] The titan supercomputer.

[65] The piz-daint supercomputer.

[66] The summit supercomputer.

[67] R.M. Dreizler and E.K.U. Gross. *Density Functional Theory: An Approach to the Quantum Many-Body Problem*. Springer Berlin Heidelberg, 2012.

[68] M Brack, C Guet, and H.-B Håkansson. Selfconsistent semiclassical description of average nuclear properties—a link between microscopic and macroscopic models. *Physics Reports*, 123(5):275 – 364, 1985.

[69] M. Brack and R.K. Bhaduri. *Semiclassical Physics*. Frontiers in physics. Addison-Wesley, Advanced Book Program, 1997.

[70] P. Ring and P. Schuck. *The Nuclear Many-Body Problem*. Springer, Berlin, 2004.

[71] P. J. Borycki, J. Dobaczewski, W. Nazarewicz, and M. V. Stoitsov. Pairing renormalization and regularization within the local density approximation. *Phys. Rev. C*, 73:044319, Apr 2006.

[72] J. Dobaczewski, W. Nazarewicz, and M.V. Stoitsov. Nuclear ground-state properties from mean-field calculations. *Eur. Phys. J. A*, 15(1):21–26, 2002.

[73] G. F. Bertsch, C. A. Bertulani, W. Nazarewicz, N. Schunck, and M. V. Stoitsov. Odd-even mass differences from self-consistent mean field theory. *Phys. Rev. C*, 79:034306, Mar 2009.

[74] M. Dutra, O. Lourenço, J. S. Sá Martins, A. Delfino, J. R. Stone, and P. D. Stevenson. Skyrme interaction and nuclear matter constraints. *Phys. Rev. C*, 85:035201, Mar 2012.

[75] M. Bender, P.-H. Heenen, and P. Bonche. Microscopic study of ^{240}Pu: Mean field and beyond. 70(5):054304, 2004.

[76] Michael Bender, Paul-Henri Heenen, and Paul-Gerhard Reinhard. Self-consistent mean-field models for nuclear structure. *Rev. Mod. Phys.*, 75:121–180, Jan 2003.

[77] Yvan Castin. Simple theoretical tools for low dimension bose gases. *arXiv:cond-mat/0407118*, 2004.

[78] W. Zwerger. *The BCS-BEC Crossover and the Unitary Fermi Gas*. Lecture Notes in Physics. Springer Berlin Heidelberg, 2011.

[79] I. Stetcu, C. A. Bertulani, A. Bulgac, P. Magierski, and K. J. Roche. Relativistic Coulomb Excitation within the Time Dependent Superfluid Local Density Approximation. *Phys. Rev. Lett.*, 114:012701, Jan 2015.

[80] Aurel Bulgac, Michael McNeil Forbes, Shi Jin, Rodrigo Navarro Perez, and Nicolas Schunck. Minimal nuclear energy density functional. *Phys. Rev. C*, 97:044313, Apr 2018.

[81] G. Audi, M. Wang, A.H. Wapstra, F.G. Kondev, M. MacCormick, X. Xu, and B. Pfeiffer. The ame2012 atomic mass evaluation. *Chinese Physics C*, 36(12):1287, 2012.

[82] M. Wang, G. Audi, A.H. Wapstra, F.G. Kondev, M. MacCormick, X. Xu, and B. Pfeiffer. The AME2012 atomic mass evaluation. 36(12):1603, 2012.

[83] G. Wlazłowski, J. W. Holt, S. Moroz, A. Bulgac, and K. J. Roche. Auxiliary-field quantum monte carlo simulations of neutron matter in chiral effective field theory. *Phys. Rev. Lett.*, 113:182503, Oct 2014.

[84] E. Chabanat, P. Bonche, P. Haensel, J. Meyer, and R. Schaeffer. A skyrme parametrization from subnuclear to neutron star densities part ii. nuclei far from stabilities. *Nuclear Physics A*, 635(1):231 – 256, 1998.

[85] S. A. Fayans. Towards a universal nuclear density functional. *Journal of Experimental and Theoretical Physics Letters*, 68(3):169–174, Aug 1998.

[86] K. Bennaceur and J. Dobaczewski. Coordinate-space solution of the Skyrme–Hartree–Fock–Bogolyubov equations within spherical symmetry. The program HFBRAD (v1.00). 168(2):96 – 122, 2005.

[87] I. Angeli and K.P. Marinova. Table of experimental nuclear ground state charge radii: An update. 99(1):69 – 95, 2013.

[88] R. O. Jones and O. Gunnarsson. The density functional formalism, its applications and prospects. 61:689–746, July 1989.

[89] Andrew E. DePristo and Joel D. Kress. Kinetic-energy functionals via padé approximations. 35:438–441, January 1987.

[90] C. F. v. Weizsäcker. Zur theorie der kernmassen. 96:431–458, 1935.

[91] R. Navarro Perez, N. Schunck, R.-D. Lasseri, C. Zhang, and J. Sarich. Axially deformed solution of the skyrme–hartree–fock–bogolyubov equations using the transformed harmonic oscillator basis (iii) hfbtho (v3.00): A new version of the program. *Computer Physics Communications*, 220:363 – 375, 2017.

[92] M.V. Stoitsov, N. Schunck, M. Kortelainen, N. Michel, H. Nam, E. Olsen, J. Sarich, and S. Wild. Axially deformed solution of the skyrme-hartree–fock–bogoliubov equations using the transformed harmonic oscillator basis (ii) hfbtho v2.00d: A new version of the program. *Computer Physics Communications*, 184(6):1592 – 1604, 2013.

[93] M.V. Stoitsov, J. Dobaczewski, W. Nazarewicz, and P. Ring. Axially deformed solution of the skyrme–hartree–fock–bogolyubov equations using the transformed harmonic oscillator basis. the program hfbtho (v1.66p). *Computer Physics Communications*, 167(1):43 – 63, 2005.

[94] M. Kortelainen, T. Lesinski, J. Moré, W. Nazarewicz, J. Sarich, N. Schunck, M. V. Stoitsov, and S. Wild. Nuclear energy density optimization. *Phys. Rev. C*, 82:024313, Aug 2010.

[95] M. Kortelainen, J. McDonnell, W. Nazarewicz, P.-G. Reinhard, J. Sarich, N. Schunck, M. V. Stoitsov, and S. M. Wild. Nuclear energy density optimization: Large deformations. *Phys. Rev. C*, 85:024304, Feb 2012.

[96] M. Kortelainen, J. McDonnell, W. Nazarewicz, E. Olsen, P.-G. Reinhard, J. Sarich, N. Schunck, S. M. Wild, D. Davesne, J. Erler, and A. Pastore. Nuclear energy density optimization: Shell structure. *Phys. Rev. C*, 89:054314, May 2014.

[97] H. De Vries, C. W. De Jager, and C. De Vries. Nuclear charge-density-distribution parameters from elastic electron scattering. 36:495 – 536, 1987.

[98] C.J. Horowitz, K.S. Kumar, and R. Michaels. Electroweak measurements of neutron densities in CREX and PREX at JLab, USA. 50(2), 2014.

[99] A. Tamii, I. Poltoratska, P. von Neumann-Cosel, Y. Fujita, T. Adachi, C. A. Bertulani, J. Carter, M. Dozono, H. Fujita, K. Fujita, K. Hatanaka, D. Ishikawa, M. Itoh, T. Kawabata, Y. Kalmykov, A. M. Krumbholz, E. Litvinova, H. Matsubara, K. Nakanishi, R. Neveling, H. Okamura, H. J. Ong, B. Özel-Tashenov, V. Yu. Ponomarev, A. Richter, B. Rubio, H. Sakaguchi, Y. Sakemi, Y. Sasamoto, Y. Shimbara, Y. Shimizu, F. D. Smit, T. Suzuki, Y. Tameshige, J. Wambach, R. Yamada, M. Yosoi, and J. Zenihiro. Complete electric dipole response and the neutron skin in ^{208}Pb. 107(6):062502, August 2011.

[100] C. M. Tarbert, D. P. Watts, D. I. Glazier, P. Aguar, J. Ahrens, J. R. M. Annand, H. J. Arends, R. Beck, V. Bekrenev, B. Boillat, A. Braghieri, D. Branford, W. J. Briscoe, J. Brudvik, S. Cherepnya, R. Codling, E. J. Downie, K. Foehl, P. Grabmayr, R. Gregor, E. Heid, D. Hornidge, O. Jahn, V. L. Kashevarov, A. Knezevic, R. Kondratiev, M. Korolija, M. Kotulla, D. Krambrich, B. Krusche, M. Lang, V. Lisin, K. Livingston, S. Lugert, I. J. D. MacGregor, D. M. Manley, M. Martinez, J. C. McGeorge, D. Mekterovic, V. Metag, B. M. K. Nefkens, A. Nikolaev, R. Novotny, R. O. Owens, P. Pedroni, A. Polonski, S. N. Prakhov, J. W. Price, G. Rosner, M. Rost, T. Rostomyan, S. Schadmand, S. Schumann, D. Sober, A. Starostin, I. Supek, A. Thomas, M. Unverzagt, Th. Walcher, L. Zana, and F. Zehr. Neutron Skin of 208Pb from Coherent Pion Photoproduction. 112:242502, 2014.

[101] M. Baldo, C. Maieron, P. Schuck, and X. Viñas. Low densities in nuclear and neutron matters and in the nuclear surface. 736(3):241 – 254, 2004.

[102] M. Baldo, P. Schuck, and X. Viñas. Kohn–Sham density functional inspired approach to nuclear binding. 663(5):390–394, 6 2008.

[103] M. Baldo, L. M. Robledo, P. Schuck, and X. Viñas. New Kohn-Sham density functional based on microscopic nuclear and neutron matter equations of state. 87:064305, June 2013.

[104] N. Schwierz, I. Wiedenhover, and A. Volya. Parameterization of the Woods-Saxon Potential for Shell-Model Calculations. September 2007.

[105] J. Dobaczewski and P. Olbratowski. Solution of the Skyrme–Hartree–Fock–Bogolyubov equations in the Cartesian deformed harmonic-oscillator basis. (IV) HFODD (v2.08i): a new version of the program. 158(3):158 – 191, 2004.

[106] N. Schunck, D. Duke, H. Carr, and A. Knoll. Description of induced nuclear fission with Skyrme energy functionals: Static potential energy surfaces and fission fragment properties. 90:054305, Nov 2014.

[107] J. Bartel, P. Quentin, M. Brack, C. Guet, and H.-B. Håkansson. Towards a better parametrisation of Skyrme-like effective forces: A critical study of the SkM force. 386(1):79 – 100, 1982.

[108] Nicolas Schunck, Jordan D McDonnell, Jason Sarich, Stefan M Wild, and Dave Higdon. Error analysis in nuclear density functional theory. *Journal of Physics G: Nuclear and Particle Physics*, 42(3):034024, 2015.

[109] J.F. Berger, M. Girod, and D. Gogny. Constrained Hartree-Fock and beyond. 502(Supplement C):85 – 104, 1989.

[110] Peter Möller, Arnold J. Sierk, Takatoshi Ichikawa, Akira Iwamoto, Ragnar Bengtsson, Henrik Uhrenholt, and Sven Åberg. Heavy-element fission barriers. 79:064304, June 2009.

[111] R. Jodon, M. Bender, K. Bennaceur, and J. Meyer. Constraining the surface properties of effective Skyrme interactions. 94:024335, Aug 2016.

[112] A Bulgac, S. Jin, K J Roche, N. Schunck, and I. Stetcu. Fission dynamics. *arXiv: 1806.00694*, 2018.

[113] D. Vautherin. Hartree-Fock Calculations with Skyrme's Interaction. II. Axially Deformed Nuclei. *Phys. Rev. C*, 7(1):296, 1973.

[114] Aurel Bulgac and Shi Jin. Dynamics of fragmented condensates and macroscopic entanglement. *Phys. Rev. Lett.*, 119:052501, Jul 2017.

[115] C. Simenel and G. Scamps. Impact of pear-shaped fission fragments on mass-asymmetric fission in actinides. *Nature*, 564:382, 2018.

[116] C. Wagemans, E. Allaert, A. Deruytter, R. Barthélémy, and P. Schillebeeckx. Comparison of the energy and mass characteristics of the Pu239(nth,f) and the Pu240(sf) fragments. *Phys. Rev. C*, 30(1):218, 1984.

[117] P. Schillebeeckx, C. Wagemans, A.J. Deruytter, and R. Barthélémy. Comparative study of the fragments' mass and energy characteristics in the spontaneous fussion of ^{238}Pu, ^{240}Pu and ^{242}Pu and in the thermal-neutron-induced fission of ^{239}Pu. *Nucl. Phys. A*, 545(3):623, 1992.

[118] A. C. Wahl. Technical Report LA-13928, Los Alamos, 2002.

[119] R. Vogt, J. Randrup, J. Pruet, and W. Younes. Event-by-event study of prompt neutrons from ^{239}Pu(n, f). *Phys. Rev. C*, 80:044611, Oct 2009.

[120] D.G. Madland. Total prompt energy release in the neutron-induced fission of 235U, 238U, and 239Pu. *Nucl. Phys. A*, 772:113, 2006.

[121] P. Talou, B. Becker, T. Kawano, M. B. Chadwick, and Y. Danon. Advanced Monte Carlo modeling of prompt fission neutrons for thermal and fast neutron-induced fission reactions on Pu239. *Phys. Rev. C*, 83(6):064612, 2011.

[122] B. Becker, P. Talou, T. Kawano, Y. Danon, and I. Stetcu. Monte Carlo Hauser-Feshbach predictions of prompt fission γ rays: Application to n_{th}+^{235}U, n_{th}+^{239}Pu, and ^{252}Cf (sf). *Phys. Rev. C*, 87(1):014617, 2013.

[123] J.M. Verbeke, J. Randrup, and R. Vogt. Fission Reaction Event Yield Algorithm, FREYA — For event-by-event simulation of fission. *Comput. Phys. Commun.*, 191:178, 2015.

[124] J. M. Verbeke, J. Randrup, and R. Vogt. Fission Reaction Event Yield Algorithm FREYA 2.0.2. *Comput. Phys. Commun.*, 222:263, 2018.

[125] N. Schunck, D. Duke, and H. Carr. Description of induced nuclear fission with Skyrme energy functionals. II. Finite temperature effects. *Phys. Rev. C*, 91(3):034327, 2015.

[126] H. Goutte, J. F. Berger, P. Casoli, and D. Gogny. Microscopic approach of fission dynamics applied to fragment kinetic energy and mass distributions in ^{238}U. *Phys. Rev. C*, 71:024316, Feb 2005.

[127] D. Regnier, N. Dubray, N. Schunck, and M. Verrière. Fission fragment charge and mass distributions in ^{239}Pu(n, f) in the adiabatic nuclear energy density functional theory. *Phys. Rev. C*, 93:054611, May 2016.

[128] C. Ishizuka, M. D. Usang, F. A. Ivanyuk, J. A. Maruhn, K. Nishio, and S. Chiba. Four-dimensional Langevin approach to low-energy nuclear fission of ^{236}**U**. *Phys. Rev. C*, 96:064616, Dec 2017.

[129] Jhilam Sadhukhan, Witold Nazarewicz, and Nicolas Schunck. Microscopic modeling of mass and charge distributions in the spontaneous fission of ^{240}Pu. *Phys. Rev. C*, 93:011304, Jan 2016.

[130] J. Sadhukhan, C. Zhang, W. Nazarewicz, and N. Schunck. Formation and distribution of fragments in the spontaneous fission of $^{\mathbf{240}}$**Pu**. *Phys. Rev. C*, 96:061301, Dec 2017.

[131] Y.M. Engel, D.M. Brink, K. Goeke, S.J. Krieger, and D. Vautherin. Time-dependent Hartree-Fock theory with Skyrme's interaction. *Nuclear Physics A*, 249(2):215 – 238, 1975.

[132] Aurel Bulgac and Michael McNeil Forbes. Use of the discrete variable representation basis in nuclear physics. *Phys. Rev. C*, 87:051301, May 2013.

[133] J. K. Krappe and K. Pomorski. *Theory of Nuclear Fission*. Springer Heidelberg, 2012.

[134] A. Bulgac, M. M. Forbes, and P. Magierski. *The Unitary Fermi Gas: From Monte Carlo to Density Functionals*, chapter 9, pages 127 – 191. In *Lecture Notes in Physics* [78], 2011.

[135] G. F. Bertsch, W. Younes, and L. M. Robledo. Scission dynamics with k partitions. *Phys. Rev. C*, 97:064619, Jun 2018.

[136] B. D. Wilkins, E. P. Steinberg, and R. R. Chasman. Scission-point model of nuclear fission based on deformed-shell effects. *Phys. Rev. C*, 14:1832–1863, Nov 1976.

[137] Jean-Fran çois Lemaître, Stefano Panebianco, Jean-Luc Sida, Stéphane Hilaire, and Sophie Heinrich. New statistical scission-point model to predict fission fragment observables. *Phys. Rev. C*, 92:034617, Sep 2015.

[138] P. Fröbrich and I.I. Gontchar. Langevin description of fusion, deep-inelastic collisions and heavy-ion-induced fission. *Physics Reports*, 292(3):131 – 237, 1998.

[139] D. E. Ward, B. G. Carlsson, T. Døssing, P. Möller, J. Randrup, and S. Åberg. Nuclear shape evolution based on microscopic level densities. *Phys. Rev. C*, 95:024618, Feb 2017.

[140] M. Albertsson, B.G. Carlsson, T. Døssing, P. Møller, J. Randrup, and S. Åberg. Microscopic treatment of energy partition in fission.

[141] R. Capote, N. Carjan, and S. Chiba. Scission neutrons for U, Pu, Cm, and Cf isotopes: Relative multiplicities calculated in the sudden limit. *Phys. Rev. C*, 93:024609, Feb 2016.

[142] Vorobyev, A.S., Shcherbakov, O.A., Gagarski, A.M., Val´ski, G.V., and Petrov, G.A. Investigation of the prompt neutron emission mechanism in low energy fission of 235,233U(n_{th} f) and 252Cf(sf). *EPJ Web of Conferences*, 8:03004, 2010.

[143] N.V Kornilov, A.B Kagalenko, S.V Poupko, P.A Androsenko, and F.-J Hambsch. New evidence of an intense scission neutron source in the 252Cf spontaneous fission. *Nuclear Physics A*, 686(1):187 – 203, 2001.

[144] N. V. Kornilov, A. B. Kagalenko, and F.-J. Hambsch. Prescission neutrons in the fission of 235U and 252Cf nuclei. *Physics of Atomic Nuclei*, 64(8):1373–1385, Aug 2001.

[145] G. A. Petrov. Current status of the search for scission neutrons in fission and estimation of their main characteristics. *AIP Conference Proceedings*, 798(1):205–212, 2005.

[146] P. A. Anderson. *Basic Notions of Condensed Matter Physics*. Benjamin/Cummins Publishing Company Inc. London, 1984.

[147] J. Dechargé and D. Gogny. Hartree-fock-bogolyubov calculations with the $d1$ effective interaction on spherical nuclei. *Phys. Rev. C*, 21:1568–1593, Apr 1980.

[148] M. Baranger. Microscopic view of nuclear collective properties. *J. Phys.*, 33:C5–61, 1972.

[149] M. Baranger and M. Veneroni. An adiabatic time-dependent Hartree-Fock theory of collective motion in finite systems. *Ann. Phys.*, 114(1):123, 1978.

[150] F. Villars. Adiabatic time-dependent Hartree-Fock theory in nuclear physics. *Nucl. Phys. A*, 285:269–296, 1978.

[151] T. Ledergerbert, Z. Paltiel, Z. Fraenkel, and H.C. Pauli. Dynamic excitation in fission. *Nuclear Physics A*, 275:280, 1977.

[152] J. Blocki, Y. Boneh, J. R. Nix, J. Randrup, M. Robel, A. J. Sierk, and W. J. Swiatecki. One-body dissipation and the super-viscidity of nuclei. 113(2):330 – 386, 1978.

[153] D. Regnier, N. Dubray, and N. Schunck. From asymmetric to symmetric fission in the fermium isotopes within the time-dependent generator-coordinate-method formalism. *Phys. Rev. C*, 99:024611, 2019.

[154] R. Balian and M. Véneroni. Fluctuations in a time-dependent mean-field approach. 136(5-6):301 – 306, 1984.

[155] J. W. Negele and H. Orland. *Quantum Many-Particle Systems*. Westview Press, Reading, MA, November 1998.

[156] A. Bulgac. The Long Journey from Ab Initio Calculations to Density Functional Theory for Nuclear Large Amplitude Collective Motion. *J. Phys. G: Nucl. Part. Phys.*, 37(6):064006, 2010.

[157] J. J. Griffin and J. A. Wheeler. Collective Motions in Nuclei by the Method of Generator Coordinates. *Phys. Rev.*, 108:311–327, Oct 1957.

[158] N. G. Van Kampen. *Stochastic Processes in Physics and Chemistry*. Elsevier, 3rd edition, 2007.

[159] Y. Abe, S. Ayik, P.-G. Reinhard, and E. Suraud. On stochastic approaches of nuclear dynamics. *Physics Reports*, 275(2):49 – 196, 1996.

[160] A. Bulgac, S. Jin, and I. Stetcu. Unitary Evolution with Dissipation and Fluctuations. *arXiv:1805.08908*, 2018.

[161] Denis Lacroix and Sakir Ayik. Stochastic quantum dynamics beyond mean field. *Eur. Phys. J. A*, 50(6):95, 2014.

[162] Sakir Ayik. A stochastic mean-field approach for nuclear dynamics. *Phys. Lett. B*, 658(4):174, 2008.

[163] Yusuke Tanimura, Denis Lacroix, and Sakir Ayik. Microscopic Phase-Space Exploration Modeling of Fm 258 Spontaneous Fission. *Phys. Rev. Lett.*, 118(15):152501, 2017.

[164] N. G. van Kampen. Itô versus Stratonovich. *Journal of Statistical Physics*, 24:175, 1981.

[165] A. Bulgac, M. M. Forbes, K. J. Roche, and G. Wlazłowski. Quantum Friction: Cooling Quantum Systems with Unitary Time Evolution, 2013.

[166] E. K. Hulet, J. F. Wild, R. J. Dougan, R. W. Lougheed, J. H. Landrum, A. D. Dougan, P. A. Baisden, C. M. Henderson, R. J. Dupzyk, R. L. Hahn, M. Schädel, K. Sümmerer, and G. R. Bethune. Spontaneous fission properties of ^{258}Fm, ^{259}Md, ^{260}Md, ^{258}No, and ^{260}[104]: Bimodal fission. *Phys. Rev. C*, 40:770–784, Aug 1989.

[167] A. Bulgac, M. M. Forbes, and W. Wlazłowski. Towards quantum turbulence in cold atomic fermionic superfluids. *J. Phys. B: At. Mol. Opt. Phys.*, 50:014001, 2016.

[168] G F Bertsch, W Loveland, W Nazarewicz, and P Talou. Benchmarking nuclear fission theory. *Journal of Physics G: Nuclear and Particle Physics*, 42(7):077001, 2015.

[169] Daniel Baye. The lagrange-mesh method. *Physics Reports*, 565:1 – 107, 2015.

[170] L.N. Trefethen. *Spectral Methods in MATLAB*. Software, Environments, and Tools. Society for Industrial and Applied Mathematics, 2000.

[171] Shi Jin, Aurel Bulgac, Kenneth Roche, and Gabriel Wlazłowski. Coordinate-space solver for superfluid many-fermion systems with the shifted conjugate-orthogonal conjugate-gradient method. *Phys. Rev. C*, 95(4):044302, 2017.

[172] A Castro, A Rubio, and M J Stott. Solution of poisson's equation for finite systems using plane-wave methods. *Canadian Journal of Physics*, 81(10):1151–1164, 2003.

[173] Andrzej Baran, Aurel Bulgac, Michael McNeil Forbes, Gaute Hagen, Witold Nazarewicz, Nicolas Schunck, and Mario V. Stoitsov. Broyden's method in nuclear structure calculations. *Phys. Rev. C*, 78:014318, Jul 2008.

[174] A. Staszczak, M. Stoitsov, A. Baran, and W. Nazarewicz. Augmented lagrangian method for constrained nuclear density functional theory. *Eur. Phys. J. A*, 46(1):85–90, 2010.

[175] R.W. Hamming. *Numerical Methods for Scientists and Engineers*. Dover books on engineering. Dover, 1986.

[176] The two-dimensional block-cyclic distribution.

[177] Scalapack – scalable linear algebra package.

[178] S. A. Umar and C. Simenel. TDHF investigations of the U+U quasifission process .